THE HIGH FREQUENCY SURFACE WAVE RADAR CROSS SECTION FOR OCEAN SWELL: DERIVATION AND INVERSION

CHENGXI SHEN

The High Frequency Surface Wave Radar Cross Section for Ocean Swell: Derivation and Inversion

by

©Chengxi Shen, B. Sc.

A thesis submitted to the School of Graduate Studies in partial fulfillment of the requirements for the degree of

Master of Engineering

Faculty of Engineering and Applied Science

Memorial University of Newfoundland

March, 2013

St. John's Newfoundland

Abstract

Over the last four decades, the application of high frequency (HF) radars to the monitoring of ocean surface has emerged as a vibrant field of study in the remote sensing and oceanographic communities. These HF radars, operating in the surface wave mode, can provide accurate and real-time information regarding surface currents and waves, which greatly aids in the planning and execution of oceanographic projects, search and rescue events, and commercial fisheries. However, most present HF radar techniques are restricted to the measurement of sea state parameters associated with wind waves only, while the underlying swell component, which may severely distort the inversion results and pose certain hazards on offshore activities, is usually neglected.

In this thesis, the first- and second-order HF radar cross sections are derived for the random, time-varying, swell-contaminated seas. The analysis originates from the electric field equations for the scattering of HF radiation from the ocean surface, with the source being a vertical dipole with a pulsed sinusoidal excitation. The various field components are then autocorrelated and Fourier transformed to give the power spectral density. Finally, the expressions of the cross sections can be obtained using the radar range equation. By introducing appropriate directional wave spectra to specify the ocean surface as a mixture of wind waves and swell, the derived cross section models are calculated and depicted. Essential characteristics and major differences from conventional cross sections for purely wind-driven seas are discussed.

Next, the study is extended to include the consideration of a frequency modulated continuous wave source (FMCW), because such a waveform is often employed in practical HF radar systems. The mathematical expressions for the FMCW cross sections of swell-contaminated seas are first presented, and their properties are then addressed. Only trivial differences can be observed when comparing the cross section model for the pulsed and FMCW wave forms, which indicates that an inversion routine may be developed and applied simultaneously for both cases.

Finally, an inversion algorithm is proposed for the extraction of swell parameters from HF radar Doppler spectra. These include the swell dominant period, propagating direction, frequency spreading, and significant wave height. The method involves the identification of swell peaks, the processing of swell peak positions, the measurement of swell peak half-power widths, and a maximum likelihood calculation. The procedure is then tested against simulated data, and promising inversion results are obtained. It is concluded that fine Doppler resolution is required to ensure the retrieval accuracy, and dual-radar systems are highly recommended to eliminate the directional ambiguity in swell direction.

Overall, the analysis presented here may provide a solid foundation for future research on other types of ocean surfaces. Additionally, the properties of the scattering as manifested in this thesis should be relevant to the understanding of the complicated hydrodynamic interaction between swell and wind waves.

Acknowledgements

I would like to thank my supervisors, Dr. Weimin Huang and Dr. Eric Gill, for their exceptional guidance and enthusiastic support throughout the research period, both academically and financially. You granted me the chance to pursue my years-long dream of studying abroad, you led me into this fantastic world of ocean remote sensing, and you provided critical comments and constructive suggestions when I was lost. I am indebted to you, always.

I would also like to express my sincere respect to Dr. John Walsh, whom I do not have the fortune to meet in person. Your brilliance has always amazed and inspired me whenever I read your work regarding this topic. I hope that one day I can grow into a great scholar just like you, independent and passionate. Rest in peace.

I am also grateful to all my friends and colleagues in St.John's. Forgive me that I cannot fit all your names into this short acknowledgment. St.John's is no paradise, especially when talking about its harsh weather and lack of entertainment. It's you that make this place much warmer, much brighter, and more like home. Be well.

Finally, this work could not have been completed without the patience and encouragement from my wonderful family - my parents, Hande Shen and Xianfang Zhang, and my lovely wife, Wenli Hu. In particular, dear Wenli has always been tolerant and supportive. Thanks for your unyielding devotion and faith in me. Thank you.

Table of Contents

List of Tables

List of Figures

Table of Symbols

The page numbers here indicate the place of first significant reference. Although not all symbols are explicitly referenced below, their definitions are obvious from the context.

f_B, ω_B : Bragg frequency in Hz and radians (p.6).

λ_0 : Incident wavelength of the radar signals (p.6).

g : Gravitational acceleration (p.6).

Δf : Doppler frequency shift induced by surface currents (p.7).

f_0 : Radar frequency (p.7).

c : Light speed (p.7).

$\vec{K}_B$: Bragg wave vector (p.8).

E_n : The scattered electric field normal to the surface and in the limit as the surface is approached from above (p.19).

ξ : Elevation profile of the ocean surface (p.19).

ρ : Distance of a general point (x, y) on the surface (p.19).

k_0 : Wavenumber of the transmitted radar signal (p.19).

η_0 : Intrinsic impedance of free space (p.20).

$\Delta\rho$: Scattering patch width (p.20).

$_E\Gamma_p$: Electromagnetic coupling coefficient for patch scatters in a symmetric form (p.20).

$P_{\vec{K},\omega}$: Fourier coefficient of the ocean surface (p.20).

$_H\Gamma_p$: Hydrodynamic coupling coefficient (p.21).

Δ : Normalized surface impedance (p.25).

$\mathcal{R}(\tau)$: Autocorrelation of the electric fields (p.28).

A_r : Effective aperture of the receiving antenna (p.28).

$S_1(\vec{K})$: First-order directional ocean wave spectrum (p.30).

f_d, ω_d : Doppler frequency in Hz and radians (p.31).

$\mathcal{P}(\omega_d)$: Doppler power spectral density (p.31).

Γ_p : Combined coupling coefficient (p.32).

$\sigma(\omega_d)$: Radar cross sections (p.36).

$_C\Gamma_p$: Coupling coefficient between swell and wind waves (p.38).

$D(\theta_{\vec{K}})$: Normalized directional distribution function (p.42).

θ_N : Radar look direction (p.42).

s : Directional spreading factor for a typical cardioid model (p.42).

U : Local wind speed (p.44).

$_SH_s$: Significant wave height of the swell component (p.52).

θ_s : Propagation direction of the swell component (p.53).

ϕ_i : Intersection angle between the radar look direction and the swell direction (p.53).

T_s : Dominant period of the swell component (p.54).

θ_w : Local wind direction (p.56).

ω_r : Frequency corresponding to a particular range cell (p.61).

α : Sweep rate of the FMCW signal (p.61).

B : Bandwidth of the FMCW signal (p.61).

T_r : Sweep interval of the FMCW signal (p.61).

f_s, ω_s : Peak frequency of the swell spectrum in Hz and Radians (p.68).

N : Shape factor of the swell spectrum (p.68).

ω_{sp} : Doppler frequency of the swell peaks (p.80).

K_s : Dominant wavenumber of the swell component (p.80).

ω_{hp} : Half-power width of the swell peak (p.88).

ω_{hp} : Half-power width of the swell spectrum (p.88).

ω_{Dhp} : Half-power width of the swell peak in Doppler spectra (p.88).

$N(\vec{K}, \omega)$: Random factor in surface Fourier coefficients (p.113).

$\epsilon(\vec{K})$) : Random phase variables uniformly distributed on $[0, 2\pi]$ for each $\vec{K}$ (p.115).

Chapter 1

Introduction

1.1 Research Rationale

The oceans have always been a key part in many cultures and a great influence on every individual on planet Earth. Environmentally, oceans are the sources for short-term weather activities and long-term climate change. Commercially, oceans teem with rich resources and provide indispensable routes for global shipment. In this sense, there has arisen an unprecedented demand for effective ocean observation strategies, technologies and applications, especially in those coastal-based and marine dependent countries such as the U.S., Canada and China. Thanks to the increasing understanding in hydrodynamics and ocean engineering enabled by modern technologies, oceanographers and ocean engineers are able to estimate various parameters associated with directional wave height spectra and surface currents. Undoubtedly, such information is highly valuable for search and rescue operations, ocean-related national defense, weather forecasts, the design of offshore structures, coastal fishery management and the control and tracking of surface-borne pollutants, to name just a few.

Conventionally, the measurement of the ocean surface has been achieved by a number of instruments including SLDMB (self-locating data marker buoys), Drifter Buoys, ADCP (acoustic Doppler Current Profilers), Waverider and other buoy technologies. Although these technologies are basically very mature and are widely applied, the inherent dynamic nature of the ocean and surrounding vessel traffic still render a challenging environment for these *in situ* sensors. For instance, moored and drifting buoys can be frequently caught in fishing nets or damaged by shipping and, once broken, they are usually very expensive and difficult to repair and maintain. Besides, the deployment, retrieval and data transmission in rough seas, where the information may be most critical, can be both costly and impractical [5]. Moreover, most buoys provide only limited spatial or temporal coverage that is far from satisfactory.

Against this backdrop, a variety of ocean remote sensing techniques have emerged in recent decades. Microwave radars, for example, are quite capable in providing ocean surface parameters with fine resolutions. However, the line-of-sight operation of microwave radars severely reduces the observation range compared with *in situ* devices, and the measurement is likely to be affected by the weather condition (e.g., heavy rain) so that the accuracy cannot be guaranteed at all times. More importantly, microwaves only interact with very small scale ocean waves (from several millimetres to metres in wavelength), while most of the wave energy is contained within the much longer gravity waves that have wavelengths of tens to hundreds of metres. It has proven to be a complicated and indirect process to determine the complete wave energy spectrum based solely on the measurement of short waves, and this poses limitations on the use of microwave radars in the area of ocean surface monitoring.

Another widely accepted remote sensing tool is the high frequency (HF) radar operating between 3 and 30 MHz. Unlike microwave radars, radio signals in this band, when guided by a good conducting medium like sea water, are able to travel

long distances along the earth's curvature. In other words, HF radars are not restricted to line-of-sight operations and can, with moderate transmitting power, actually see beyond the horizon. In addition, since the wavelengths associated with HF signals are of the same order as those ocean waves that carry most of the spectral energy, the transmitted signals will interact very strongly with these waves. This reduces the complexity in interpreting the backscattered signals for wave information. Finally, HF radars are rarely affected by weather, clouds or changing ocean conditions, and are capable of providing near real-time measurements with high temporal and reasonable spatial resolution.

As will be indicated in the next section, several mature algorithms already exist for the extraction of ocean wave spectra from HF return signals. However, most of these inversion routines are for wind waves generated by the local wind field, whereas in fact, the wave records often reveal additional spectral content associated with waves of longer period. These waves are commonly called swell (see Fig. 1.1). Basically, swell consists of waves that are generated by earlier storms at a distant location. After leaving the area of the active wind field, these waves propagate freely across the ocean surface, dissipating energy dissipation and spreading laterally, and result in a decrease in the wave heights. This effect is greater for the shorter period waves so that the components of swell are generally long period and narrow-band waves.

The coexistence of wind sea and swell, which may impose grave threats to sea-keeping safety, offshore structure designs, and surf forecasting [6], has been extensively reported by various researchers globally. Titov [7] presented the distribution of the frequency of wind waves and swell for the North Atlantic during winter and summer, showing that regions with heavy swell extend over open ocean as well as coastal areas. Thompson [8] analysed wave records from nine locations along United States Atlantic, Pacific, Gulf and Great Lakes coasts and observed that multi-peaked

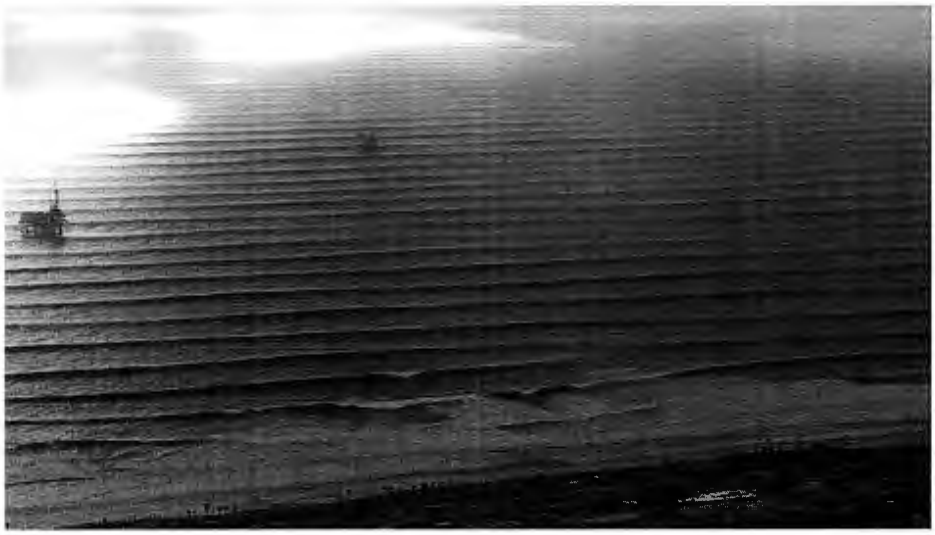

Figure 1.1: A picture of swell dominated sea [1].

spectra are common at all locations. Cummings *et al.* [9], using hindcast data from the North Atlantic, determined that 25% of the spectra were double-peaked, while Aranuvachapun [10] reported 24% from the analysis of measured data in the same area. From these results, it is clear that combined wind wave and swell systems can occur at relatively high frequency both in the open ocean and in coastal sites.

Predictably, in the context of HF radar spectra, the underlying swell component will be reflected and might, if not properly treated, result in inaccurate inversion for the local sea state. Meanwhile, since the coexistence of swell and wind waves has already been proved to be the "precursor" of some abnormal sea conditions [11], knowledge of the incoming swell may help in providing early warnings so that operators of offshore units are able to anticipate contingencies and introduce accident prevention initiatives. Thus, a new model accounting for the swell effect must be established as a complement to the present HF radar remote sensing techniques.

This thesis aims primarily at developing a general HF cross section model for swell-contaminated seas and an automated routine for swell parameter extraction. Some practical engineering applications, including the use of frequency modulated

(FM) waveforms, will be also considered here. Hopefully, the model and algorithm formulated here will provide a foundation for future investigations that focus on other wave components, and ultimately benefit the coastal-based industry at large.

1.2 Literature Review

1.2.1 Fundamental Concepts of HF Radars

An HF surface wave radar system (including antennas, transmitter, receiver, control and data processing units) is typically installed at a site very near the coast because the signal can be severely attenuated by land. Moreover, for optimal surface wave propagation, the transmitted electromagnetic (EM) signal is generally vertically polarized and narrow band. As it propagates along the electrically conductive ocean water surface, the EM wave is scattered off any object it encounters (including ocean waves), and some of the reflected energy, which contains information regarding the target, is collected by the receiving antenna. By analysing this return signal through means of Doppler spectra, a variety of parameters can be estimated.

When HF radar technology initially appeared during the second world war, it was used to detect approaching enemy aircrafts and vessels. Before long it was noticed that scattering from an unknown source often masked the targets being tracked. For a relatively long time, there was no satisfactory explanation for this contamination which was later referred to as "clutter". It was not until 1955 that Crombie [12] first suggested and confirmed the source of this clutter. Crombie correctly pointed out that the two discrete spectral peaks sitting at an equal distance above and below the radar carrier frequency in the Doppler spectrum (see Fig. 1.2) are resulted from the Bragg scattering [13] and these peaks are thus named Bragg peaks. In the case of monostatic radar configuration (co-located transmitting and receiving antennas) and

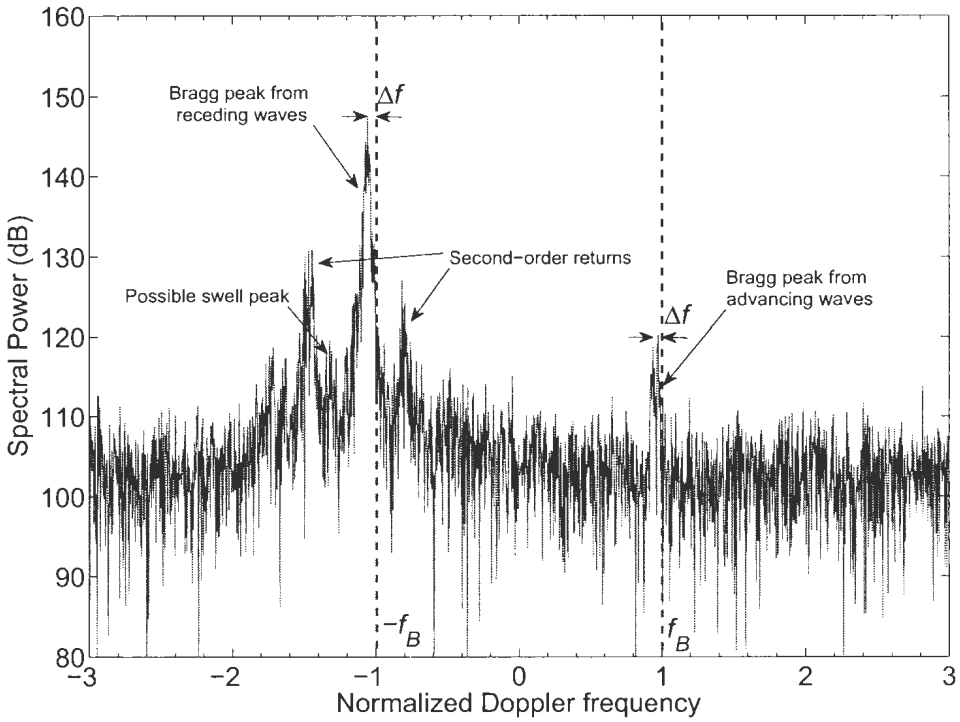

Figure 1.2: Sample backscatter Doppler spectrum from the ocean surface showing prominent Bragg peaks due to waves advancing toward and receding from the receiver. The tiny Doppler deviation from the theoretical Bragg peaks, Δf, is due to ocean surface currents. The second-order continuum is also identifiable in this example. The data was collected at Placentia Bay, NL, Canada, Jan. 2013.

grazing incidence, the Bragg waves refer to those ocean waves having wavelengths one half to those of the incident EM waves, so that phase coherent reinforcement occurs (see Fig. 1.3). From Crombie [12], the Doppler shift caused by this first-order resonant phenomenon is

$$f_B = \frac{2v}{\lambda_0} = \frac{v}{\lambda} = \sqrt{\frac{g}{2\pi\lambda}} = \sqrt{\frac{g}{\pi\lambda_0}} \tag{1.1}$$

where f_B is the theoretical Doppler shift (Hz), v is the ocean wave radial speed (m/s), λ is the ocean wave wavelength (m), λ_0 is the incident wavelength (m) and g is the

gravity acceleration. Clearly, (1.1) directly explains the two dominant peaks in the Doppler spectrum.

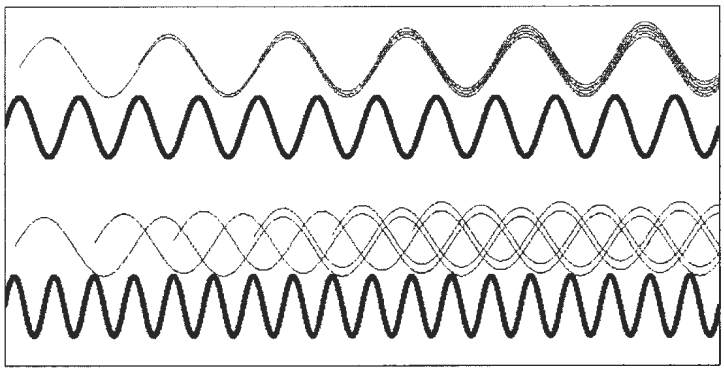

Figure 1.3: Bragg scattering of the incident EM wave (thin) by ocean waves (thick) with wavelength $\lambda_0/2$ (top), and the cancellation of EM energy for arbitrary ocean wavelengths (bottom). Figure taken from [2].

Based on these findings, Crombie [12] realized that the small differences between the expected Bragg peak positions and measured Doppler frequencies could be the consequence of surface current velocities. His conjecture has been extensively verified (see, for example, [14]). When the frequency shift due to surface currents is defined as Δf, the current velocity can be simply calculated from the relationship

$$v_s = -\frac{\Delta f c}{f_0} \tag{1.2}$$

where v_s is the radial magnitude of the surface current component, c is the light speed, and f_0 is the radar frequency. Since Δf is either positive or negative in a particular Doppler spectrum, the inverted values for v_s can be positive or negative as well, which represent ocean waves traveling towards or away from the radar look direction, respectively. This discovery alone was a great asset to the field of oceanographic remote sensing, and oceanographers and engineers, encouraged by the potential of HF radars, started to dedicate their time into this area.

At this stage, however, the analysis is limited to short ocean waves because the Bragg waves are mainly metres long in wavelengths, while an accurate description of the sea state relies on the measurement of longer wave components. In 1972, Barrick [15] noticed that the continuum surrounding the first-order peak, which he referred to as the second-order region, is much higher than the remaining noise floor. After close inspection, he concluded that the continuum is actually comprised of reflections from ocean waves of all wavelengths and traveling directions. Therefore, by examining these second-order sea echoes, the directional wave spectrum, which fully describes the sea state, can be extracted.

According to [16, 17], the second-order continuum is produced by two independent effects: an electromagnetic component arising from double-scatters from two distinct waves trains, where the geometry of the waves causes coherent reflections (see Fig. 1.4), and a hydrodynamic component corresponding to a single scatter from second-order ocean waves resulting from the non-linear coupling effects between two first-order waves whose wave vectors must satisfy the relation $\vec{K}_1 + \vec{K}_2 = \vec{K}_B$, with $\vec{K}_B$ being the Bragg wave vector (see Fig. 1.5). Barrick [15] also developed mathematical models to account for these second-order effects, and thereby established a solid foundation for future HF radar investigations.

1.2.2 Research on the Development of Cross Sections

While the material presented in the previous section gives the general ideas involved in using HF radars to remotely probe the ocean surface, further understanding of the interaction between radar waves and ocean waves requires the development of a

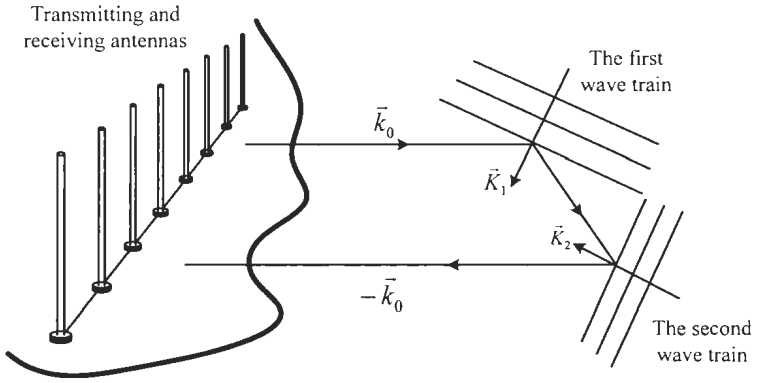

Figure 1.4: Electromagnetic double-scattering. The incident radar wave vector is indicated by $\vec{k}_0$, and the backscattered wave vector is denoted as $-\vec{k}_0$.

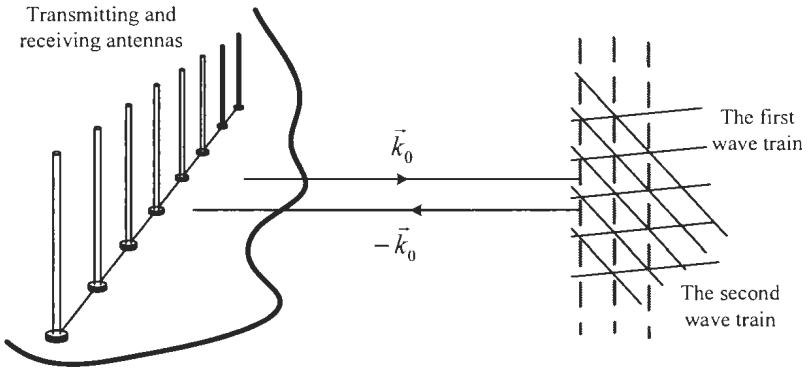

Figure 1.5: Hydrodynamic scattering. Two first order waves (black) interact through non-linear effects to produce a second order wave (red dashed lines). The new formed wave has a wave vector $\vec{K}_B = \vec{K}_1 + \vec{K}_2$, and $\vec{K}_B$ must satisfy the Bragg scatter condition.

radar cross section model. The formal definition of the radar cross section is "the area which, when multiplied by the power flux density of the incident wave, would yield sufficient power that could produce by isotropic radiation, the same radiation intensity as that in a given direction from the scattering surface" [18].

Barrick was the first to derive a complete cross section model for the ocean surface to second order. By employing the effective surface impedance at grazing incidence [19], he examined the exact propagation losses of EM waves due to surface roughness in the HF and VHF bands [20]. In his subsequent analysis, Barrick formulated

a first-order HF scattering cross section by extending Rayleigh's perturbation model [21] to include a slightly rough sea surface [22]. This model successfully verified Crombie's [12] experimental deductions. Later in the same year, Barrick [15] modelled the second-order backscatter from the ocean surface with a non-linear, two dimensional Fredholm-type integral equation. As noted, the second-order backscatter actually contain one scatter from a second-order ocean wave and two successive scatters from two first-order ocean waves, which are indicated by the hydrodynamic and electromagnetic coupling coefficients, respectively. To illustrate the effects, two directional wave height spectra were used to originate the required wave components, and a Dirac delta function was employed to constrain the manner through which the wave vectors are related, i.e., $\vec{K}_1 + \vec{K}_2 = \vec{K}_B$.

Largely based on these initial efforts, Barrick published widely in refining and extending the existing models. For example, in 1980, Lipa and Barrick [23] noticed very narrow spikes in the higher-order structure adjacent to the first-order peaks. These spikes are indicative of ocean waves with very limited, high frequency spectral components, which match the features of long period swell. By assuming a cardioid distribution in direction and a Gaussian distribution in wave frequency for the swell spectrum, a general cross section model to account for such a mixed ocean surface was proposed. Also, in 1986, Barrick and Lipa [24] produced a new hydrodynamic coupling coefficient for shallow water applications and demonstrated its validity against measured data.

Although Barrick's models are the most accepted and studied in the area of HF marine radar technology, it must be noted that all his techniques are based on the assumption of a plane wave as the incident wave field. Consequently, the Bragg scatter mechanism are accounted for by Dirac delta functions in the cross section equations, which suggests the Bragg peaks to be infinitesimal in width and infinite in

amplitude. However, this is not the case in real Doppler spectra. Such a discrepancy is conventionally attributed to surface currents structures or external noise. While these factors do play a role in broadening the Bragg peaks, they do not explain the underlying cause satisfactorily.

The first analysis which addresses the Bragg peak broadening in a fundamental manner was conducted by Walsh and Donnelly [25]. They studied the problem of EM wave scatter at the boundary of two different media based on a generalized function approach. The solutions were shown to agree with classical methods, with the major difference being that the boundary conditions evolve directly from the formulation as auxiliary equations. Later, Walsh and his colleagues (Srivastava, Dawe, Howell, and Gill) further applied the generalized function approach to the problem of ocean surface scatter under the assumption of a pulsed radar waveform [26, 27]. As a result, the Bragg scatter mechanism was shown to be better modeled as a finite squared sinc function, rather than a Dirac delta function. This new cross section model is more realistic than the traditional ones, as the appearance of this squared sinc function accounts for a finite width of the scattering patch on the ocean surface and a signal of finite bandwidth. The corresponding cross section has a finite width for the Bragg peak just as in real practice.

By extending the techniques, Walsh and his colleagues successfully developed a variety of cross section models for different practical situations. During 2000-2001, bistatic first- and second-order radar cross sections of the time-varying ocean surface were derived [27, 28, 29]. These contain the earlier monostatic result as a special case with the bistatic angle set to zero. The other significant contributions include the HF radar cross section for a Frequency Modulated Continuous Wave (FMCW) waveform [30], the combined sea clutter and noise model [31], the study on Bragg fluctuations due to the randomness of ocean surfaces [32], the HF cross section model

incorporating antenna barge motion [33], and a new form of cross sections for swell-contaminated seas [34, 35, 36]. These works serve as a solid theoretical foundation for the primary content of this thesis.

1.2.3 Present Inversion Algorithms

With the first- and second-order backscatter cross section models established [15], investigators started to interpret the HF radar sea echoes using a variety of methods. Barrick [37, 38] first presented general techniques to extract non-directional ocean wave data. An important step in his inversion algorithm was to remove the path gains and losses from the second-order region by normalizing to the first-order spectral power. As noted, the test results were proved to be relatively insensitive to direction. In 1978, Lipa [39, 40] showed that directional features of the ocean spectrum can be indeed derived from the second-order echo. She first reduced the double integral of the second-order model into a set of linear equations, and then applied the regularization methods of Phillips [41] and Twomey [42] to solve the equations. Barrick and Lipa [43] consolidated this algorithm by applying a similar procedure to a broad beam system composed of a cross-loop antenna and a monopole, which they named the Coastal Ocean Dynamics Application Radar (CODAR). Reasonable results were obtained from the experiments. Since then, this linearisation scheme has been rigorously applied to CODAR systems.

An important constraint of the techniques described above is that the analysis of the Doppler spectrum is narrowed down to the frequency band surrounding the Bragg peaks. This is due to the assumption of a one-on-one mapping relationship between a certain ocean wave frequency and a radar Doppler frequency, which is only valid for those Doppler frequencies close to the first-order peaks. Thus, the frequency range for the extracted wave spectrum is severely limited, especially when low HF radar

frequencies are used. In view of this, such inversion scheme was only applied to high HF (i.e., 15-30 MHz) measurements. However, doing so could significantly reduce the range capability of the instrument, or even smear the first-order Bragg returns and make the calculation impossible.

Recognizing the need to extend the frequency range that can be used, Wyatt [44] suggested an improved model-fitting technique based on Lipa and Barrick's work [45]. Basically, Wyatt created many simulated Doppler spectra for a variety of sea states, and real radar data are matched with the simulation using a least squares manner. This method gave accurate estimates as long as the dominant wave direction is not perpendicular to the incident wave direction. Also, tests using this method revealed that a two radar system may provide higher accuracy than a single radar station, and the use of two radars eliminates the usual left/right directional ambiguity associated with single radar systems. However, a consequence is that a noticeable over-prediction in amplitude of the wave height is often observed.

The most recent inversion algorithms were proposed by Gill and Walsh [46] and Howell and Walsh [47]. The basis of this technique, similar to Barrick and Lipa's, is to numerically approximate the integral equation representing the second-order radar cross section as a equation in which the Fourier coefficients of the ocean spectrum are the unknowns. A novel singular value decomposition approach is then applied to invert the kernel matrix to yield the ocean Fourier coefficients. To validate the algorithm, Howell implemented his technique on Barrick's classic model [15] and Walsh's new one [26], and very good results were produced for both cases. Particularly, results based on Walsh's cross section model agreed even better with *in situ* data.

Up to this stage, it should be noted that all techniques introduced sought to address the extraction of wind wave parameters from Doppler spectra, while the research on long period swell was not so rigorously conducted. The initial effort in this area was

made by Lipa and Barrick [23], who suggested that the positions and amplitudes of the higher-order swell peaks are closely related with the dominant swell period, direction and wave height. Moreover, the swell inversion can be viewed as independent from that for local wind wave parameters. Thus, by identifying the swell peaks in the Doppler spectrum, various parameters regarding the incoming swell can be extracted without applying the general inversion techniques to the whole Doppler spectrum.

Although Lipa and Barrick [48] conducted three separate narrow-beam HF radar experiments on the Pacific Ocean in order to validate their swell inversion algorithms, it was later found by Bathgate [49] that these routines are not so robust since the precise positions of swell peaks are often difficult to resolve and are susceptible to external noise. Bathgate then presented an alternative approach based on the frequency modulation effects imposed on Bragg waves by swell. He also conducted a case study at Tweed Heads, Australia, and proved the method to be fast and effective. However, since the data set collected in [49] has little variation in both swell periods and wave height, the generality of this simplified method remains untested.

1.3 Scope of the Thesis

In this thesis, a new monostatic HF radar cross section model for swell-contaminated seas is established based on the fundamental electric field equations appearing in [26]. The non-linear hydrodynamic coupling effects between local wind waves and incoming swell are particularly investigated and are proven to be the major cause for the second-order swell peaks in the backscatter Doppler spectrum. A data interpretation algorithm for the extraction of swell parameters is also developed and tested. As noted, the primary content in this work is based on the theoretical analysis developed by Walsh and his colleagues over the past two decades.

Chapter 2 starts with electric field equations describing the scatter received from a general rough time-varying ocean surface. The current excitation is a pulsed sinusoid on a vertical dipole. Strictly, the first-order E-field contains two portions: 1) a scatter from a single train of first-order ocean wave and 2) a single scatter from a second-order wave train formed by two independent first-order waves. The latter portion is then considered in conjunction with the second-order E-field, which describes successive double scatters. To introduce the concept of swell contamination on local wind waves, a three-dimensional Fourier series, consisting of contributions from swell and wind waves, is used to represent the rough ocean surface. By assuming the surface to be stationary and homogeneous within each range cell that is interrogated, one can easily obtain the auto- and cross-correlations of the various E-field components, and the Doppler power spectral density is then calculated through a Fourier transform. The remainder of Chapter 2 is devoted to calculating the cross sections for different sea states, and to examining the effects of changing the input parameters. It must be noted that for the purpose of demonstration, deep water is assumed for all cases, though the results can be easily extended to general depths.

In Chapter 3, the derived cross section model is extended to the FMCW waveform. The results are then depicted and compared to those for the pulsed waveform. This is a crucial step as the field data to be examined in real world is collected by radars operating in FMCW mode.

In Chapter 4, the received radar time series with external white Gaussian noise is first simulated based on the analysis presented in Chapter 2, from which the Doppler spectrum is obtained as a periodogram. Next, following the techniques described by Bathgate [50], all swell peaks in the spectrum are identified and processed with a robust peak recognition routine, and the positions of those peaks are used to calculate the period and dominant direction of the swell. The half-power width of each swell

peak is extracted in order to derive the frequency spreading of the unknown swell wave height spectrum. Finally, a maximum likelihood method is applied to the swell peak amplitudes to determine the significant wave height and directional spreading of swell. The performance of the algorithm is tested on substantial simulated Doppler spectra.

Chapter 5 summarizes the fundamental conclusions from the previous three chapters. Some constraints related to this thesis, as well as a few obvious suggestions for future research are also presented there.

Chapter 2

The HF Radar Cross Sections of Swell-contaminated Seas for a Pulsed Source

The goal in this chapter is to develop the monostatic HF radar cross sections of swell-contaminated seas. The initial step is to develop the electric field equations received from a random time-varying ocean surface, as has been done in [26]. Next, the specific scenario of swell contamination will be characterized via a three-dimensional Fourier series - two-dimensional in space and one in time. During this step, the hydrodynamic coupling effects between the incoming swell and local wind waves are highlighted via two different manners, which leads to two Fourier representations of the ocean surface. Upon determining the mathematical form of the ocean surface containing a mixture of swell and wind waves, the associated equations of the scattered E-field can be obtained, whose power spectral density (PSD) is then calculated through an autocorrelation and Fourier transform. The radar cross sections, which contain both first- and second-order portions, are easily derived by examining the obtained PSDs

against the monostatic radar range equation.

Some of the key features of the cross sections are discussed in Section 2.4. Effects of different local sea states and radar parameters are investigated. To do so, we simply change the input variables one at a time (such as swell period, direction and significant wave height) and illustrate the responses in the Doppler spectrum. Overall, the simulation results shown at the end of this chapter clearly suggest the possibility of a fast and stable algorithm for swell extraction, which will be introduced in Chapter 4.

2.1 The Electric Field Equations for Scatters From a Random Time-varying Ocean Surface

The fundamental analysis for the received electric field components, scattered from the ocean surface due to a radiation from a vertical dipole source, can be found initially in [26] and also appeared later in [27, 28, 29]. In these works, the ocean surface is defined to be random, rough, and time-varying, which means our study that involves swell can be also included as a special, less general case. Thus, it is possible for us to estimate the form of the E-field received from swell-contaminated seas without having to re-derive a completely new set of equations from first principles. Still, certain assumptions regarding the mixed ocean surface should be invoked: 1) small slopes, where the powers of the surface slope which are greater than unity (for a single scatter) are neglected; 2) small surface heights, where the product of the radar wave number and surface height is taken to be much less than unity; 3) the random surface can be viewed as a zero-mean Gaussian process even after the swell component is incorporated. These assumptions, as well as the specific simplifications they introduce to the mathematical analysis, are discussed extensively in the previously cited open

literature and are not repeated here. Now, the scattered field, E_n, normal to the surface and in the limit as the surface is approached from above, may be cast as (e.g. [27])

$$E_n - \left\{ \nabla\xi \cdot \nabla(E_n) \overset{xy}{*} F(\rho)\frac{e^{-jk_0\rho}}{2\pi\rho} \right\} = C_0 F(\rho)\frac{e^{-jk_0\rho}}{2\pi\rho} \tag{2.1}$$

where $C_0 = (I_0\Delta l k^2)/(j\omega_0\epsilon_0)$ is a constant for a dipole of length Δl carrying a current I_0 whose radian frequency is ω_0 and whose wavenumber is k_0 in a space for which the permittivity is ϵ_0. ρ denotes the distance of a general point (x, y) on the surface ξ measured from the origin, and $F(\rho)$ is the usual Sommerfeld attenuation function. The ∇ operator in (2.1) indicates gradients in the x-y plane, and $\overset{xy}{*}$ indicates a two-dimensional spatial convolution. It should be noted that E_n in (2.1) actually contains electric field components of all orders, i.e.,

$$E_n = (E_n)_0 + (E_n)_1 + (E_n)_2 + \cdots \tag{2.2}$$

where $(E_n)_0$ is the zero-order term representing the EM wave propagation over a smooth plane surface, and the remaining terms are scatters of higher orders indicated by the corresponding subscripts. In this thesis, only the first- and second-order E-fields are analysed, while the higher orders are neglected due to their relatively small contribution to the received E-field.

Following the same procedure as described in earlier papers (see [27, 28, 29]), it is straightforward to deduce the first- (i.e. for a single scatter) and second-order (i.e. for a double scatter) backscatter electric field equations in the time domain as

$$(E_n)_1(t) = -j\eta_0\Delta l\Delta\rho I_0 k_0^2 \frac{F^2(\rho)}{(2\pi\rho)^{3/2}} e^{-j\frac{\pi}{4}} e^{jk_0\Delta\rho} \sum_{\vec{K},\omega} {}_T P_{\vec{K},\omega} \sqrt{K} e^{j\omega t} e^{j\rho K} \mathrm{Sa}\left[\frac{\Delta\rho}{2}(K - 2k_0)\right] \tag{2.3}$$

$$(E_n)_2(t) = -j\eta_0 \Delta l \Delta\rho I_0 k_0^2 \frac{F^2(\rho)}{(2\pi\rho)^{3/2}} e^{-j\frac{\pi}{4}} e^{jk_0\Delta\rho} \cdot \sum_{\vec{K}_1,\omega_1} \sum_{\vec{K}_2,\omega_2} {}_E\Gamma_{pT} P_{\vec{K}_1,\omega_1 T} P_{\vec{K}_2,\omega_2} \sqrt{K_T} e^{j(\omega_1+\omega_2)t} e^{j\rho K_T} \mathrm{Sa}\left[\frac{\Delta\rho}{2}(K_T - 2k_0)\right] \quad (2.4)$$

where η_0 is the intrinsic impedance of free space, $\mathrm{Sa}(\cdot)$ is the usual sampling function, $\Delta\rho$ is the scattering "patch width" for pulsed signals, ${}_E\Gamma_p$ is the electromagnetic coupling coefficient for patch scatters in a symmetric form [26], and $\vec{K}_T = \vec{K}_1 + \vec{K}_2$ refers to a wave vector that lies along the radar look direction. The key term in (2.3) and (2.4), ${}_T P_{\vec{K},\omega}$, represents the total Fourier coefficient of the general sea surface and will be specified in the next section. It should be pointed out that there is actually a second term in the above expressions containing factors in the form of $e^{j\frac{\pi}{4}} e^{-jk_0\Delta\rho}$, but it is negligible because of the rapidly decaying sampling function [26].

2.2 Cross Sections with No Coupling Effects Involved between Swell and Wind Waves

2.2.1 Specification of the Ocean Surface and the Corresponding Backscattered *E*-field

In order to model the backscattered signal, the properties of the random ocean surface must be first specified. As in [26], here the general surface (with or without the background swell component) is represented by a three-dimensional Fourier series,

$$\xi(\vec{\rho}, t) = \sum_{\vec{K},\omega} {}_T P_{\vec{K},\omega} e^{j(\vec{\rho}\cdot\vec{K} + \omega t)} \quad (2.5)$$

with $\vec{K}$ and ω being the wave vector and angular frequency of a certain wave train. It must be understood that the Fourier coefficients, ${}_TP_{\vec{K},\omega}$, fully describes the ocean surface, $\xi(\vec{\rho},t)$, and can be inverted through

$$ {}_TP_{\vec{K},\omega} = \frac{1}{L^2T} \int_{-\frac{L}{2}}^{\frac{L}{2}} \int_{-\frac{L}{2}}^{\frac{L}{2}} \int_{-\frac{T}{2}}^{\frac{T}{2}} \xi(\vec{\rho},t) e^{-j(\vec{\rho}\cdot\vec{K}+\omega t)} \, dx\, dy\, dt \tag{2.6} $$

where L is the fundamental wavelength of the surface and T is the fundamental period.

Meanwhile, the surface ξ defined in (2.5) is actually the sum of all orders of surface displacement so that we may expand it to second order as

$$ \xi(\vec{\rho},t) = {}_1\xi(\vec{\rho},t) + {}_2\xi(\vec{\rho},t) \tag{2.7} $$

where ${}_1\xi(\vec{\rho},t)$ denotes the contribution from first-order linear gravity waves, and ${}_2\xi(\vec{\rho},t)$ accounts for second-order non-linear waves. Naturally, this expansion will be reflected in the Fourier series and, to second order, the Fourier coefficients will be of the form

$$ {}_TP_{\vec{K},\omega} = {}_{T1}P_{\vec{K},\omega} + {}_{T2}P_{\vec{K},\omega} \quad . \tag{2.8} $$

In addition, by following the perturbational analysis proposed by Hasselmann [51], the second-order Fourier coefficients, ${}_{T2}P_{\vec{K},\omega}$, may be conveniently written in terms of products of two first-order coefficients (${}_{T1}P_{\vec{K},\omega}$) and a hydrodynamic coupling coefficient, ${}_H\Gamma_p$, as

$$ {}_{T2}P_{\vec{K},\omega} = \sum_{\substack{\vec{K}_1+\vec{K}_2=\vec{K} \\ \omega_1+\omega_2=\omega}} {}_H\Gamma_p {}_{T1}P_{\vec{K}_1,\omega_1} {}_{T1}P_{\vec{K}_2,\omega_2} \quad . \tag{2.9} $$

This form emphasizes the relationship between the first- and second-order wave vectors to indicate the fact that a second-order gravity wave actually arises from the sum of two first-order components. The hydrodynamic coupling coefficient, ${}_H\Gamma_p$, accounts

for the manner through which the first-order waves interact with each other. The exact form of ${}_H\Gamma_p$ was given explicitly in [29] as

$$ {}_H\Gamma_p(\vec{K}_1, \vec{K}_2) = \frac{1}{2}\left\{ K_1 + K_2 + \frac{g}{\omega_1\omega_2}\left(K_1K_2 - \vec{K}_1 \cdot \vec{K}_2 \right) \times \left[\frac{gK + (\omega_1 + \omega_2)^2}{gK - (\omega_1 + \omega_2)^2} \right] \right\} \quad (2.10) $$

where K_1 and K_2 are magnitudes of $\vec{K}_1$ and $\vec{K}_2$, respectively. It is worthy of note that ${}_H\Gamma_p$ is in a symmetric form.

Having specified the ocean surface in a general sense, we are at a position to examine the potential underlying swell component. The first thing to consider, of course, is what might happen when the long-period swell "merges" with the short-period wind waves. In fact, such non-linear interaction between swell and wind waves is quite controversial due to its complexity. Even the most sophisticated wave models up to date cannot fully explain the mechanism behind the coupling process [52]. Therefore, some oceanographers suggested to ignore it when modeling the sea surface [53]. To confirm if this interaction is truly negligible, we first assume that there is no coupling effects between swell and wind waves so that the total Fourier coefficient ${}_TP_{\vec{K},\omega}$ can be expanded linearly as

$$ {}_TP_{\vec{K},\omega} = {}_SP_{\vec{K},\omega} + {}_WP_{\vec{K},\omega} \quad (2.11) $$

where ${}_SP_{\vec{K},\omega}$ and ${}_WP_{\vec{K},\omega}$ denote the contribution from swell and wind waves, respectively. As in (2.8) and (2.9), ${}_SP_{\vec{K},\omega}$ and ${}_WP_{\vec{K},\omega}$ in (2.11) also represent the sum of all orders of surface displacement, which can be written to second-order as

$$ {}_TP_{\vec{K},\omega} = ({}_{S1}P_{\vec{K},\omega} + {}_{S2}P_{\vec{K},\omega}) + ({}_{W1}P_{\vec{K},\omega} + {}_{W2}P_{\vec{K},\omega}) \quad (2.12) $$

which immediately leads to

$$
\begin{aligned}
{}_{T}P_{\vec{K},\omega} = &\left({}_{S1}P_{\vec{K},\omega} + \sum_{\substack{\vec{K}_1+\vec{K}_2=\vec{K} \\ \omega_1+\omega_2=\omega}} {}_{H}\Gamma_{pS1}\, {}_{S1}P_{\vec{K}_1,\omega_1}\, {}_{S1}P_{\vec{K}_2,\omega_2} \right) \\
&+ \left({}_{W1}P_{\vec{K},\omega} + \sum_{\substack{\vec{K}_1+\vec{K}_2=\vec{K} \\ \omega_1+\omega_2=\omega}} {}_{H}\Gamma_{pW1}\, {}_{W1}P_{\vec{K}_1,\omega_1}\, {}_{W1}P_{\vec{K}_2,\omega_2} \right) \quad . \qquad (2.13)
\end{aligned}
$$

It is clear that (2.13) accounts for only linear effects between the swell and wind wave components, since no cross related terms (e.g., ${}_{S1}P_{\vec{K},\omega}\, {}_{W1}P_{\vec{K},\omega}$) are involved. Another crucial point is that in (2.13), the random surface variables, ${}_{S1}P_{\vec{K},\omega}$ and ${}_{W1}P_{\vec{K},\omega}$, are considered to be independent from each other, because they are physically generated by two wind fields separated by very large distances. The implication of this consideration is later discussed in Appendix A.1.

By substituting (2.13) into (2.3), we obtain the first-order E-field as

$$
\begin{aligned}
(E_n)_1(t) = &-j\eta_0 \Delta l \Delta\rho I_0 k_0^2 \frac{F^2(\rho)}{(2\pi\rho)^{3/2}} e^{-j\frac{\pi}{4}} e^{jk_0\Delta\rho} \\
&\cdot \Bigg\{ \Bigg[\sum_{\vec{K},\omega} \left({}_{S1}P_{\vec{K},\omega} + {}_{W1}P_{\vec{K},\omega} \right) \sqrt{K} e^{j\omega t} e^{j\rho K} \mathrm{Sa}\left[\frac{\Delta\rho}{2}(K - 2k_0) \right] \Bigg] \\
&+ \Bigg[\sum_{\vec{K}_1,\omega_1} \sum_{\vec{K}_2,\omega_2} {}_{H}\Gamma_p \left({}_{S1}P_{\vec{K}_1,\omega_1}\, {}_{S1}P_{\vec{K}_2,\omega_2} + {}_{W1}P_{\vec{K}_1,\omega_1}\, {}_{W1}P_{\vec{K}_2,\omega_2} \right) \\
&\cdot \sqrt{K_T} e^{j(\omega_1+\omega_2)t} e^{j\rho K_T} \mathrm{Sa}\left[\frac{\Delta\rho}{2}(K_T - 2k_0) \right] \Bigg] \Bigg\} \quad . \qquad (2.14)
\end{aligned}
$$

As usual, we have the constraint that $\vec{K}_T = \vec{K}_1 + \vec{K}_2$, and both $\vec{K}$ and $\vec{K}_T$ shall lie along the radar look direction, while $\vec{K}_1$ and $\vec{K}_2$ have no such restrictions. After a close examination of (2.14), we notice that while the single summation (the second line) refers to a single scatter from first-order ocean waves, the double summation (the third and fourth line) is clearly indicative of higher order effects. Moreover, this

double sum is almost identical with equation (2.4) for double scatters from two first-order wave trains. Thus, for later differentiation, only the first summation appearing in (2.14) will be referred to as the first-order electric field, and the remaining double sum will be appropriately addressed later in conjunction with (2.4). To emphasize this new order arrangement, we rewrite (2.14) into two distinct portions as

$$(E_n)_1(t) = -j\eta_0 \Delta l \Delta\rho I_0 k_0^2 \frac{F^2(\rho)}{(2\pi\rho)^{3/2}} e^{-j\frac{\pi}{4}} e^{jk_0\Delta\rho} \cdot \left[\sum_{\vec{K},\omega} \left(s_1 P_{\vec{K},\omega} + w_1 P_{\vec{K},\omega} \right) \sqrt{K} e^{j\omega t} e^{j\rho K} \mathrm{Sa}\left[\frac{\Delta\rho}{2}(K - 2k_0) \right] \right] \tag{2.15}$$

and

$$ {}_H(E_n)_2(t) = -j\eta_0 \Delta l \Delta\rho I_0 k_0^2 \frac{F^2(\rho)}{(2\pi\rho)^{3/2}} e^{-j\frac{\pi}{4}} e^{jk_0\Delta\rho} \cdot \left[\sum_{\vec{K}_1,\omega_1} \sum_{\vec{K}_2,\omega_2} {}_H\Gamma_p \left(s_1 P_{\vec{K}_1,\omega_1} s_1 P_{\vec{K}_2,\omega_2} + w_1 P_{\vec{K}_1,\omega_1} w_1 P_{\vec{K}_2,\omega_2} \right) \cdot \sqrt{K_T} e^{j(\omega_1+\omega_2)t} e^{j\rho K_T} \mathrm{Sa}\left[\frac{\Delta\rho}{2}(K_T - 2k_0) \right] \right] \quad . \tag{2.16}$$

It should be noted that the subscript, H, of ${}_H(E_n)_2(t)$ means that the cause for (2.16) is the hydrodynamic coupling effects between two first-order waves. In an effort to avoid confusion, equation (2.16) will be refereed to as the second-order hydrodynamic term from now on.

Having specified the hydrodynamic second-order, we shall next focus on its counterpart in (2.4), the electric field due to a double EM scatter from two successive first-order waves. Similar to the manner that (2.16) is named, henceforth (2.4) will be referred to as the second-order electromagnetic term. Again, by substituting (2.13)

into (2.4), we have

$$
\begin{aligned}
{}_E(E_n)_2(t) = & -j\eta_0 \Delta l \Delta\rho I_0 k_0^2 \frac{F^2(\rho)}{(2\pi\rho)^{3/2}} e^{-j\frac{\pi}{4}} e^{jk_0\Delta\rho} \\
& \cdot \sum_{\vec{K}_1,\omega_1} \sum_{\vec{K}_2,\omega_2} {}_E\Gamma_p \Bigg[\Bigg({}_{S1}P_{\vec{K}_1,\omega_1} + \sum_{\substack{\vec{K}_a+\vec{K}_b=\vec{K}_1 \\ \omega_a+\omega_b=\omega_1}} {}_H\Gamma_{pS1}\, {}_{S1}P_{\vec{K}_a,\omega_a}\, {}_{S1}P_{\vec{K}_b,\omega_b} \Bigg) \\
& + \Bigg({}_{W1}P_{\vec{K}_1,\omega_1} + \sum_{\substack{\vec{K}_a+\vec{K}_b=\vec{K}_1 \\ \omega_a+\omega_b=\omega_1}} {}_H\Gamma_{pW1}\, {}_{W1}P_{\vec{K}_a,\omega_a}\, {}_{W1}P_{\vec{K}_b,\omega_b} \Bigg) \Bigg] \\
& \cdot \Bigg[\Bigg({}_{S1}P_{\vec{K}_2,\omega_2} + \sum_{\substack{\vec{K}_c+\vec{K}_d=\vec{K}_2 \\ \omega_c+\omega_d=\omega_2}} {}_H\Gamma_{pS1}\, {}_{S1}P_{\vec{K}_c,\omega_c}\, {}_{S1}P_{\vec{K}_d,\omega_d} \Bigg) \\
& + \Bigg({}_{W1}P_{\vec{K}_2,\omega_2} + \sum_{\substack{\vec{K}_c+\vec{K}_d=\vec{K}_2 \\ \omega_a+\omega_b=\omega_2}} {}_H\Gamma_{pW1}\, {}_{W1}P_{\vec{K}_c,\omega_c}\, {}_{W1}P_{\vec{K}_d,\omega_d} \Bigg) \Bigg] \\
& \cdot \sqrt{K_T} e^{j(\omega_1+\omega_2)t} e^{j\rho K_T} \mathrm{Sa}\Big[\frac{\Delta\rho}{2}(K_T - 2k_0) \Big]
\end{aligned}
\tag{2.17}
$$

where the electromagnetic coupling coefficient ${}_E\Gamma_p$, according to the analysis in [30], may be written in a symmetrized form as

$$
{}_E\Gamma_p = \frac{\left| \vec{K}_1 \times \vec{K}_2 \right|^2}{2(2k_0)^2 \Big[\sqrt{-\vec{K}_1 \cdot \vec{K}_2} + jk_0\Delta \Big]} \tag{2.18}
$$

with k_0 being the wavenumber of the transmitted EM wave, and Δ being the normalized surface impedance (see, e.g. [19]).

Since the analysis in this thesis is carried only to second-order, we may safely neglect the 3rd and 4th order effects arising from either a double scatter from two second-order waves, or a single scatter from a first-order wave followed by another

from a second-order wave, or vice versa. Therefore, (2.17) reduces to

$$
\begin{aligned}
{}_E(E_n)_2(t) = & -j\eta_0 \Delta l \Delta\rho I_0 k_0^2 \frac{F^2(\rho)}{(2\pi\rho)^{3/2}} e^{-j\frac{\pi}{4}} e^{jk_0\Delta\rho} \sum_{\vec{K}_1,\omega_1} \sum_{\vec{K}_2,\omega_2} {}_E\Gamma_p \\
& \cdot \Big({}_{S1}P_{\vec{K}_1,\omega_1 S1}P_{\vec{K}_2,\omega_2} + {}_{S1}P_{\vec{K}_1,\omega_1 W1}P_{\vec{K}_2,\omega_2} + {}_{W1}P_{\vec{K}_1,\omega_1 S1}P_{\vec{K}_2,\omega_2} + {}_{W1}P_{\vec{K}_1,\omega_1 W1}P_{\vec{K}_2,\omega_2} \Big) \\
& \cdot \sqrt{K_T} e^{j(\omega_1+\omega_2)t} e^{j\rho K_T} \mathrm{Sa}\left[\frac{\Delta\rho}{2}(K_T - 2k_0) \right] \qquad (2.19)
\end{aligned}
$$

Having specified both the hydrodynamic and electromagnetic second-order E-field, it is appropriate to compare the two and regroup them if possible. It is apparent that the major difference between (2.16) and (2.19) lies in the coupling coefficient, ${}_H\Gamma_p$ and ${}_E\Gamma_p$. Thus, we may combine the two to give the complete second-order E-field as

$$
\begin{aligned}
(E_n)_2(t) &= {}_H(E_n)_2(t) + {}_E(E_n)_2(t) \\
&= -j\eta_0 \Delta l \Delta\rho I_0 k_0^2 \frac{F^2(\rho)}{(2\pi\rho)^{3/2}} e^{-j\frac{\pi}{4}} e^{jk_0\Delta\rho} \sum_{\vec{K}_1,\omega_1} \sum_{\vec{K}_2,\omega_2} \Big[2\,{}_E\Gamma_{pS1}P_{\vec{K}_1,\omega_1 W1}P_{\vec{K}_2,\omega_2} \\
&\quad + \Big({}_E\Gamma_p + {}_H\Gamma_p \Big) \Big({}_{S1}P_{\vec{K}_1,\omega_1 S1}P_{\vec{K}_2,\omega_2} + {}_{W1}P_{\vec{K}_1,\omega_1 W1}P_{\vec{K}_2,\omega_2} \Big) \Big] \\
&\quad \cdot \sqrt{K_T} e^{j(\omega_1+\omega_2)t} e^{j\rho K_T} \mathrm{Sa}\left[\frac{\Delta\rho}{2}(K_T - 2k_0) \right] \quad . \qquad (2.20)
\end{aligned}
$$

Note that to reach (2.20), a more compact form is adopted in the square bracket where

$$
\begin{aligned}
& \sum_{\vec{K}_1,\omega_1} \sum_{\vec{K}_2,\omega_2} {}_E\Gamma_p \Big({}_S P_{\vec{K}_1,\omega_1 W} P_{\vec{K}_2,\omega_2} + {}_W P_{\vec{K}_1,\omega_1 S} P_{\vec{K}_2,\omega_2} \Big) \\
& \qquad = \sum_{\vec{K}_1,\omega_1} \sum_{\vec{K}_2,\omega_2} 2\,{}_E\Gamma_{pS} P_{\vec{K}_1,\omega_1 W} P_{\vec{K}_2,\omega_2} \quad , \qquad (2.21)
\end{aligned}
$$

for that the electromagnetic coupling coefficient, ${}_E\Gamma_p$, is in its symmetric form.

Up to this stage, it must be pointed out that in our second-order analysis, only the patch scatter, which refers to the scatters occurring at essentially the same position

remote from the antenna, is discussed. In fact, it was shown in [5] that this patch scatter almost always dominates the second-order effects, while the other components, i.e., double scatters that are widely separated with one of the two near the transmitter or receiver, are generally negligible.

Now, by virtue of (2.15) and (2.20), the total electric field received from the swell-contaminated ocean surface is given by

$$E_n(t) = (E_n)_1(t) + {}_H(E_n)_2(t) + {}_E(E_n)_2(t) = (E_n)_1(t) + (E_n)_2(t) \quad . \tag{2.22}$$

In the next section, (2.22) will be used to develop the power spectral density (PSD) of the received E-field.

2.2.2 The Doppler Power Spectral Density of the Received Electric Field

An important step in arriving at the radar cross sections involves determining the psd of the received electric field, $E_n(t)$, in (2.22). However, before we proceed to find this PSD, a few statistical properties regarding the ocean surface shall be first defined: 1) the ocean surface under investigation can be viewed as a real, zero-mean Gaussian process. As a result, the scattered E-field should be a random process as well, though it does not have to be Gaussian. 2) as is common in oceanographic treatments, the ocean surface shall be taken to be homogeneous and stationary, which suggests that the addition of a constant space vector, $\Delta\vec{\rho}$, or a constant time period, τ, does not affect the surface statistics. Actually, this is a very reasonable assumption, even in real practice, because a typical scattering ocean patch for HF radar applications ranges between 10 to 20 square kilometres, and the time necessary for a significant change to occur on the ocean surface is much greater than the time required for a typical single

radar interrogation, e.g., 15 minutes.

With the fundamental assumptions now clarified, we may proceed to seek the power spectral density of the received E-field through a Fourier transformation of its autocorrelation. Given stationarity, the autocorrelation of a random process will only depend on the time shift, τ, so that we can conveniently express the autocorrelation, $\mathcal{R}$, of the field in (2.22) as [26]

$$\mathcal{R}(\tau) = \frac{A_r}{2\eta_0} < E_n(t+\tau) \cdot E_n^*(t) > \tag{2.23}$$

where the effective aperture of the receiving antenna $A_r = (\lambda_0^2/4\pi)G_r$ [54] with G_r being the gain of the receiving antenna while λ_0 is the free space wavelength of the transmitted EM wave. Also, $*$ represents the complex conjugation, and $< \cdot >$ indicates the ensemble average. The normalization term, $\frac{A_r}{2\eta_0}$, appearing in (2.23) readily equates $\mathcal{R}(0)$ with the average power received from the scattering patch, i.e.

$$\mathcal{R}(0) = \frac{A_r}{2\eta_0} < E_n(t) \cdot E_n^*(t) >= \frac{A_r}{2\eta_0} < |E_n(t)|^2 >= \mathcal{P}_r \quad . \tag{2.24}$$

Now, applying (2.23) to (2.22) renders

$$\mathcal{R}(\tau) = \frac{A_r}{2\eta_0} < \Big[(E_n)_1(t+\tau) + (E_n)_2(t+\tau)\Big] \cdot \Big[(E_n)_1^*(t) + (E_n)_2^*(t)\Big] > \quad . \tag{2.25}$$

Since the ensemble average of a linear summation is equivalent to the sum of the individual averages, we may rewrite (2.25) in a new form as

$$\begin{aligned}\mathcal{R}(\tau) = \frac{A_r}{2\eta_0}\Big\{ &< (E_n)_1(t+\tau)(E_n)_1^*(t) > + < (E_n)_1(t+\tau)(E_n)_2^*(t) > \\ &+ < (E_n)_2(t+\tau)(E_n)_1^*(t) > + < (E_n)_2(t+\tau)(E_n)_2^*(t) > \Big\} \quad .\end{aligned} \tag{2.26}$$

Obviously, (2.26) contains four distinct portions, among which the first and last averages account for the autocorrelation of the individual E-field components, and the intermediate two terms indicate the cross-correlations. It is later shown in Appendix A.3 that the cross-correlated terms equal to zero and can be immediately eliminated from (2.26). Thus, only the remaining two components need to be examined in detail.

2.2.2.1 The First-order Doppler Power Spectral Density

Attention will now be focused on the first term appearing within the braces of (2.26). Since it is simply the autocorrelation of the first-order field due to a single scatter, we use the subscript "1" to define the term as

$$\begin{aligned}
\mathcal{R}_1(\tau) &= \frac{A_r}{2\eta_0} < (E_n)_1(t+\tau)(E_n)_1^*(t) > \\
&= \frac{A_r}{2\eta_0}\Bigg\{ \eta_0^2 \Delta l^2 \Delta\rho^2 |I_0|^2 k_0^4 \frac{F^4(\rho)}{(2\pi\rho)^3} \\
&\quad \cdot \left\langle \left(\sum_{\vec{K},\omega} {}_{S1}P_{\vec{K},\omega} + \sum_{\vec{K},\omega} {}_{W1}P_{\vec{K},\omega} \right) \left(\sum_{\vec{K}',\omega'} {}_{S1}P^*_{\vec{K}',\omega'} + \sum_{\vec{K}',\omega'} {}_{W1}P^*_{\vec{K}',\omega'} \right) \right\rangle \\
&\quad \cdot \sqrt{K}\sqrt{K'} e^{j\omega(t+\tau)} e^{-j\omega' t} e^{j\rho K} e^{-j\rho K'} \mathrm{Sa}\left[\frac{\Delta\rho}{2}(K-2k_0)\right] \mathrm{Sa}\left[\frac{\Delta\rho}{2}(K'-2k_0)\right] \Bigg\} \qquad (2.27)
\end{aligned}$$

where the ensemble average, $< \cdot >$, is performed only on the random variables, ${}_{S1}P_{\vec{K},\omega}$ and ${}_{W1}P_{\vec{K},\omega}$. It is not difficult to see that this ensemble average actually contains four linear portions as

$$\begin{aligned}
&\left\langle \left(\sum_{\vec{K},\omega} {}_{S1}P_{\vec{K},\omega} + \sum_{\vec{K},\omega} {}_{W1}P_{\vec{K},\omega} \right) \left(\sum_{\vec{K}',\omega'} {}_{S1}P^*_{\vec{K}',\omega'} + \sum_{\vec{K}',\omega'} {}_{W1}P^*_{\vec{K}',\omega'} \right) \right\rangle \\
&= \sum_{\vec{K},\omega} \sum_{\vec{K}',\omega'} \left\langle {}_{S1}P_{\vec{K},\omega} {}_{S1}P^*_{\vec{K}',\omega'} + {}_{S1}P_{\vec{K},\omega} {}_{W1}P^*_{\vec{K}',\omega'} + {}_{W1}P_{\vec{K},\omega} {}_{S1}P^*_{\vec{K}',\omega'} + {}_{W1}P_{\vec{K},\omega} {}_{W1}P^*_{\vec{K}',\omega'} \right\rangle
\end{aligned} \qquad (2.28)$$

where the summation and $< \cdot >$ have been interchanged. Obviously, the first and fourth terms from the second line are autocorrelated, while the intermediate two are cross correlated. For the sake of brevity, only the first and second terms shall be detailed in the body of the thesis (see Appendix A.1). By following essentially the same path, the remaining two may be deduced without much effort.

In Appendix A.1, it is shown that

$$< {}_1P_{\vec{K},\omega}{}_1P^*_{\vec{K}',\omega'} >= \begin{cases} \sum_{m=\pm 1} \frac{1}{2} S_1(m\vec{K})\delta(\omega + m\sqrt{gK})d\vec{K}\,d\omega, & \vec{K} = \vec{K}',\ \omega = \omega' \\ 0, & \text{otherwise} \end{cases} \tag{2.29}$$

and that any cross-correlated term involving a swell coefficient and a wind wave coefficient will simply vanish. Therefore, (2.27) can be rewritten in a differential form as

$$\begin{aligned} \mathcal{R}_1(\tau) =& \frac{A_r \eta_0 \Delta l^2 \Delta\rho^2 |I_0|^2 k_0^4}{4} \frac{F^4(\rho)}{(2\pi\rho)^3} \sum_{m=\pm 1} \int_{-\infty}^{\infty} \int_{-\pi}^{\pi} \int_{0}^{\infty} \Big[{}_S S_1(m\vec{K}) + {}_W S_1(m\vec{K}) \Big] \\ & \cdot \delta(\omega + m\sqrt{gK}) K^2 e^{j\omega\tau} \mathrm{Sa}^2\Big[\frac{\Delta\rho}{2}(K - 2k_0)\Big] dK\, d\theta_{\vec{K}}\, d\omega \quad . \end{aligned} \tag{2.30}$$

Note that to reach (2.30), we have employed the fact that

$$d\vec{K}\,d\omega = dK_x\, dK_y\, d\omega = K\, dK\, d\theta_{\vec{K}}\, d\omega \quad . \tag{2.31}$$

Then, the ω integral in (2.30) immediately yields to the delta constraint so that

$$\begin{aligned} \mathcal{R}_1(\tau) =& \frac{A_r \eta_0 \Delta l^2 \Delta\rho^2 |I_0|^2 k_0^4}{4} \frac{F^4(\rho)}{(2\pi\rho)^3} \sum_{m=\pm 1} \int_{-\pi}^{\pi} \int_{0}^{\infty} \Big[{}_S S_1(m\vec{K}) + {}_W S_1(m\vec{K}) \Big] \\ & \cdot K^2 e^{j\omega\tau} \mathrm{Sa}^2\Big[\frac{\Delta\rho}{2}(K - 2k_0)\Big] dK\, d\theta_{\vec{K}} \end{aligned} \tag{2.32}$$

where $\omega = -m\sqrt{gK}$.

Having derived a relatively compact expression for $\mathcal{R}_1(\tau)$, the normalized first-order Doppler power spectral density, or, the power spectrum of the return signal may now be determined via a Fourier transform with respect to τ. Interestingly, the only term in (2.32) that involves the time shift, τ, is $e^{j\omega\tau}$, and we have, from Lathi [55], that

$$\mathcal{F}[e^{j\omega\tau}] = \mathcal{F}[e^{j(-m\sqrt{gK})\tau}] = 2\pi\delta(\omega_d + m\sqrt{gK}) \quad . \tag{2.33}$$

Note that the angular Doppler frequency ω_d, measured in radians per second, is actually the transform variable for τ. In some cases, the Doppler frequency in hertz is more favoured as a scale, which can be simply obtained through $f_d = \omega_d/2\pi$. Now the first-order Doppler spectrum, $\mathcal{P}_1(\omega_d)$, is given by

$$\begin{aligned}\mathcal{P}_1(\omega_d) = \mathcal{F}[\mathcal{R}_1(\tau)] = &\frac{A_r\eta_0\Delta l^2\Delta\rho^2|I_0|^2k_0^4}{16}\frac{F^4(\rho)}{\pi^2\rho^3}\sum_{m=\pm1}\int_{-\pi}^{\pi}\int_{0}^{\infty}\Big[{}_S S_1(m\vec{K}) + {}_W S_1(m\vec{K})\Big] \\ &\cdot K^2\mathrm{Sa}^2\Big[\frac{\Delta\rho}{2}(K-2k_0)\Big]\delta(\omega_d + m\sqrt{gK})\,dK\,d\theta_{\vec{K}} \quad .\end{aligned} \tag{2.34}$$

Noting that the delta constraint in (2.34) actually implies

$$K = \frac{\omega_d^2}{g} \quad \text{so that} \quad dK = \frac{2\omega_d}{g}d\omega_d = \frac{2\sqrt{K}}{\sqrt{g}}d\omega_d \quad , \tag{2.35}$$

we may replace dK in (2.34) with $d\omega_d$ and eliminate the integral over K by resorting to the delta constraint. Now (2.34) may be written as

$$\begin{aligned}\mathcal{P}_1(\omega_d) = &\frac{A_r\eta_0\Delta l^2\Delta\rho^2|I_0|^2k_0^4}{8}\frac{F^4(\rho)}{\pi^2\rho^3}\sum_{m=\pm1}\int_{-\pi}^{\pi}\Big[{}_S S_1(m\vec{K}) + {}_W S_1(m\vec{K})\Big] \\ &\cdot \frac{K^{2.5}}{\sqrt{g}}\mathrm{Sa}^2\Big[\frac{\Delta\rho}{2}(K-2k_0)\Big]d\theta_{\vec{K}} \quad .\end{aligned} \tag{2.36}$$

2.2.2.2 The Second-order Doppler Power Spectral Density

Following the procedure for the first-order case described in section 2.2.2.1, the auto-correlation of the second-order E-field will now be addressed. From (2.20), we may write

$$\mathcal{R}_2(\tau) = \frac{A_r \eta_0 \Delta l^2 \Delta\rho^2 |I_0|^2 k_0^4}{2} \frac{F^4(\rho)}{(2\pi\rho)^3} \cdot \Bigg\{ \sum_{\vec{K}_1,\omega_1} \sum_{\vec{K}_2,\omega_2} \sum_{\vec{K}'_1,\omega'_1} \sum_{\vec{K}'_2,\omega'_2}$$
$$\Bigg\langle \Bigg[\Gamma_p \Big({}_{S1}P_{\vec{K}_1,\omega_1 S1} P_{\vec{K}_2,\omega_2} + {}_{W1}P_{\vec{K}_1,\omega_1 W1} P_{\vec{K}_2,\omega_2} \Big) + 2_E\Gamma_{pS1} P_{\vec{K}_1,\omega_1 W1} P_{\vec{K}_2,\omega_2} \Bigg]$$
$$\cdot \Bigg[\Gamma^*_p \Big({}_{S1}P^*_{\vec{K}'_1,\omega'_1 S1} P^*_{\vec{K}'_2,\omega'_2} + {}_{W1}P^*_{\vec{K}'_1,\omega'_1 W1} P^*_{\vec{K}'_2,\omega'_2} \Big) + 2_E\Gamma^*_{pS1} P^*_{\vec{K}'_1,\omega'_1 W1} P^*_{\vec{K}'_2,\omega'_2} \Bigg] \Bigg\rangle \sqrt{K_T}\sqrt{K'_T}$$
$$\cdot e^{j(\omega_1+\omega_2)(t+\tau)} e^{-j(\omega'_1+\omega'_2)t} e^{j\rho K_T} e^{-j\rho K'_T} \mathrm{Sa}\Big[\frac{\Delta\rho}{2}(K_T - 2k_0)\Big] \mathrm{Sa}\Big[\frac{\Delta\rho}{2}(K'_T - 2k_0)\Big] \Bigg\} \quad (2.37)$$

where $\Gamma_p = {}_E\Gamma_p + {}_H\Gamma_p$ gives the coupling coefficient for the combined electromagnetic and hydrodynamic effects.

If we expand the complex ensemble average into a linear summation, which is tedious but straightforward, we may obtain

$$\Bigg\langle \Bigg[\Gamma_p \Big({}_{S1}P_{\vec{K}_1,\omega_1 S1} P_{\vec{K}_2,\omega_2} + {}_{W1}P_{\vec{K}_1,\omega_1 W1} P_{\vec{K}_2,\omega_2} \Big) + 2_E\Gamma_{pS1} P_{\vec{K}_1,\omega_1 W1} P_{\vec{K}_2,\omega_2} \Bigg]$$
$$\cdot \Bigg[\Gamma^*_p \Big({}_{S1}P^*_{\vec{K}'_1,\omega'_1 S1} P^*_{\vec{K}'_2,\omega'_2} + {}_{W1}P^*_{\vec{K}'_1,\omega'_1 W1} P^*_{\vec{K}'_2,\omega'_2} \Big) + 2_E\Gamma^*_{pS1} P^*_{\vec{K}'_1,\omega'_1 W1} P^*_{\vec{K}'_2,\omega'_2} \Bigg] \Bigg\rangle$$
$$= |\Gamma_p|^2 \Bigg[\Big\langle {}_{S1}P_{\vec{K}_1,\omega_1 S1} P_{\vec{K}_2,\omega_2 S1} P^*_{\vec{K}'_1,\omega'_1 S1} P^*_{\vec{K}'_2,\omega'_2} \Big\rangle + \Big\langle {}_{S1}P_{\vec{K}_1,\omega_1 S1} P_{\vec{K}_2,\omega_2 W1} P^*_{\vec{K}'_1,\omega'_1 W1} P^*_{\vec{K}'_2,\omega'_2} \Big\rangle$$
$$+ \Big\langle {}_{W1}P_{\vec{K}_1,\omega_1 W1} P_{\vec{K}_2,\omega_2 S1} P^*_{\vec{K}'_1,\omega'_1 S1} P^*_{\vec{K}'_2,\omega'_2} \Big\rangle + \Big\langle {}_{W1}P_{\vec{K}_1,\omega_1 W1} P_{\vec{K}_2,\omega_2 W1} P^*_{\vec{K}'_1,\omega'_1 W1} P^*_{\vec{K}'_2,\omega'_2} \Big\rangle \Bigg]$$
$$+ 2\Gamma_{pE}\Gamma^*_p \Bigg[\Big\langle {}_{S1}P_{\vec{K}_1,\omega_1 S1} P_{\vec{K}_2,\omega_2 S1} P^*_{\vec{K}'_1,\omega'_1 W1} P^*_{\vec{K}'_2,\omega'_2} \Big\rangle + \Big\langle {}_{W1}P_{\vec{K}_1,\omega_1 W1} P_{\vec{K}_2,\omega_2 S1} P^*_{\vec{K}'_1,\omega'_1 W1} P^*_{\vec{K}'_2,\omega'_2} \Big\rangle \Bigg]$$
$$+ 2\Gamma^*_{pE}\Gamma_p \Bigg[\Big\langle {}_{S1}P_{\vec{K}_1,\omega_1 W1} P_{\vec{K}_2,\omega_2 S1} P^*_{\vec{K}'_1,\omega'_1 S1} P^*_{\vec{K}'_2,\omega'_2} \Big\rangle + \Big\langle {}_{S1}P_{\vec{K}_1,\omega_1 W1} P_{\vec{K}_2,\omega_2 W1} P^*_{\vec{K}'_1,\omega'_1 W1} P^*_{\vec{K}'_2,\omega'_2} \Big\rangle \Bigg]$$
$$+ 4|{}_E\Gamma_p|^2 \Big\langle {}_{S1}P_{\vec{K}_1,\omega_1 W1} P_{\vec{K}_2,\omega_2 S1} P^*_{\vec{K}'_1,\omega'_1 W1} P^*_{\vec{K}'_2,\omega'_2} \Big\rangle \quad . \quad (2.38)$$

Clearly, an essential step to simplify (2.37) involves resolving these complex $< \cdot >$ that has up to four separate Fourier coefficients. Although (2.38) seems to be awkward at first glance, it is shown in Appendix A.2 that only the averages with all variables from the same wave system as well as the last line in (2.38) will be retained, while the other components may simply reduce to zero. With help from (A.23) and (A.27), we now rewrite (2.37) as

$$\mathcal{R}_2(\tau) = \frac{A_r \eta_0 \Delta l^2 \Delta\rho^2 |I_0|^2 k_0^4}{4} \frac{F^4(\rho)}{(2\pi\rho)^3}$$
$$\sum_{m_1=\pm 1} \sum_{m_2=\pm 1} \int_{-\infty}^{\infty} \int_{-\pi}^{\pi} \int_{0}^{\infty} \int_{-\infty}^{\infty} \int_{-\pi}^{\pi} \int_{0}^{\infty} \Big[|\Gamma_p|^2 \Big({}_S S_1(m_1 \vec{K}_1) {}_S S_1(m_2 \vec{K}_2) + {}_W S_1(m_1 \vec{K}_1) {}_W S_1(m_2 \vec{K}_2) \Big)$$
$$+ 2|{}_E\Gamma_p|^2 \Big({}_S S_1(m_1 \vec{K}_1) {}_W S_1(m_2 \vec{K}_2) \Big) \Big] \delta(\omega_1 + m_1 \sqrt{gK_1}) \delta(\omega_2 + m_2 \sqrt{gK_2})$$
$$\cdot K_T e^{j(\omega_1+\omega_2)\tau} \mathrm{Sa}^2 \Big[\frac{\Delta\rho}{2} (K_T - 2k_0) \Big] K_1 dK_1 d\theta_{\vec{K}_1} d\omega_1 K_2 dK_2 d\theta_{\vec{K}_2} d\omega_2 \tag{2.39}$$

where the relation in (2.31) is again employed. By solving the delta constraint in (2.39) and converting the $\vec{K}_2$ integration into an integral over $\vec{K}_T$ with the stipulation that $\vec{K}_2 = \vec{K}_T - \vec{K}_1$ so that $d\vec{K}_2 = d\vec{K}_T$ [5], the autocorrelation may be further simplified as

$$\mathcal{R}_2(\tau) = \frac{A_r \eta_0 \Delta l^2 \Delta\rho^2 |I_0|^2 k_0^4}{4} \frac{F^4(\rho)}{(2\pi\rho)^3}$$
$$\cdot \sum_{m_1=\pm 1} \sum_{m_2=\pm 1} \int_{-\pi}^{\pi} \int_{0}^{\infty} \int_{-\pi}^{\pi} \int_{0}^{\infty} \Big[|\Gamma_p|^2 \Big({}_S S_1(m_1 \vec{K}_1) {}_S S_1(m_2 \vec{K}_2) + {}_W S_1(m_1 \vec{K}_1) {}_W S_1(m_2 \vec{K}_2) \Big)$$
$$+ 2|{}_E\Gamma_p|^2 \Big({}_S S_1(m_1 \vec{K}_1) {}_W S_1(m_2 \vec{K}_2) \Big) \Big] K_T^2 K_1 e^{j(\omega_1+\omega_2)\tau}$$
$$\cdot \mathrm{Sa}^2 \Big[\frac{\Delta\rho}{2} (K_T - 2k_0) \Big] dK_1 d\theta_{\vec{K}_1} dK_T d\theta_{\vec{K}_T} \tag{2.40}$$

with $\omega_1 = -m_1 \sqrt{gK_1}$ and $\omega_2 = -m_2 \sqrt{gK_2}$. Of course, the key stipulations that $\vec{K}_T = \vec{K}_1 + \vec{K}_2$ and $\omega = \omega_1 + \omega_2$ still apply, with $\vec{K}_T$ lying along the radar look direction.

Also, since (2.40) is the autocorrelation of the second-order E-field associated with patch scatter only, the surface components that form the second-order ocean waves, which are here denoted by wave vectors $\vec{K}_1$ and $\vec{K}_2$, are expected to be found within the same remote ocean patch.

Next, following exactly the same procedure as for the first-order scatter, a Fourier transform on (2.40) with respect to τ is performed, and the second-order power spectral density, $\mathcal{P}_2(\omega_d)$, can be written analogously to (2.34) as

$$\begin{aligned}
\mathcal{P}_2(\omega_d) &= \frac{A_r \eta_0 \Delta l^2 \Delta\rho^2 |I_0|^2 k_0^4}{16} \frac{F^4(\rho)}{\pi^2 \rho^3} \\
&\cdot \sum_{m_1=\pm 1} \sum_{m_2=\pm 1} \int_{-\pi}^{\pi} \int_{0}^{\infty} \int_{-\pi}^{\pi} \int_{0}^{\infty} \Big[|\Gamma_p|^2 \Big({}_S S_1(m_1 \vec{K}_1) {}_S S_1(m_2 \vec{K}_2) + {}_W S_1(m_1 \vec{K}_1) {}_W S_1(m_2 \vec{K}_2) \Big) \\
&+ 2 |{}_E \Gamma_p|^2 \Big({}_S S_1(m_1 \vec{K}_1) {}_W S_1(m_2 \vec{K}_2) \Big) \Big] \delta(\omega_d + m_1 \sqrt{g K_1} + m_2 \sqrt{g K_2}) \\
&\cdot K_T^2 K_1 \mathrm{Sa}^2 \Big[\frac{\Delta\rho}{2} (K_T - 2k_0) \Big] dK_1 d\theta_{\vec{K}_1} dK_T d\theta_{\vec{K}_T} \quad . \qquad (2.41)
\end{aligned}$$

Based on these results, the overall monostatic Doppler PSD, $\mathcal{P}(\omega_d)$, of the received signal from swell-contaminated seas may be simply written as

$$\mathcal{P}(\omega_d) = \mathcal{P}_1(\omega_d) + \mathcal{P}_2(\omega_d) \qquad (2.42)$$

where the two components on the right hand side are given by (2.36) and (2.41), respectively.

2.2.3 Derivation of the Cross Sections for the "No Coupling" Case

Since the radar cross section, $\sigma(\omega_d)$, that we seek here is the average cross section per unit area, we shall first normalize the PSD in (2.42) to the scattering ocean patch area.

It is seen from Fig. 2.1 that for a scattering region dictated by a range resolution, $\Delta\rho$, and beamwidth, $d\theta_N$, at an observation range, ρ, the elemental area may be approximated by

$$dA \approx \rho \Delta\rho d\theta_N \quad . \tag{2.43}$$

It must be noted that for the first-order scatter and the second-order patch scatter discussed in the previous section, θ_N in (2.43) is precisely the direction $\theta_{\vec{K}}$ in (2.36) or $\theta_{\vec{K}_T}$ in (2.41), which both correspond to the radar look direction.

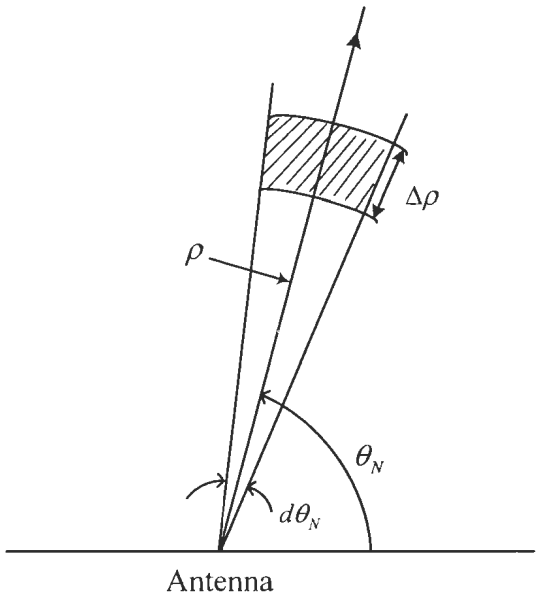

Figure 2.1: The general geometry of the scattering ocean patch

Next, a key step leading to the cross sections involves the consideration of the monostatic radar range equation (see, for example, Barton [56]). In our case where the cross section is normalized to dA, we may accordingly express the radar range equation in an incremental form as

$$\frac{d\mathcal{P}(\omega_d)}{dA} = \frac{\lambda_0^2 P_t G_t G_r F^4(\rho)}{(4\pi)^3 \rho^4} \sigma(\omega_d) \tag{2.44}$$

where $\sigma(\omega_d)$ is the cross section being sought, P_t is the transmitted power, and G_t and G_r are the free space gains of the transmitter and receiver, respectively. The product of these three may be expressed more explicitly with the specific antenna parameters, i.e., for the elementary vertical dipole assumed in this thesis,

$$P_t G_t G_r = \frac{\eta_0 k_0^2 \Delta l^2 |I_0|^2}{12\pi} \cdot \frac{3}{2} \cdot \frac{4\pi A_r}{\lambda_0^2} \tag{2.45}$$

where A_r has already been defined in (2.23) as the effective free space aperture of the receiving antenna. Combining the equations presented above, (2.44) now takes a new form as

$$\frac{d\mathcal{P}(\omega_d)}{dA} = \frac{A_r \eta_0 \Delta l^2 |I_0|^2 k_0^2 F^4(\rho)}{128\pi^3 \rho^4} \sigma(\omega_d) \quad . \tag{2.46}$$

where $\sigma(\omega_d)$ actually contains two parts consistent with (2.42) as

$$\sigma(\omega_d) = \sigma_1(\omega_d) + \sigma_2(\omega_d) \tag{2.47}$$

and the subscript 1 and 2 intuitively represent the first-order and second-order radar cross sections.

Finally, based on the power spectral densities developed in (2.42) and the monostatic radar range equation in (2.46), the expressions for the various radar cross section components will be presented. Given the fact that $d\theta_N \equiv d\theta_{\vec{K}}$, we may compare (2.36) with (2.46) to give

$$\begin{aligned} \frac{d\mathcal{P}_1(\omega_d)}{dA_p} &= \frac{A_r \eta_0 \Delta l^2 \Delta\rho |I_0|^2 k_0^4}{8} \frac{F^4(\rho)}{\pi^2 \rho^4} \sum_{m=\pm 1} \Big[{}_S S_1(m\vec{K}) + {}_W S_1(m\vec{K}) \Big] \\ &\quad \cdot \frac{K^{2.5}}{\sqrt{g}} \mathrm{Sa}^2\Big[\frac{\Delta\rho}{2}(K - 2k_0)\Big] \\ &= \frac{A_r \eta_0 \Delta l^2 |I_0|^2 k_0^2 F^4(\rho)}{128\pi^3 \rho^4} \sigma_1(\omega_d) \end{aligned} \tag{2.48}$$

from which it immediately follows that the first-order component of the monostatic HF radar cross section of the swell-contaminated seas can be written as

$$\sigma_1(\omega_d) = 16\pi k_0^2 \Delta\rho \sum_{m=\pm 1} \left[{}_S S_1(m\vec{K}) + {}_W S_1(m\vec{K}) \right] \frac{K^{2.5}}{\sqrt{g}} \mathrm{Sa}^2\left[\frac{\Delta\rho}{2}(K - 2k_0) \right] . \quad (2.49)$$

It should be noted that (2.49) has a unit of (radian/second)$^{-1}$ and accounts for a single scatter from first-order waves only.

Similarly, the second-order HF radar cross section for swell-contaminated seas will be given by

$$\begin{aligned} \sigma_2(\omega_d) = 8\pi k_0^2 \Delta\rho \sum_{m_1=\pm 1} \sum_{m_2=\pm 1} \int_0^{\infty} \int_{-\pi}^{\pi} \int_0^{\infty} \Big[|\Gamma_p|^2 \Big({}_S S_1(m_1\vec{K}_1) {}_S S_1(m_2\vec{K}_2) \\ + {}_W S_1(m_1\vec{K}_1) {}_W S_1(m_2\vec{K}_2) \Big) + 2|{}_E\Gamma_p|^2 \Big({}_S S_1(m_1\vec{K}_1) {}_W S_1(m_2\vec{K}_2) \Big) \Big] \\ \cdot \delta(\omega_d + m_1\sqrt{gK_1} + m_2\sqrt{gK_2}) K_T^2 K_1 \mathrm{Sa}^2\left[\frac{\Delta\rho}{2}(K_T - 2k_0) \right] dK_1 \, d\theta_{\vec{K}_1} \, dK_T \quad . \end{aligned} \quad (2.50)$$

To conclude this section, a few important assumptions shall be restated: 1) for both swell and wind waves, the sea surface can be viewed as a homogeneous and stationary zero-mean Gaussian process; 2) the swell and wind wave components are decoupled and independent from each other, so that the total Fourier coefficient of the ocean surface, ${}_T P_{\vec{K},\omega}$, contains only two linear portions.

2.3 Cross Sections Involving Coupling Effects

In the previous section, the HF radar cross sections were derived for mixed sea surface based on the assumption that no coupling effects exist between swell and wind waves. However, strong non-linear interaction between long-period waves such as swell and

shorter wind waves has been verified both through experiments [57] and field observations [58]. In recent attempts, a few researchers [59, 11] have numerically modeled the coupling process between swell and wind waves by following Hasselmann's classic work [51] on non-linear energy transfer for gravity waves. Despite the fact that their numerical models demonstrate weaker interaction effects than real measurements, the general process agrees quite well.

In this context, a new coupling term, ${}_{C}P_{\vec{K},\omega}$, indicating the non-linear coupling effects between swell and wind waves is added into the Fourier representation in (2.11), with the coupling coefficient denoted by ${}_{C}\Gamma_{p}$ (whose form is unclear for the moment). Now the total Fourier coefficient ${}_{T}P_{\vec{K},\omega}$ may be expanded as

$$\begin{aligned}
{}_{T}P_{\vec{K},\omega} &= {}_{C}P_{\vec{K},\omega} + {}_{S}P_{\vec{K},\omega} + {}_{W}P_{\vec{K},\omega} \\
&= \sum_{\substack{\vec{K}_1+\vec{K}_2=\vec{K} \\ \omega_1+\omega_2=\omega}} {}_{C}\Gamma_{pS1}P_{\vec{K}_1,\omega_1}{}_{W1}P_{\vec{K}_2,\omega_2} + \left({}_{S1}P_{\vec{K},\omega} + \sum_{\substack{\vec{K}_1+\vec{K}_2=\vec{K} \\ \omega_1+\omega_2=\omega}} {}_{H}\Gamma_{pS1}P_{\vec{K}_1,\omega_1}{}_{S1}P_{\vec{K}_2,\omega_2}\right) \\
&+ \left({}_{W1}P_{\vec{K},\omega} + \sum_{\substack{\vec{K}_1+\vec{K}_2=\vec{K} \\ \omega_1+\omega_2=\omega}} {}_{H}\Gamma_{pW1}P_{\vec{K}_1,\omega_1}{}_{W1}P_{\vec{K}_2,\omega_2}\right) \quad . \qquad (2.51)
\end{aligned}$$

Based on (2.51), we can easily form the first- and second-order E-field received from the ocean surface by following the same procedure as described in Section 2.2.1. It is then found that for this new "coupling case", the received first-order E-field, which arises from single scatters from first-order ocean waves only, has exactly the same expression as (2.15). Since the first-order electric fields in the two cases are identical with each other, we may skip the derivation process and directly write the final first-order cross section for the "coupling case" as

$$\sigma_1(\omega_d) = 16\pi k_0^2 \Delta\rho \sum_{m=\pm 1} \left[{}_{S}S_1(m\vec{K}) + {}_{W}S_1(m\vec{K})\right] \frac{K^{2.5}}{\sqrt{g}} \mathrm{Sa}^2\left[\frac{\Delta\rho}{2}(K-2k_0)\right] \qquad (2.52)$$

with the symbol definitions remaining the same as before.

While there is no change in the first-order result, the second-order E-field in the "coupling case" will be slightly modified. By substituting (2.51) back into (2.3), we observe that the hydrodynamic second-order E-field is given by

$$
\begin{aligned}
{}_H(E_n)_2(t) = & -j\eta_0 \Delta l \Delta\rho I_0 k_0^2 \frac{F^2(\rho)}{(2\pi\rho)^{3/2}} e^{-j\frac{\pi}{4}} e^{jk_0\Delta\rho} \\
& \cdot \sum_{\vec{K}_1,\omega_1} \sum_{\vec{K}_2,\omega_2} \left[{}_H\Gamma_p \Big({}_{S1}P_{\vec{K}_1,\omega_1 S1}P_{\vec{K}_2,\omega_2} + {}_{W1}P_{\vec{K}_1,\omega_1 W1}P_{\vec{K}_2,\omega_2} \Big) + {}_C\Gamma_{pS1}P_{\vec{K}_1,\omega_1 W1}P_{\vec{K}_2,\omega_2} \right] \\
& \cdot \sqrt{K_T} e^{j(\omega_1+\omega_2)t} e^{j\rho K_T} \mathrm{Sa}\left[\frac{\Delta\rho}{2}(K_T - 2k_0) \right] \quad . \qquad (2.53)
\end{aligned}
$$

Similarly, the electromagnetic second-order E-field can be obtained by substituting (2.51) into (2.4) and neglecting the higher-order effects, which is seen to take the same form as (2.19), i.e.,

$$
\begin{aligned}
{}_E(E_n)_2(t) = & -j\eta_0 \Delta l \Delta\rho I_0 k_0^2 \frac{F^2(\rho)}{(2\pi\rho)^{3/2}} e^{-j\frac{\pi}{4}} e^{jk_0\Delta\rho} \sum_{\vec{K}_1,\omega_1} \sum_{\vec{K}_2,\omega_2} {}_E\Gamma_p \\
& \cdot \Big({}_{S1}P_{\vec{K}_1,\omega_1 S1}P_{\vec{K}_2,\omega_2} + 2\,{}_{S1}P_{\vec{K}_1,\omega_1 W1}P_{\vec{K}_2,\omega_2} + {}_{W1}P_{\vec{K}_1,\omega_1 W1}P_{\vec{K}_2,\omega_2} \Big) \\
& \cdot \sqrt{K_T} e^{j(\omega_1+\omega_2)t} e^{j\rho K_T} \mathrm{Sa}\left[\frac{\Delta\rho}{2}(K_T - 2k_0) \right] \quad . \qquad (2.54)
\end{aligned}
$$

Thus, the total second-order E-field can be promptly obtained by combining the two portions as

$$
\begin{aligned}
(E_n)_2(t) = & \; {}_H(E_n)_2(t) + {}_E(E_n)_2(t) \\
= & -j\eta_0 \Delta l \Delta\rho I_0 k_0^2 \frac{F^2(\rho)}{(2\pi\rho)^{3/2}} e^{-j\frac{\pi}{4}} e^{jk_0\Delta\rho} \sum_{\vec{K}_1,\omega_1} \sum_{\vec{K}_2,\omega_2} \Big[\Big({}_C\Gamma_p + 2\,{}_E\Gamma_p \Big) {}_{S1}P_{\vec{K}_1,\omega_1 W1}P_{\vec{K}_2,\omega_2} \\
& + \Gamma_p \Big({}_{S1}P_{\vec{K}_1,\omega_1 S1}P_{\vec{K}_2,\omega_2} + {}_{W1}P_{\vec{K}_1,\omega_1 W1}P_{\vec{K}_2,\omega_2} \Big) \Big] \\
& \cdot \sqrt{K_T} e^{j(\omega_1+\omega_2)t} e^{j\rho K_T} \mathrm{Sa}\left[\frac{\Delta\rho}{2}(K_T - 2k_0) \right] \qquad (2.55)
\end{aligned}
$$

where as usual, $\Gamma_p = {}_E\Gamma_p + {}_H\Gamma_p$.

Next, we shall seek the autocorrelation of (2.55). By referring to Appendix A.2 for the ensemble averages that equal to zero, we may express the remainder of the autocorrelation as

$$\begin{aligned}
&\mathcal{R}_2(\tau) = \frac{A_r}{2\eta_0} < (E_n)_2(t+\tau)(E_n)_2^*(t) > \\
&= \frac{A_r\eta_0\Delta l^2\Delta\rho^2|I_0|^2k_0^4}{2}\frac{F^4(\rho)}{(2\pi\rho)^3} \\
&\Bigg\{ \sum_{\vec{K}_1,\omega_1}\sum_{\vec{K}_2,\omega_2}\sum_{\vec{K}_1',\omega_1'}\sum_{\vec{K}_2',\omega_2'} \Bigg[\Big|{}_C\Gamma_p + 2{}_E\Gamma_p\Big|^2 \Big\langle {}_{S1}P_{\vec{K}_1,\omega_1 W1}P_{\vec{K}_2,\omega_2 S1}P^*_{\vec{K}_1',\omega_1' W1}P^*_{\vec{K}_2',\omega_2'}\Big\rangle \\
&+ \Big|\Gamma_p\Big|^2\Big(\Big\langle {}_{S1}P_{\vec{K}_1,\omega_1 S1}P_{\vec{K}_2,\omega_2 S1}P^*_{\vec{K}_1',\omega_1' S1}P^*_{\vec{K}_2',\omega_2'}\Big\rangle + \Big\langle {}_{W1}P_{\vec{K}_1,\omega_1 W1}P_{\vec{K}_2,\omega_2 W1}P^*_{\vec{K}_1',\omega_1' W1}P^*_{\vec{K}_2',\omega_2'}\Big\rangle\Big)\Bigg] \\
&\cdot \sqrt{K_T}\sqrt{K_T'}e^{j(\omega_1+\omega_2)(t+\tau)}e^{-j(\omega_1'+\omega_2')t}e^{j\rho K_T}e^{-j\rho K_T'} \\
&\cdot \mathrm{Sa}\Big[\frac{\Delta\rho}{2}(K_T - 2k_0)\Big]\mathrm{Sa}\Big[\frac{\Delta\rho}{2}(K_T' - 2k_0)\Big]\Bigg\} \quad . \qquad (2.56)
\end{aligned}$$

Again, employing the results in (A.23) and (A.27), we can reduce (2.56) into a differential form as

$$\begin{aligned}
&\mathcal{R}_2(\tau) = \frac{A_r\eta_0\Delta l^2\Delta\rho^2|I_0|^2k_0^4}{4}\frac{F^4(\rho)}{(2\pi\rho)^3} \\
&\sum_{m_1=\pm1}\sum_{m_2=\pm1}\int_{-\infty}^{\infty}\int_{-\pi}^{\pi}\int_{0}^{\infty}\int_{-\infty}^{\infty}\int_{-\pi}^{\pi}\int_{0}^{\infty}\Bigg\{\Bigg[\Big|\Gamma_p\Big|^2\Big({}_SS_1(m_1\vec{K}_1){}_SS_1(m_2\vec{K}_2) + {}_WS_1(m_1\vec{K}_1){}_WS_1(m_2\vec{K}_2)\Big)\Bigg] \\
&+ \Bigg[\frac{1}{2}\Big|{}_C\Gamma_p + 2{}_E\Gamma_p\Big|^2\Big({}_SS_1(m_1\vec{K}_1){}_WS_1(m_2\vec{K}_2)\Big)\Bigg]\Bigg\}\delta(\omega_1 + m_1\sqrt{gK_1})\delta(\omega_2 + m_2\sqrt{gK_2}) \\
&\cdot K_T e^{j(\omega_1+\omega_2)\tau}\mathrm{Sa}^2\Big[\frac{\Delta\rho}{2}(K_T - 2k_0)\Big]K_1\,dK_1\,d\theta_{\vec{K}_1}\,d\omega_1 K_2\,dK_2\,d\theta_{\vec{K}_2}\,d\omega_2 \quad . \qquad (2.57)
\end{aligned}$$

By converting the $d\vec{K}_2$ integral into a $d\vec{K}_T$ integral and eliminating the integrals of

$d\omega_1$ and $d\omega_2$ in accordance with the delta constraints, we have

$$\mathcal{R}_2(\tau) = \frac{A_r \eta_0 \Delta l^2 \Delta\rho^2 |I_0|^2 k_0^4}{4} \frac{F^4(\rho)}{(2\pi\rho)^3}$$
$$\sum_{m_1=\pm1} \sum_{m_2=\pm1} \int_{-\pi}^{\pi} \int_{0}^{\infty} \int_{-\pi}^{\pi} \int_{0}^{\infty} \left\{ \left[\left| \Gamma_p \right|^2 \left({}_S S_1(m_1 \vec{K}_1) {}_S S_1(m_2 \vec{K}_2) + {}_W S_1(m_1 \vec{K}_1) {}_W S_1(m_2 \vec{K}_2) \right) \right] \right.$$
$$\left. + \left[\frac{1}{2} \left| {}_C\Gamma_p + 2 {}_E\Gamma_p \right|^2 \left({}_S S_1(m_1 \vec{K}_1) {}_W S_1(m_2 \vec{K}_2) \right) \right] \right\}$$
$$\cdot K_T^2 K_1 e^{j(\omega_1+\omega_2)\tau} \mathrm{Sa}^2 \left[\frac{\Delta\rho}{2} (K_T - 2k_0) \right] dK_1 d\theta_{\vec{K}_1} dK_T d\theta_{\vec{K}_T} \quad . \tag{2.58}$$

Finally, following the same process presented in the previous section (A Fourier transform and a normalization by the patch area), we obtain the second-order cross section involving coupling effects between swell and wind waves as

$$\sigma_2(\omega_d) = 8\pi k_0^2 \Delta\rho \sum_{m_1=\pm1} \sum_{m_2=\pm1} \int_{0}^{\infty} \int_{-\pi}^{\pi} \int_{0}^{\infty} \left\{ \left[\left| \Gamma_p \right|^2 \left({}_S S_1(m_1 \vec{K}_1) {}_S S_1(m_2 \vec{K}_2) \right. \right. \right.$$
$$\left. \left. \left. + {}_W S_1(m_1 \vec{K}_1) {}_W S_1(m_2 \vec{K}_2) \right) \right] + \left[\frac{1}{2} \left| {}_C\Gamma_p + 2 {}_E\Gamma_p \right|^2 \left({}_S S_1(m_1 \vec{K}_1) {}_W S_1(m_2 \vec{K}_2) \right) \right] \right\}$$
$$\cdot \delta(\omega_d + m_1 \sqrt{g K_1} + m_2 \sqrt{g K_2}) K_T^2 K_1 \mathrm{Sa}^2 \left[\frac{\Delta\rho}{2} (K_T - 2k_0) \right] dK_1 d\theta_{\vec{K}_1} dK_T \quad . \tag{2.59}$$

Although the difference between (2.59) and (2.50) is self-evident, a solid conclusion may not be drawn at this point as to which one of the two results is more valid before calculating the cross sections and comparing them with real Doppler radar spectra. In the next section, we will validate our derived cross section models against the data collected in field tests, and various features of both the "no coupling" and "coupling" models will be presented and discussed.

2.4 Calculation and Interpretation of the Cross Sections

2.4.1 Choice of Spectral Model for Swell Contaminated Seas

Any description of the scattering of radar signals from the ocean surface obviously must incorporate a particular ocean model. Typically, this model is specified by a directional wave number spectrum, $S_1(\vec{K})$, with the direction of the wave vectors, $\vec{K}$, being $\theta_{\vec{K}}$ (i.e. $\vec{K} \equiv (K, \theta_{\vec{K}})$). Specifically, it is assumed that this wave spectrum can be expressed as the product of a non-directional spectrum, $S_1(K)$, and a normalized directional distribution, $D(\theta_{\vec{K}})$ [60]. That is,

$$S_1(\vec{K}) = S_1(K) \cdot D(\theta_{\vec{K}}) \quad . \tag{2.60}$$

In our case, the two distinct directional spectra appearing in (2.59) shall be defined as

$${}_S S_1(\vec{K}_1) = {}_S S_1(K) \cdot {}_S D(\theta_{\vec{K}}) \quad \text{and} \quad {}_W S_1(\vec{K}_1) = {}_W S_1(K) \cdot {}_W D(\theta_{\vec{K}}) \tag{2.61}$$

where ${}_S S(K)$ and ${}_W S(K)$ represent the non-directional portion for swell and wind waves, respectively, while $D_s(\theta_{\vec{K}})$ and $D_w(\theta_{\vec{K}})$ denote their respective directional distribution. The exact expressions for (2.61) will be given in what follows.

2.4.1.1 The Swell Component

During the last two decades, several distinct non-directional models have been constructed to represent swell. By examining a 40-day long wave record at Cape Grim, Australia, Hinwood *et al.* [61] suggested that the swell component can be well de-

scribed by a Wallop spectrum. Similarly, Torsethaugen [62] tracked buoy data collected in North Sea for a month and modelled the swell part as a narrow bandwidth Jonswap spectrum. Although these two spectra are similar in the overall shape, the Wallop spectrum is more appropriate in our case because its short decaying tail better matches the property of swell generated at great distances. The non-directional portion of the swell is thus expressed by

$$_{S}S_1(K) = A * G_o * \frac{g^2}{2\omega^3} * (\frac{\omega}{\omega_p})^{-N} * \exp\frac{-N}{4(\frac{\omega}{\omega_p})^4} \tag{2.62}$$

where G_o and A denote two normalization factors, ω_p implies the peak angular frequency and N gives the shape factor that determines the spectral spreading [63]. Note that K and ω are related via the deep water dispersion relationship throughout this thesis as

$$\omega = \sqrt{gK} \quad . \tag{2.63}$$

As will be further introduced in Chapter 4, the typical period for swell components is within the range of 10-18 seconds, while the corresponding significant wave height has a maximum of 4 metres [50].

Historically, just as several forms of $S_1(K)$ have evolved, so has a variety of directional models, $D(\theta_{\vec{K}})$. Yet, little information can be found regarding the exact directional distribution for the swell component. For simplicity, we employ the traditional cardioid directional distribution ($\cos^{2s}$) with $s = 30$ to illustrate its convergent property as

$$_{S}D(\theta_{\vec{K}}) = \frac{\Gamma(s+1)}{2\sqrt{\pi}(s+1/2)} \cos^{2s}\left(\frac{\theta_{\vec{K}} - \theta_s}{2}\right) \quad . \tag{2.64}$$

In (2.64), θ_s denotes the dominant swell propagation direction and $\Gamma(\cdot)$ is the usual gamma function.

2.4.1.2 The Wind-sea Component

As in [29], here a Pierson-Moskowitz spectrum is adopted to represent the fully developed wind driven sea. As a result, the non-directional portion, ${}_{W}S(K)$, with a slight modification, can be given by

$$ {}_{W}S_1(K) = \frac{1}{2}S_{PM}(K) = \frac{\alpha_{PM}}{4K^4}e^{\left(\frac{-0.74g^2}{K^2U^4}\right)} \tag{2.65} $$

where α_{PM} is a non-dimensional constant equal to 0.0081 and U represents the wind speed measured at 19.5 m above the ocean surface. It can be seen that U is the sole variable describing the spectrum and there is clearly no fetch or duration dependence.

In terms of the directional portion ${}_{W}D(\theta_{\vec{K}})$ for wind seas, the $\cos^{2s}$ spreading is again applied, but now with a value of $s = 2$ to indicate the normal broad spreading of wind waves.

Generally, the wave model introduced in this section for swell-contaminated seas is used as necessary throughout the cross section simulation and the inversion process. A comparison between this wave spectrum model and real data presented by Wyatt [3] is shown in Fig. 2.2 and 2.3. The narrow-band swell component with a centre frequency at 0.85 Hz and a mean direction of 210° is evident in both figures, while the broad-band wind wave portion is more irregular in the real wave data.

2.4.2 The First-order Cross Section Analysis

The first-order cross section of swell-contaminated seas, denoted by (2.52), may be calculated by following the procedure described in [5]. Fig. 2.5 and Fig. 2.6 illustrate the smoothed first-order cross sections when the operating radar frequency is 15 and 5 MHz, respectively, and the corresponding scattering geometry is shown in Fig. 2.4.

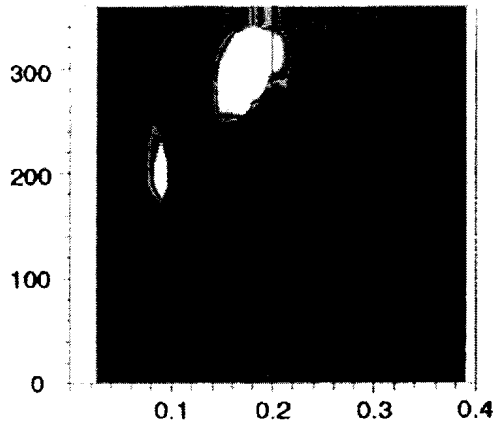

Figure 2.2: Directional spectrum estimated from the directional waverider measurement, showing both swell and locally wind-generated waves. (Figure taken from [3])

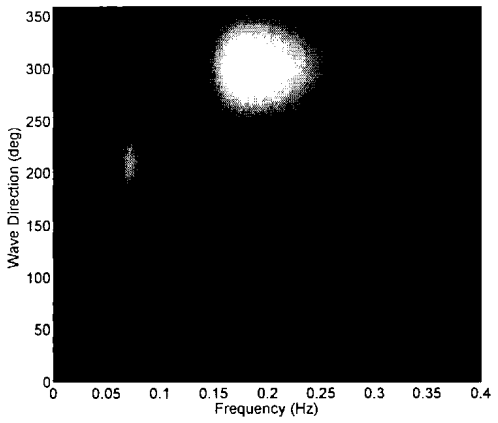

Figure 2.3: Simulated wave spectrum combining a Wallop spectrum and a PM spectrum.

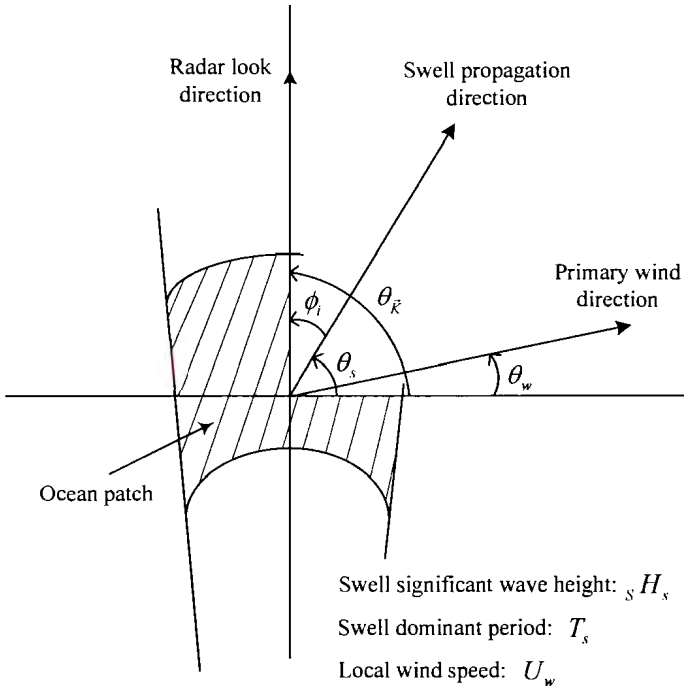

Figure 2.4: The general geometry of patch scatters on swell-contaminated seas.

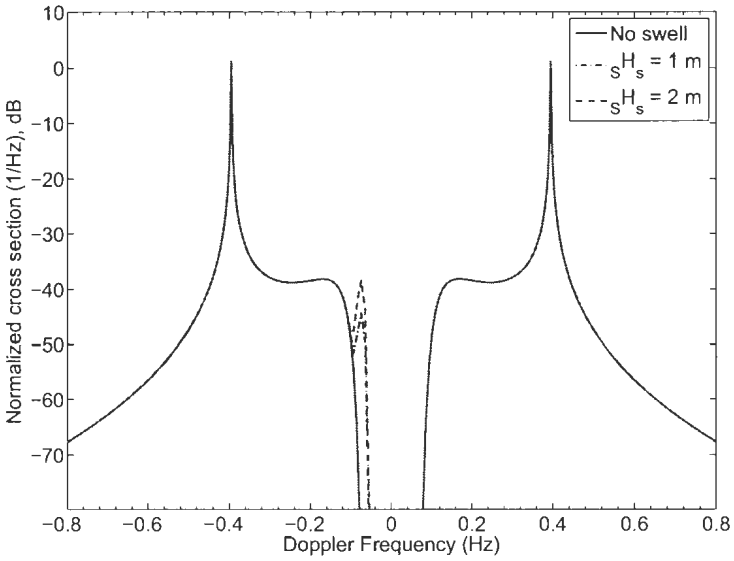

Figure 2.5: An example of the first-order radar cross sections when the operating frequency $f_0 = 15$ MHz. The radar look direction, $\theta_{\vec{K}}$, is 90 degrees, the local wind direction is 180 degrees, and the swell propagation direction is 60 degrees.

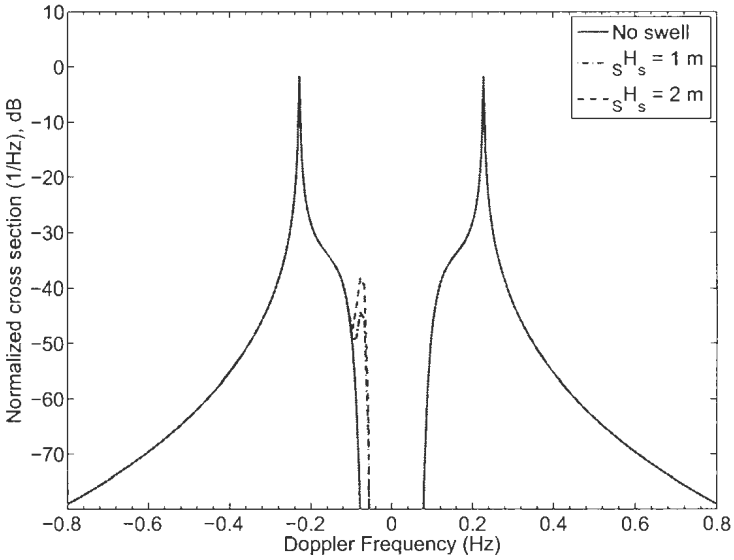

Figure 2.6: First-order cross sections with $f_0 = 5$ MHz. The other input parameters are identical with those in Fig. 2.5.

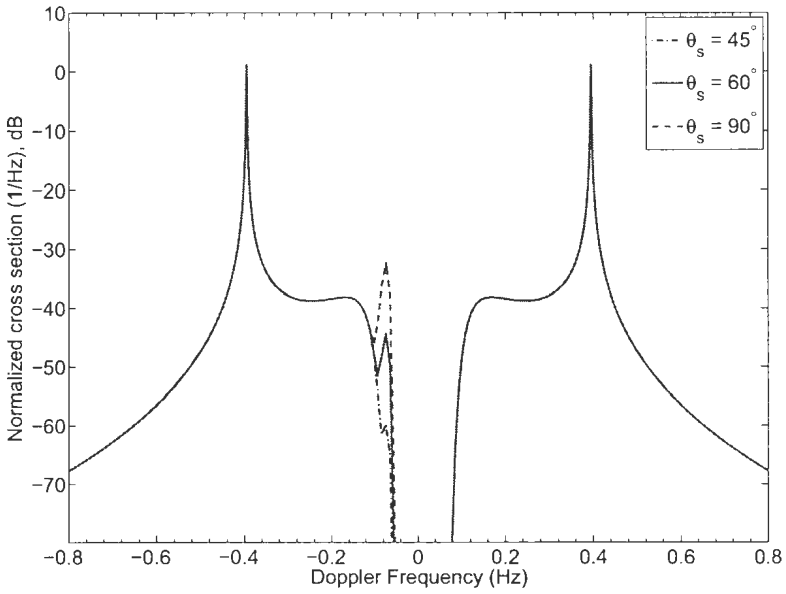

Figure 2.7: First-order cross sections with different ϕ_i. The significant wave height of the swell component is fixed to 1.5 metres.

Clearly, the overall shape and major peak positions of the Doppler spectrum remain unchanged compared to that of wind driven seas only. This may be explained by the fact that the two prominent Bragg peaks result from the interaction between the radar signal and short wind waves, rather than the long-period waves such as swell; therefore, the introduction of the swell component will not cause significant change in the Bragg region. However, it may be also noticed that when the intersection angle between the swell direction and the radar look direction $\phi_i = |\theta_{\vec{K}} - \theta_s| \leq 20°$ (see Fig. 2.7), a visible peak at near-zero Doppler appears due to the presence of the swell component. Predictably, the amplitude of this first-order swell peak largely depends on the swell height and the intersection angle ϕ_i that determines the projected swell velocity along the radar look direction. For example, if the swell propagation direction is aligned with the radar look direction, the first-order scattering from long waves will be the strongest. On the other hand, if the swell direction is perpendicular to the look

direction, the first-order scattering from the swell is simply negligible. In other words, to get an enhanced first-order swell peak, one should expect ϕ_i to approach zero, and the swell height to be reasonably large, and the local sea state to be low. Obviously, such prerequisites are seldom satisfied simultaneously in the real world. Thus, the first-order swell peak is often obscured either by noise or by the surrounding second-order Doppler continuum, which makes it unlikely to be seen in real data. Moreover, since the first-order cross section equations are identical in both the "coupling case" and the "non-coupling case", it is impossible to determine which case is more valid by solely depicting the first-order results.

2.4.3 The Second-order Cross Section Analysis

A cross section comparison between the "coupling case" and the "non-coupling case" is shown in Fig. 2.8. Since the exact equation for the coupling coefficient, ${}_C\Gamma_p$, is still unknown, for the purpose of this work, we assume it to take the same form as ${}_H\Gamma_p$ during the simulation. It is apparent that the solid curve, which indicates the cross sections with coupling effects involved, agrees well with the field data collected in [23, 4] (e.g., see Fig. 2.9), as four second-order swell peaks are clearly visible surrounding the first-order Bragg region. On the contrary, the dashed curve depicting the non-coupling case has no swell peak structures and does not match with field observations.

Another important observation is that the hydrodynamic contribution to the second order is generally dominant, especially in the Doppler region where the swell peaks and the Bragg peaks are located (see Fig. 2.10). Since these peaks contain sufficient information for subsequent extraction, we may safely neglect the electromagnetic coupling effects when developing the inversion algorithm for swell.

In brief, a form of non-linear interaction must exist between the incoming swell

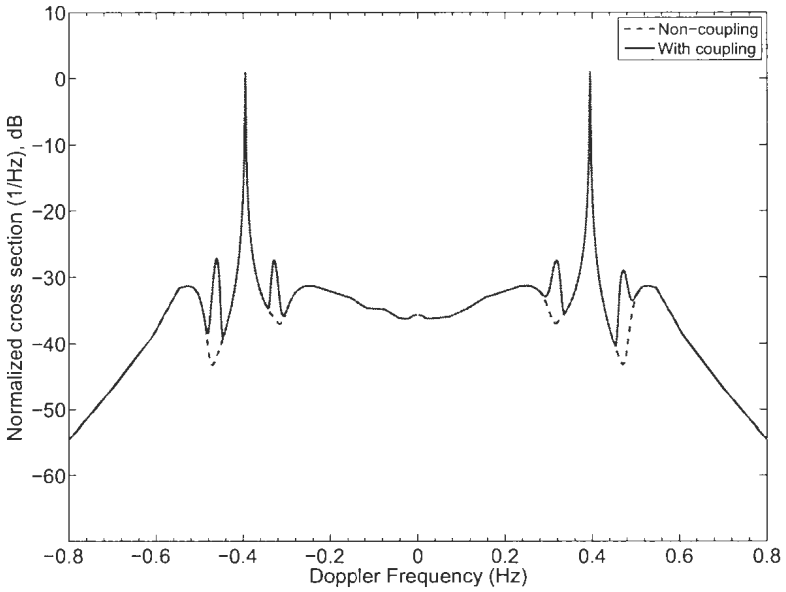

Figure 2.8: Second-order cross sections with $f_0 = 15$ MHz. Four second-order swell peaks are clearly visible in the result under the coupling assumption.

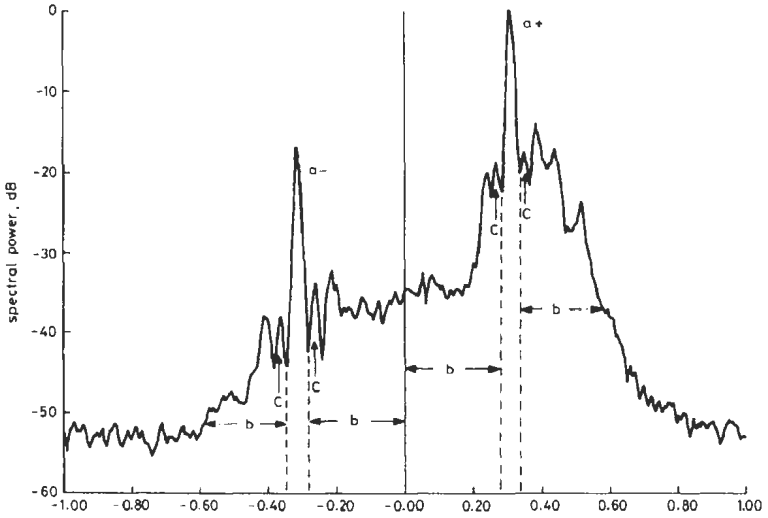

Figure 2.9: Doppler spectrum measured along a south-westerly beam from South Wales, taken from [4]. $a\pm$, approaching and receding first-order returns, indicating an onshore wind. b, second-order continuum showing long waves predominately towards the radar. c, very long wavelength swell peaks again propagating towards the radar.

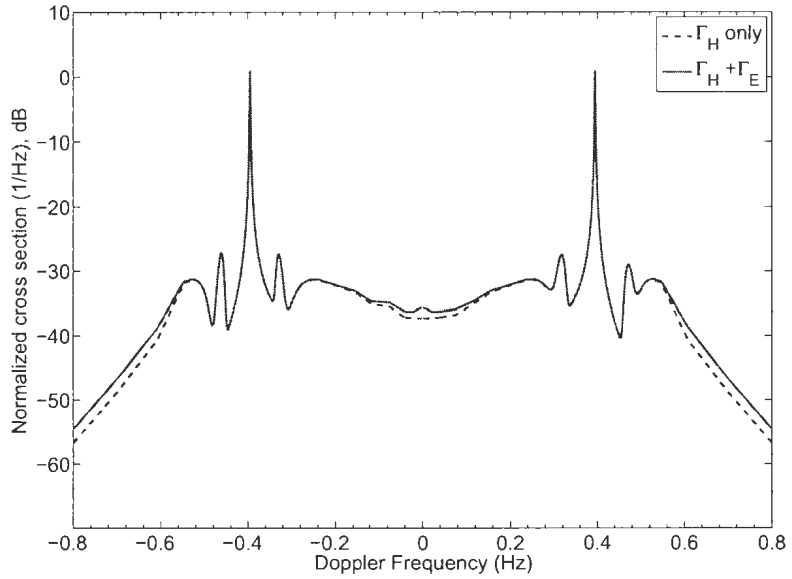

Figure 2.10: Second-order cross sections with $f_0 = 15$ MHz. The dashed curve is obtained by considering the hydrodynamic coupling effects only, while the solid curve accounts for the combined electromagnetic and hydrodynamic effects.

and local wind waves, and the coupling effects can be well explained by Hasselman's classic energy transfer theory for gravity waves [51]. Thus, (2.59), rather than (2.50), will be referred to hereafter as the proper form for the second-order cross section. Various features of the model will be presented in the following analysis.

2.4.3.1 The Effects of the Radar Operating Frequency

Fig. 2.11 shows the cross sections for three different operating frequencies of 10 MHz, 15 MHz, and 25 MHz. It is apparent that the first-order Bragg peaks, while shifted in Doppler, are of comparable magnitudes. Again, this is explained by the fact that the ocean waves producing these peaks are basically short waves, which are located in the saturated region of the wave height spectrum.

It is noteworthy that the swell peaks are generally more prominent at higher frequencies, which suggests that the swell information may be better extracted when the

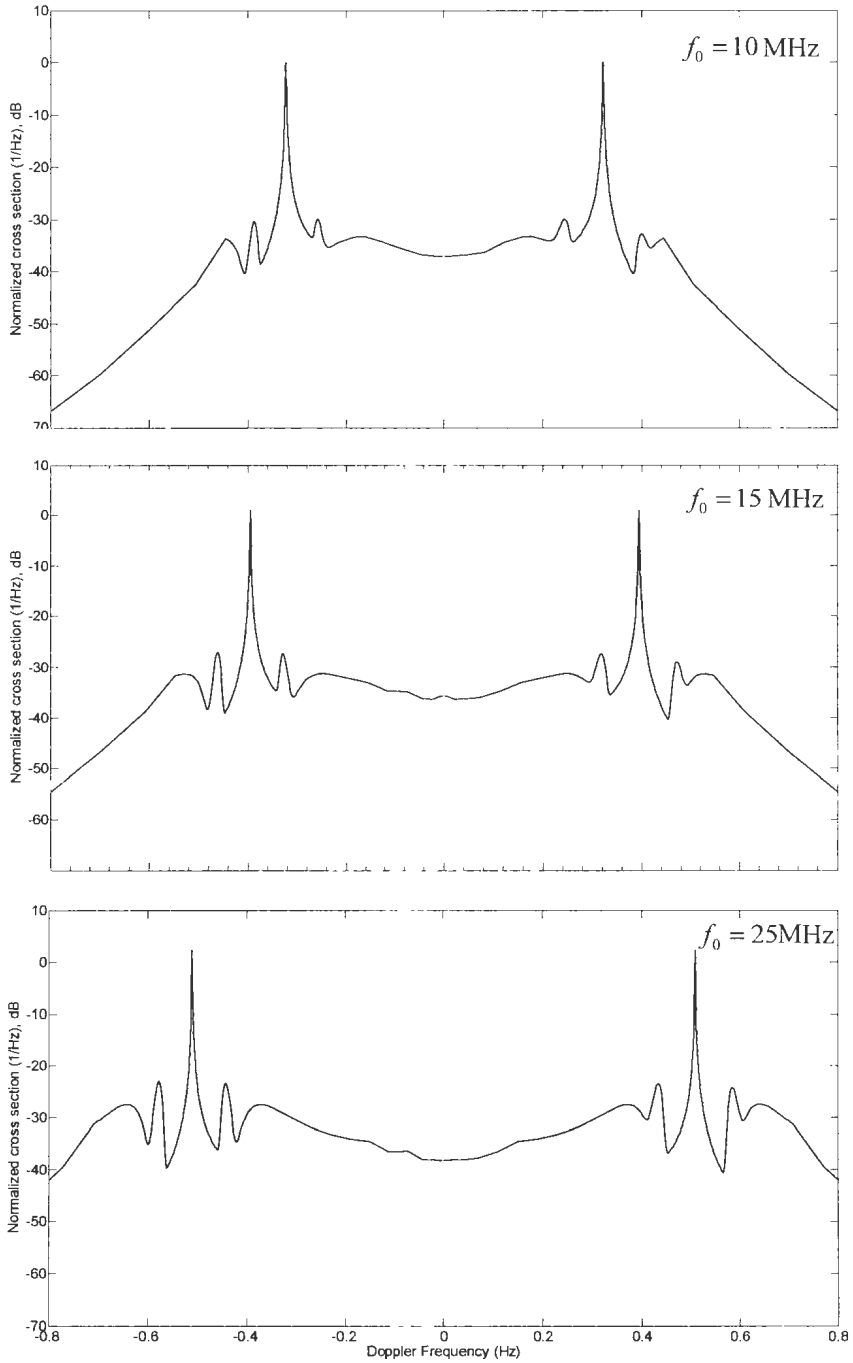

Figure 2.11: The effect on the cross sections of changing the operating frequency, f_0. The wind direction is 180°, the radar look direction is 90°, the wind speed is 10 m/s, the swell wave height is 1.5 m, the swell period is 14 seconds, and the swell direction is 60°.

radar is operating in the upper HF band (15-30 MHz). However, since the change in the operating frequency does not significantly affect the radar cross sections in the swell peak region, a fixed value of 15 MHz is chosen hereafter.

2.4.3.2 The Effects of the Swell Significant Wave Height

As can be expected, the amplitudes of the swell peaks will largely depend on the significant wave height of the swell component. Fig. 2.12 demonstrates this effect by setting the swell height to 0.5, 1, and 2 metres, respectively.

An initial observation from Fig. 2.12 is that the strength of the Doppler spectrum, aside from the swell peak region, is almost identical for the three cases shown. Still, it is worth noticing that a small increase in amplitudes occurs at the near-zero Doppler, which corresponds to the increase of first-order swell peaks due to larger ${}_{S}H_{s}$ (see Fig. 2.5). Such differences can be simply viewed as trivial in real practice, where the spectrum is quite rough and noise-contaminated.

A close examination reveals that the amplitudes of the swell peaks are almost proportional to the square of ${}_{S}H_{s}$, which agrees with [23], where it is stated that the normalized power of the swell peaks can be given by

$$R_{m,m'} = 2{}_{S}H_{s}^{2}|\Gamma_{m,m'}|^{2} \tag{2.66}$$

where $\Gamma_{m,m'}$ is a constant coupling coefficient that includes both hydrodynamic and electromagnetic effects.

Moreover, it is seen that the swell peaks are barely visible when ${}_{S}H_{s} = 0.5$ m, which indicates that the inversion of swell information is impossible beyond a certain threshold for the swell height (e.g., 0.5 m).

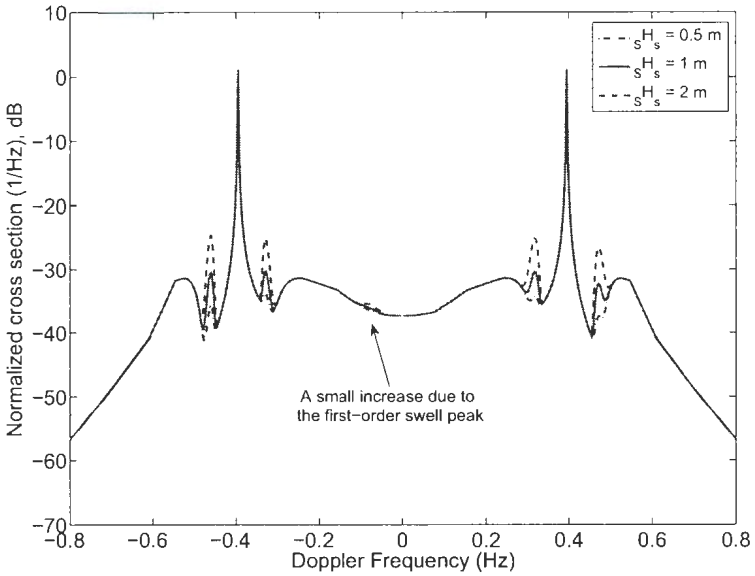

Figure 2.12: The effect on the cross sections of changing the swell significant wave height, $_SH_s$. The remaining parameters are identical to those in the middle figure of Fig. 2.11.

2.4.3.3 The Effects of the Swell Propagating Direction

Fig. 2.13 portrays how the swell propagating direction, θ_s, influences the cross section. While the Doppler positions of the swell peaks do not vary significantly for the three values of the intersection angle ϕ_i, the amplitudes drop quickly as ϕ_i increases. This result agrees with [49], in which it is suggested from field observation that the swell peak amplitude "reaches a maximum when the radar beam is in line with the direction of swell propagation and is a minimum when the beam is orthogonal to the direction of swell-wave propagation". Meanwhile, the slight difference between the peak positions can be explained by the fact that the frequency contours defined by the delta function constraint are not perfect circles [64]. Finally, the small increase at near-zero Doppler due to the first-order swell peaks may be again observed when changing the value of ϕ_s.

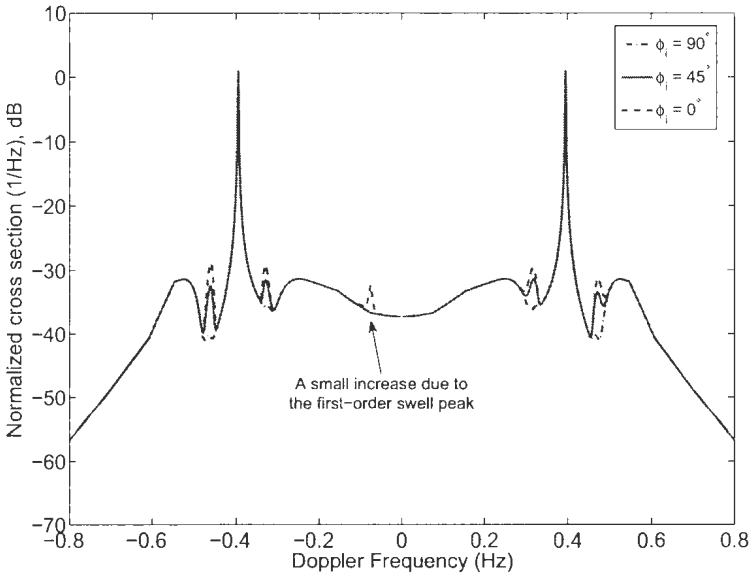

Figure 2.13: The effect on the cross sections of changing the swell propagating direction, θ_s. The intersection angle, ϕ_i in the figure can be given by $\phi_i = |\theta_{\vec{K}} - \theta_s|$. The remaining parameters are identical to those in Fig. 2.11.

2.4.3.4 The Effects of the Swell Dominant Period

Next, the effects of changing the swell peak frequency, f_s, or, the dominant period, T_s, are depicted in Fig. 2.14. Unlike the observation made from changing swell directions, the swell peaks now have almost the same heights but completely different positions. This is mainly due to the change in the size of the wave vector, $\vec{K}$, that is responsible for the maximum scatter. Thus, in order to extract the peak frequency of the swell component, the positions of the swell peaks must be first identified. This also coincides with the inversion algorithm proposed in [23]. A more detailed discussion regarding the relation between the theoretical swell peak positions and swell periods can be found in Appendix C.

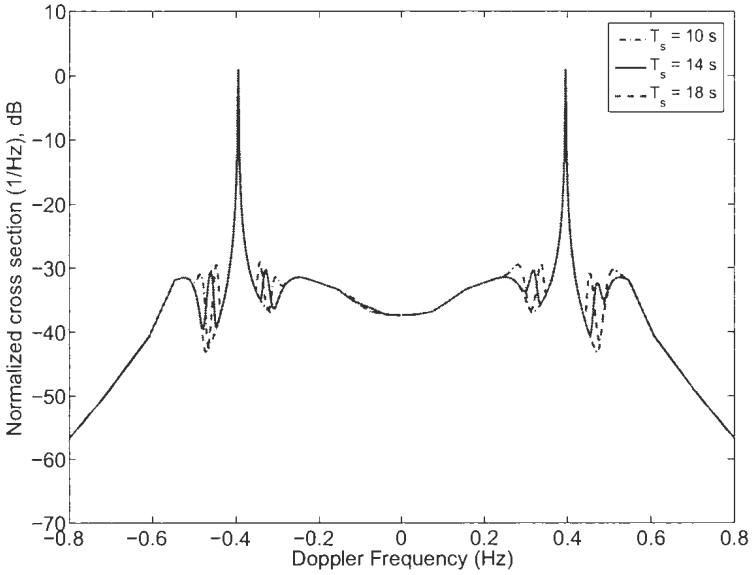

Figure 2.14: The effect on the cross sections of changing the swell dominant period, T_s. The remaining parameters are identical to those in Fig. 2.11.

2.4.3.5 The Effects of the Local Wind Speed

As was discussed in [5], the most obvious spectral effects, when changing the local wind speed, occurs adjacent to the Bragg peaks. Basically, at higher wind speeds, the relatively longer wind waves that produce the scatter carry a significant amount of the spectral energy so that the wind wave second-order structure has much higher peaks. However, since the swell peaks are not created by these long wind waves but rather by a particular swell wave component (whose frequency and power are already fixed) and a very short wind wave (which is located in the saturated region of the wave height spectrum), the amplitudes for swell peaks will remain almost constant as wind speed changes. In other words, when the local sea state is low, we are more likely to observe four clean swell peaks without the interference from the surrounding wind wave structures (e.g., the red dashed curve in Fig. 2.15); otherwise, the swell peaks can be completely buried.

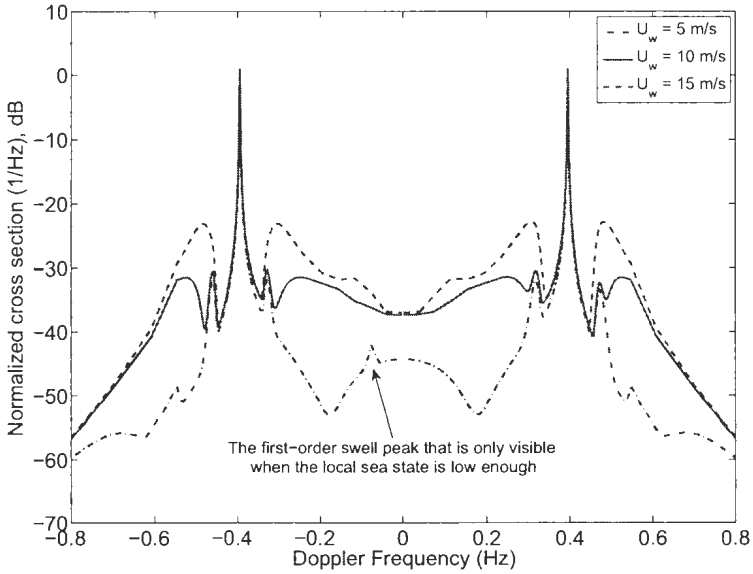

Figure 2.15: The effect on the cross sections of changing the local wind speed, U_w. The remaining parameters are identical to those in Fig. 2.11. In the case where $U_w = 15$ m/s, the swell peaks are no longer visible.

2.4.3.6 The Effects of the Local Wind Direction

Fig. 2.16 illustrates how the local wind direction influences the cross section. As in [5], when the wind direction is within 90 degrees of the radar look direction, the spectral energy is primarily distributed in the negative Doppler region. On the contrary, when the wind is blowing opposite to radar look direction, the positive Doppler section will be greatly enhanced. The implication is quite obvious: when the positive and negative Doppler region is imbalanced, there is a greater possibility that the two swell peaks on the one side are obscured by external noise (see the third figure in Fig. 2.16). In Chapter 4, it is stated that the extraction of swell information is most robust when all four swell peaks are considered. Thus, the accuracy of the inversion process could be significantly affected by the local wind direction.

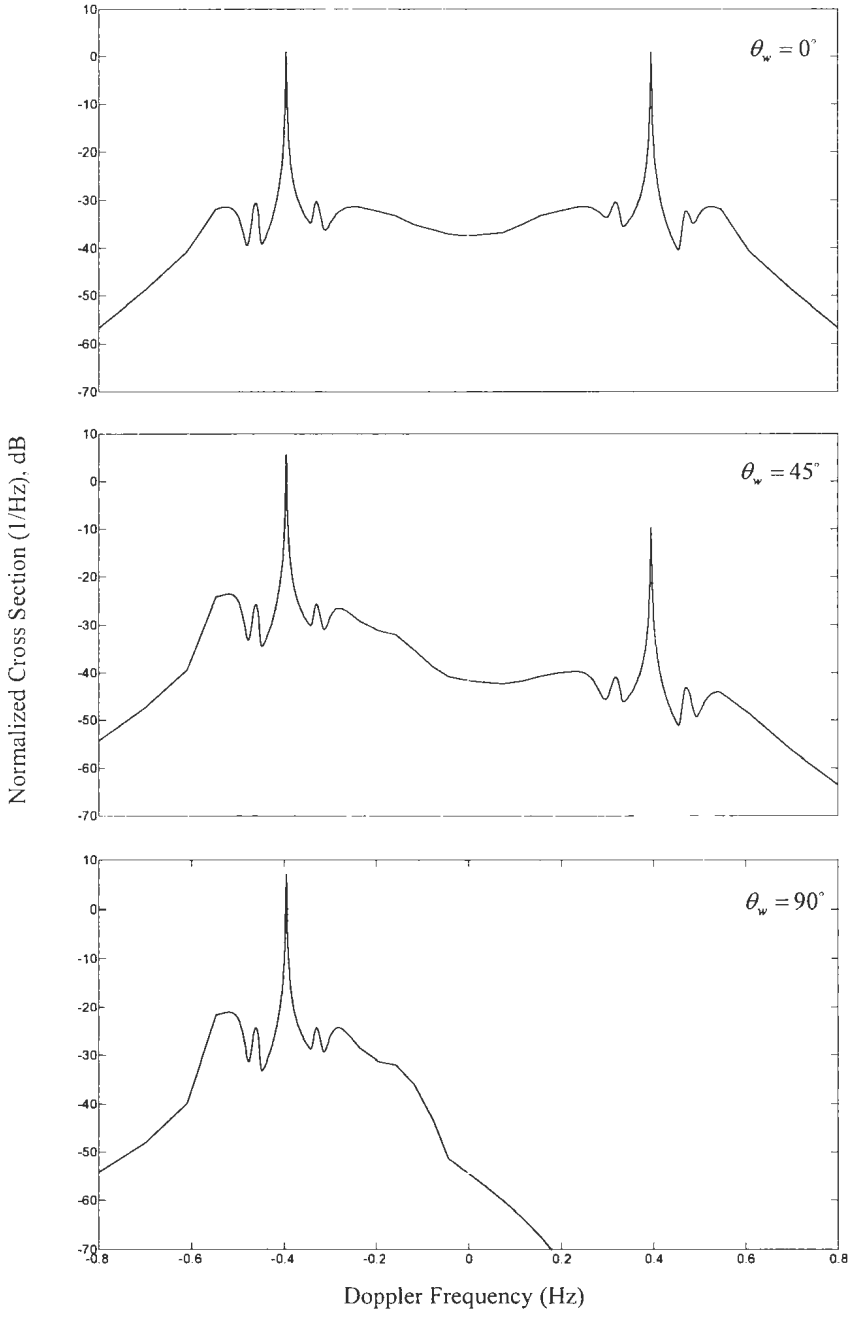

Figure 2.16: The effect on the cross sections of changing the local wind direction, θ_w. The remaining parameters are identical to those in Fig. 2.11. In the case where $\theta_w = 90°$ (aligns with the radar look direction), the swell peaks in the positive Doppler region totally vanish and may degrade the later inversion process.

2.5 General Chapter Summary

This chapter has been devoted to the derivation of the first- and second-order radar cross sections of swell-contaminated seas. Due to the similarity to the problem involving wind waves only, the equations for the received electric field scattered from a general ocean surface were first repeated, with the scattering surface represented by a three-dimensional Fourier series. The swell component was then incorporated via two different ways: 1) the incoming swell and local wind waves were assumed to be independent with no hydrodynamic interaction existing between the two, 2) a coupling portion, based on the classic analysis of Hasselmann [51], was added to the contribution from swell and wind waves. The received power spectral density and, subsequently, the radar cross sections per unit area for the two cases were developed to second order.

In order to validate the model, the proposed cross sections were calculated and depicted. It has been observed that the assumption which emphasizes the non-linear coupling effects between swell and wind waves, was more reasonable, as the corresponding Doppler spectrum displayed clear swell peak structures that highly resemble field data, while the first case above did not. Meanwhile, such a result provided a new perspective to prove the existence of the complicated coupling effects.

Finally, a variety of parameters affecting the cross sections were examined. These included operating frequency, swell height, direction and period, local wind speed and direction. It has been concluded that the swell direction and period can be inverted from the Doppler positions of the four swell peaks, and the swell height closely associates with the swell peak amplitudes. Also, the local sea state might significantly affect the inversion accuracy by obscuring the swell peaks.

In the next chapter, the cross section model is extended to include an FMCW waveform, instead of the pulsed waveform, as the excited source. Upon completing

the derivation, an inversion algorithm for swell parameters will be finally developed.

Chapter 3

The HF Radar Cross Sections of Swell-contaminated Seas for an FMCW Waveform

In this chapter, the cross section equations presented in Section 2.3 are extended to include a dipole source with a linear frequency-modulated continuous waveform (FMCW). Presently, most HF ground surveillance applications are based on the FMCW waveform due to its better resolution, less complexity, and lower peak power. Consequently, the development of an inversion algorithm to obtain ocean information from backscattered signals with an FMCW source rather than a pulsed source is quite important. To do so, a proper cross section model for the FMCW operation must be first established.

The fundamental analysis regarding the issue has already been extensively discussed in [30] and will not be repeated here. Generally, the equations of the first- and second-order cross sections for an FMCW waveform can be written analogously to (2.52) and (2.59). The results are then depicted and compared with those for the

pulse radar operation, and it is seen that the differences between the two modes are negligible in the present context.

3.1 The Derivation of the RCS for an FMCW Waveform

In [30], the mathematical equations for the electric fields collected after the first Fourier transform, or the so called "range transform", were neatly presented. Again, since the ocean surface defined in [30] was a general one, we may directly apply those field equations to the swell contamination case. Thus, the first-order E-field, including both single scatters and double scatters from first-order ocean waves, can be given by

$$(E_n)_1(\omega_r, t) = -j\eta_0 \Delta l \Delta\rho I_0 k_0^2 \frac{F^2(\rho)}{(2\pi\rho)^{3/2}} e^{-j\frac{\pi}{4}} \cdot \sum_{\vec{K},\omega} {}_T P_{\vec{K},\omega} \sqrt{K} e^{j\omega t} e^{j(K-2k_0+k_r)\rho} T_r \mathrm{Sm}(K, k_{BW}, \Delta_r) \tag{3.1}$$

where the new argument, ω_r, corresponds to a certain range cell at a distance of ρ via the relation that

$$\rho = \frac{c\omega_r}{4\pi\alpha} \tag{3.2}$$

where α is the sweep rate of the FMCW signal whose sweep bandwidth is B and sweep interval is T_r, i.e., $\alpha = B/T_r$. Moreover, the symbolic range resolution, $\Delta\rho$, is now associated with the sweep bandwidth through $\Delta\rho = c/2B$. Finally, k_r and k_B are defined by

$$k_r = \frac{\omega_r}{c} \quad \text{and} \quad k_{BW} = \frac{2\pi B}{c} \tag{3.3}$$

and the $\mathrm{Sm}(\cdot)$ function is defined as

$$\mathrm{Sm}(K, k_{BW}, \Delta_r) = \frac{1}{\pi}\Big\{\mathrm{Si}[(K - 2k_0 + k_{BW})\Delta_r] - \mathrm{Si}[(K - 2k_0 - k_{BW})\Delta_r]\Big\} \tag{3.4}$$

where the quantity Si refers to the sine integral

$$\mathrm{Si}(x) = \int_0^x \frac{\sin(t)}{t} dt \quad , \tag{3.5}$$

and $\pm\Delta_r$ represents the interaction between range bins and may take the value of

$$\Delta_r = \frac{\Delta\rho}{2}, \ \frac{2\Delta\rho}{2}, \ \frac{3\Delta\rho}{2}, \cdots . \tag{3.6}$$

In practice, such effects determine the actual range resolution and may be mitigated by windowing. Finally, the key term in (3.1) for the present analysis, the total Fourier coefficients of the swell-contaminated ocean surface, takes the same form as (2.51), which has been shown to be valid in the previous chapter.

Having clarified all parameters in (3.1), we can proceed to write the electromagnetic second-order E-field as

$$\begin{aligned} {}_E(E_n)_2(\omega_r, t) &= -j\eta_0 \Delta l \Delta\rho I_0 k_0^2 \frac{F^2(\rho)}{(2\pi\rho)^{3/2}} e^{-j\frac{\pi}{4}} \\ &\cdot \sum_{\vec{K}_1,\omega_1} \sum_{\vec{K}_2,\omega_2} {}_E\Gamma_{pT} P_{\vec{K}_1,\omega_1 T} P_{\vec{K}_2,\omega_2} \sqrt{K_T} e^{j\omega t} e^{j(K_T - 2k_0 + k_r)\rho} T_r \mathrm{Sm}(K_T, k_{BW}, \Delta_r) \end{aligned} \tag{3.7}$$

where $\vec{K}_T = \vec{K}_1 + \vec{K}_2$ still holds.

As in Section 2.3, the next step is to calculate the autocorrelations of the first- and second-order E-field given by (3.1) and (3.7). Obviously, the critical analysis on the ensemble averages, presented in Appendix A, is independent from the excitation source being used so that the parts associated with the wave height spectrum can

be written analogously to (2.52) and (2.59). However, the remaining terms must be modified according to [30]. Finally, the first-order cross section of swell-contaminated seas for FMCW radars is given by

$$\sigma_1(\omega_d) = 16\pi k_0^2 \Delta\rho \sum_{m=\pm 1} \left[{}_S S_1(m\vec{K}) + {}_W S_1(m\vec{K}) \right] \frac{K^{2.5}}{\sqrt{g}} \mathrm{Sm}^2(K, k_{BW}, \Delta_r) \quad , \tag{3.8}$$

and, similarly, the second-order cross section is

$$\begin{aligned} \sigma_2(\omega_d) = 8\pi k_0^2 \Delta\rho \sum_{m_1=\pm 1} \sum_{m_2=\pm 1} \int_0^{\infty} \int_{-\pi}^{\pi} \int_0^{\infty} \Bigg\{ \Bigg[\left|\Gamma_p\right|^2 \Big({}_S S_1(m_1\vec{K}_1) {}_S S_1(m_2\vec{K}_2) \\ + {}_W S_1(m_1\vec{K}_1) {}_W S_1(m_2\vec{K}_2) \Big) \Bigg] + \left[\frac{1}{2} \left| {}_C\Gamma_p + 2 {}_E\Gamma_p \right|^2 \Big({}_S S_1(m_1\vec{K}_1) {}_W S_1(m_2\vec{K}_2) \Big) \right] \Bigg\} \\ \cdot \delta(\omega_d + m_1\sqrt{gK_1} + m_2\sqrt{gK_2}) K_T^2 K_1 \mathrm{Sm}^2(K_T, k_{BW}, \Delta_r) dK_1 d\theta_{\vec{K}_1} dK_T \quad . \end{aligned} \tag{3.9}$$

When (3.8) and (3.9) are compared with the cross section equations for pulsed radars, the only notable distinction is that the squared sampling function, $\mathrm{Sa}(\cdot)$, is now replaced by the newly defined function, $\mathrm{Sm}(\cdot)$, that contains the sine integral. In the next section, the features of the two cross section components will be further analyzed.

3.2 The Interpretation of the RCS for an FMCW waveform

3.2.1 The First-order Cross Section Analysis

Figures 3.1 and 3.2 illustrate the smoothed versions of the first-order cross section for both pulsed and FMCW radars, with the operating frequencies being 15 MHz and 5 MHz, respectively. For the FMCW operation, the operating frequency is taken to be

the central frequency of the sweep bandwidth, B.

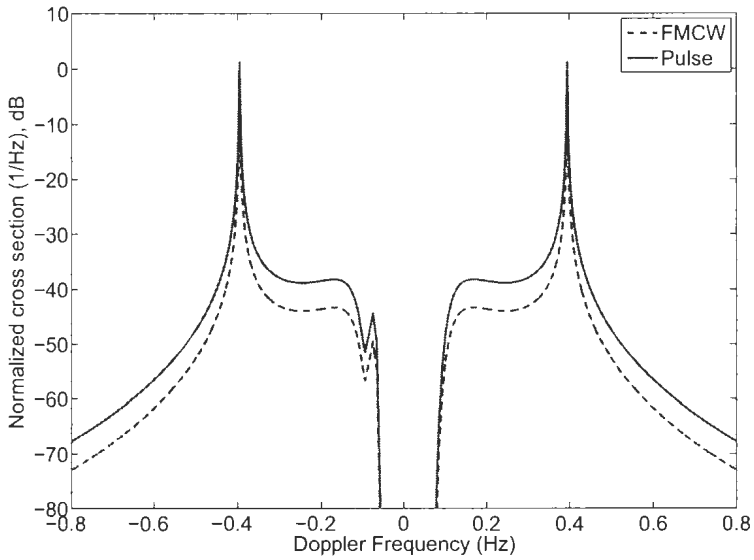

Figure 3.1: A comparison between the first-order cross sections for pulsed and FMCW waveforms. The operating frequency is $f_0 = 15$ MHz, the sweep bandwidth is $B = 100$ kHz, the wind speed is 10 m/s, and the wind direction is 90° to the radar look direction. The patch width is $\Delta\rho = 1000$m, and the integral limit $\Delta_r = \Delta\rho/2$.

It can be observed from both figures that the maxima, i.e., the two prominent Bragg peaks which are determined by $\omega_B = \pm\sqrt{2gk_0}$, are coincident. However, the sidelobe level in the FMCW case is significantly lower than that for the pulsed case. This suggests that the first-order swell peaks, which can be rarely observed due to its proximity to the noise floor and the second-order structures, are now even harder to detect in the FMCW case. In other words, it is unrealistic to extract any valid swell information from these first-order swell peaks.

3.2.2 The Second-order Cross Section Analysis

In order to carry out the calculation for the second-order cross section, the Sm(·) function must be first addressed. It has been stated in [30] that when $\Delta\rho \to \infty$ so

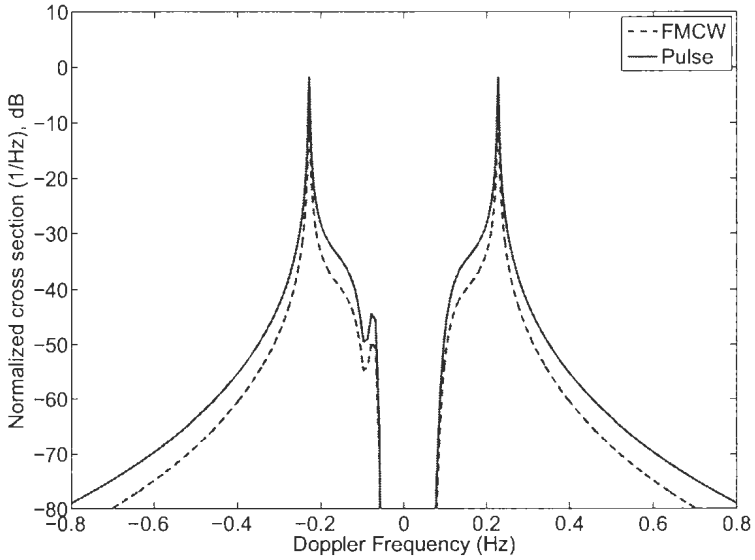

Figure 3.2: A another comparison when the operating frequency is $f_0 = 5$ MHz. The remaining parameters are identical to those in Fig. 3.1.

that $\Delta_r \to \infty$ (which means large radial patch width in practice), we have

$$\lim_{\Delta_r \to \infty} \mathrm{Sm}^2(K_T, k_{BW}, \Delta_r) \approx h\Big[K_T - (2k_0 - k_{BW})\Big] - h\Big[K_T - (2k_0 + k_{BW})\Big] \quad (3.10)$$

where $h(\cdot)$ denotes the Heaviside function. Assuming that the other terms in (3.9) vary slowly for the following wave number interval (which is very reasonable since k_{BW} is almost negligible compared to k_0),

$$2k_0 - k_B < K_T < 2k_0 + k_B \quad (3.11)$$

the right hand side of (3.10), within such a narrow wave number interval, may be replaced by a squared sampling function as

$$h\Big[K_T - (2k_0 - k_B)\Big] - h\Big[K_T - (2k_0 + k_B)\Big] \approx \mathrm{Sa}^2\Big[\frac{\Delta\rho}{2}(K_T - 2k_0)\Big] \,. \quad (3.12)$$

Substituting (3.12) back into (3.9), it may be easily seen that the second-order cross section in the FMCW case reduces to its counterpart in the pulsed case, i.e., equation (2.59). Thus, we can start the numerical calculation using the same techniques employed in Section 2.4.3.

Fig. 3.3 shows the combined first- and second-order cross sections for the two cases of the FMCW and pulsed waveforms. Since the first-order power surrounding Bragg peaks in the FMCW case decays faster than that in the pulsed case, the definition of swell peaks is correspondingly higher in the former case. Still, the amplitudes and positions of the swell peaks are identical in the two curves, which indicates that any inversion algorithm for swell information can be indiscriminately applied to either FMCW or pulsed radar operation.

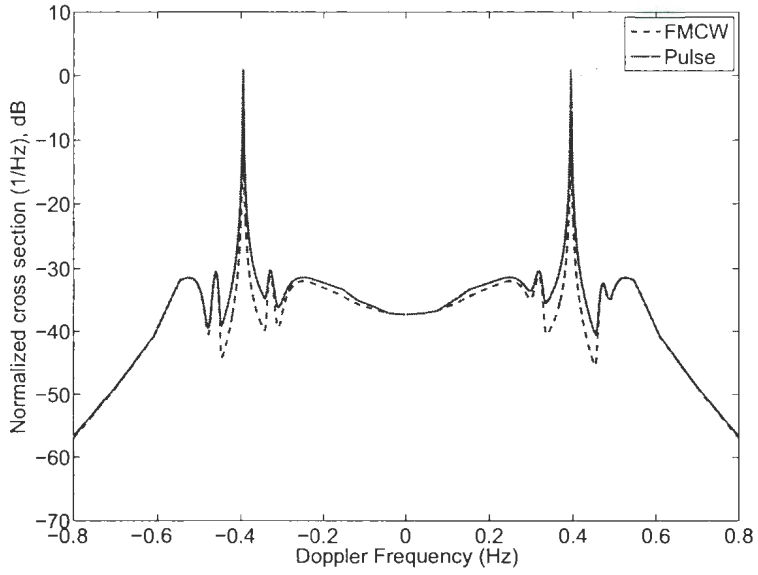

Figure 3.3: A full comparison between the cross sections of the FMCW and pulsed waveforms. The operating frequency is $f_0 = 15$ MHz. The remaining parameters are identical to those in Fig. 3.1.

3.3 General Chapter Summary

In this chapter, the first- and second-order cross sections of swell-contaminated seas have been derived for the case involving an FMCW source. Since the ocean surface profile is independent from the excitation source being applied, the obtained cross section results were very similar to those for the pulsed radar operation.

One thing worth noticing is that the first-order cross section in the FMCW case has lower sidelobes than that in the pulsed case, and the power level in the Bragg region decays faster. This produces slightly higher definition for the second-order swell peaks. However, such tiny differences would not significantly affect the development of an inversion algorithm. Thus, the automated swell inversion routine presented in the next Chapter may be applied to either the pulse or FMCW case.

Chapter 4

Extraction of Swell Parameters from Noisy HF Radar Signals

Having derived the first- and second-order radar cross sections of swell-contaminated seas, the major goal in this chapter is to develop an automated inversion algorithm for swell information from radar sea echoes. This piece of work is partially accomplished in [65]. Basically, to completely reconstruct a directional swell wave height spectrum, the following parameters are required: the swell peak frequency, f_s (or period, T_s), the dominant direction, θ_s, the frequency spreading (or later known as the shape factor, N), the significant wave height, ${}_SH_s$, and the directional spreading, s, for a typical cardioid model. For the purpose of illustration, the received radar time series with external white Gaussian noise is first simulated, from which the Doppler spectrum is estimated as a periodogram. Next, all second-order swell peaks, which contain a large amount of information regarding the swell component, are identified in the spectrum. The Doppler positions of these swell peaks are then processed through a robust routine to minimize the negative effects of low quality signals. Then, the processed values are used to calculate the dominant period and propagation direction

of swell. Meanwhile, the half-power width of each swell peak is extracted in order to derive the frequency spreading of the unknown swell wave height spectrum. Finally, the various amplitudes of swell peaks are normalized to the respective Bragg peak power, and by doing so, the dependence on the wind wave information is eliminated from the inversion routine. Thus, the obtained value can be used to estimate the swell significant wave height as well as its directional spreading.

Next, the proposed inversion algorithm is tested on a large set of simulated data. Based on the results, some final additions to the routine will be made to improve the overall extraction performance. Finally, the effects of changing local sea states are particularly investigated, and the limitations of the algorithm are revealed.

4.1 Simulation of the Doppler Spectrum in a Noisy Environment - Pulse Radar Operation

From equation (2.22), the full expression for the received time series from swell-contaminated seas at time t referenced to the start of the pulse sequence can be given by combining (2.15) and (2.55) as

$$
\begin{aligned}
E(t) = & -j\eta_0 \Delta l \Delta\rho I_0 k_0^2 \frac{F^2(\rho)}{(2\pi\rho)^{3/2}} e^{-j\frac{\pi}{4}} e^{jk_0\Delta\rho} \\
& \cdot \Bigg\{ \sum_{\vec{K},\omega} \Big({}_{S1}P_{\vec{K},\omega} + {}_{W1}P_{\vec{K},\omega} \Big) \sqrt{K} e^{j\omega t} e^{j\rho K} \mathrm{Sa}\Big[\frac{\Delta\rho}{2}(K - 2k_0) \Big] + \sum_{\vec{K}_1,\omega_1} \sum_{\vec{K}_2,\omega_2} \\
& \Big[\Big({}_C\Gamma_p + 2_E\Gamma_p \Big) {}_{S1}P_{\vec{K}_1,\omega_1} {}_{W1}P_{\vec{K}_2,\omega_2} + \Gamma_p \Big({}_{S1}P_{\vec{K}_1,\omega_1} {}_{S1}P_{\vec{K}_2,\omega_2} + {}_{W1}P_{\vec{K}_1,\omega_1} {}_{W1}P_{\vec{K}_2,\omega_2} \Big) \Big] \\
& \cdot \sqrt{K_T} e^{j(\omega_1+\omega_2)t} e^{j\rho K_T} \mathrm{Sa}\Big[\frac{\Delta\rho}{2}(K_T - 2k_0) \Big] \Bigg\}
\end{aligned}
\tag{4.1}
$$

Since the electromagnetic coupling effects have been proven to be negligible when seeking the swell information, we may simply remove all ${}_E\Gamma_p$ from (4.1). Also, the

Fourier coefficient, ${}_{S1}P_{\vec{K},\omega}$ and ${}_{W1}P_{\vec{K},\omega}$ are already defined in (A.9), and the coupling coefficient ${}_{C}\Gamma_p$ is taken to be identical with ${}_{H}\Gamma_p$. Therefore, we may rewrite (4.1) as

$$
\begin{aligned}
E(t) = & -j\eta_0 \Delta l \Delta\rho I_0 k_0^2 \frac{F^2(\rho)}{(2\pi\rho)^{3/2}} e^{-j\frac{\pi}{4}} e^{jk_0\Delta\rho} \\
& \cdot \Bigg\{ \sum_{m=\pm 1} \int_{\vec{K}} \Big(\sqrt{{}_{S}S_1(m\vec{K})} e^{jm\epsilon_s(m\vec{K})} + \sqrt{{}_{W}S_1(m\vec{K})} e^{jm\epsilon_w(m\vec{K})} \Big) \\
& \cdot \sqrt{K} e^{-jm\sqrt{gK}t} e^{j\rho K} \mathrm{Sa}\Big[\frac{\Delta\rho}{2}(K - 2k_0)\Big] \sqrt{\frac{1}{2} d\vec{K}} \\
& + \sum_{m_1=\pm 1} \sum_{m_2=\pm 1} \int_{\vec{K}_1} \int_{\vec{K}_2} \Big[{}_{H}\Gamma_p \Big(\sqrt{{}_{S}S_1(m_1\vec{K}_1)} \sqrt{{}_{W}S_1(m_2\vec{K}_2)} e^{jm_1\epsilon_s(m_1\vec{K}_1)} e^{jm_2\epsilon_w(m_2\vec{K}_2)} \\
& \quad + \sqrt{{}_{S}S_1(m_1\vec{K}_1)} \sqrt{{}_{S}S_1(m_2\vec{K}_2)} e^{jm_1\epsilon_s(m_1\vec{K}_1)} e^{jm_2\epsilon_s(m_2\vec{K}_2)} \\
& \quad + \sqrt{{}_{W}S_1(m_1\vec{K}_1)} \sqrt{{}_{W}S_1(m_2\vec{K}_2)} e^{jm_1\epsilon_w(m_1\vec{K}_1)} e^{jm_2\epsilon_w(m_2\vec{K}_2)} \Big) \Big] \\
& \cdot \sqrt{K_T} e^{-j(m_1\sqrt{gK_1} + m_2\sqrt{gK_2})t} e^{j\rho K_T} \mathrm{Sa}\Big[\frac{\Delta\rho}{2}(K_T - 2k_0)\Big] \sqrt{\frac{1}{4} d\vec{K}_1 d\vec{K}_2} \Bigg\}
\end{aligned}
\tag{4.2}
$$

with the constraint $\vec{K_T} = \vec{K_1} + \vec{K_2}$ still holding. From Lathi [55], we may replace the squared sampling function in (4.2) by

$$
\Delta\rho \mathrm{Sa}\Big[\frac{\Delta\rho}{2}(K_T - 2k_0)\Big] = \sqrt{\Delta\rho} \cdot \sqrt{\Delta\rho \mathrm{Sa}^2\Big[\frac{\Delta\rho}{2}(K_T - 2k_0)\Big]} \approx \sqrt{\Delta\rho} \cdot \sqrt{2\pi\delta(K - 2k_0)}
\tag{4.3}
$$

so that (4.2) can be simplified as

$$
\begin{aligned}
E(t) = M\sqrt{\Delta\rho} \Bigg\{ & \sum_{m=\pm 1} \int_{\vec{K}} \Big(\cdot \Big) \sqrt{\Delta\rho K} e^{-jm\sqrt{gK}t} e^{j\rho K} \mathrm{Sa}\Big[\frac{\Delta\rho}{2}(K - 2k_0)\Big] \sqrt{\frac{1}{2} d\vec{K}} \\
& + \sum_{m_1=\pm 1} \sum_{m_2=\pm 1} \int_{\vec{K}_1} \int_{\vec{K}_2} \Big[\cdot \Big] \sqrt{K_T} e^{-j(m_1\sqrt{gK_1} + m_2\sqrt{gK_2})t} e^{j\rho K_T} \sqrt{\frac{2\pi}{4} \delta(K_T - 2k_0) d\vec{K}_1 d\vec{K}_2} \Bigg\}
\end{aligned}
\tag{4.4}
$$

where the constant before the brace and the terms in the bracket are omitted for compactness, but are obvious by comparing with (4.2). Again, by employing the

facts that $d\vec{K}_2 = d\vec{K}_T$ and that the radar is operated with a very narrow beam, we may eliminate the integral over $\vec{K}_2$ by resorting to the delta constraint under the square root so that (4.4) becomes

$$E(t) = M\sqrt{\Delta\rho}\Bigg\{ \sum_{m=\pm 1} \int_{\vec{K}} \Big(\cdot \Big) \sqrt{\Delta\rho K} e^{-jm\sqrt{gK}t} e^{j\rho K} \mathrm{Sa}\Big[\frac{\Delta\rho}{2}(K - 2k_0)\Big] \sqrt{\frac{1}{2} d\vec{K}} \\ + \sum_{m_1=\pm 1} \sum_{m_2=\pm 1} \int_{\vec{K}_1} \Big[\cdot \Big] \sqrt{2k_0} e^{-j(m_1\sqrt{gK_1} + m_2\sqrt{gK_2})t} e^{j\rho 2k_0} \sqrt{\frac{4\pi k_0}{4} d\vec{K}_1 d\theta_{\vec{K}_T}} \Bigg\} . \quad (4.5)$$

Finally, noting that $\theta_{\vec{K}_T} \equiv \theta_{\vec{K}}$ and both lie along the radar look direction, we may further simplify (4.5) as

$$E(t) = M\sqrt{\Delta\rho d\theta_{\vec{K}}}\Bigg\{ \sum_{m=\pm 1} \int_{K} \Big(\cdot \Big) \sqrt{\Delta\rho} K e^{-jm\sqrt{gK}t} e^{j\rho K} \mathrm{Sa}\Big[\frac{\Delta\rho}{2}(K - 2k_0)\Big] \sqrt{\frac{1}{2} dK} \\ + \sum_{m_1=\pm 1} \sum_{m_2=\pm 1} \int_{K_1} \int_{\theta_{\vec{K}_1}} \Big[\cdot \Big] \sqrt{2\pi} k_0 e^{-j(m_1\sqrt{gK_1} + m_2\sqrt{gK_2})t} e^{j\rho 2k_0} \sqrt{K_1 dK_1 d\theta_{\vec{K}_1}} \Bigg\} . \quad (4.6)$$

To numerically simulate the time series in (4.6), the integration limits for the dK, dK_1 and $d\theta_{\vec{K}_1}$ integrals must be clarified. For $d\theta_{\vec{K}_1}$, the limit is simply 0 to 2π, because the ocean waves may travel in any direction. Likewise, for dK and dK_1, the theoretical limit is 0 to ∞ since the ocean waves may theoretically have any wavelength. However, it is understood that the energy contained within high-frequency (large wavenumber) ocean waves is negligible when compared with that in lower-frequency waves. In other words, for large numbers of K and K_1, we have that

$$ {}_S S_1(\vec{K}) = 0, \ {}_W S_1(\vec{K}) \approx 0, \\ \text{and } {}_S S_1(\vec{K}_1) = 0, \ {}_W S_1(\vec{K}_1) \approx 0. \quad (4.7)$$

Thus, an upper limit, instead of ∞, can be assigned to the dK and dK_1 integrals. In our simulation, this upper limit is set to be $6k_0$, which is seen to be sufficiently large. Now the electric field time series may be simulated directly from (4.6) by converting the integral equation to a summation equation. Note that the constant before the brace is assigned a value of unity due to a later normalization in which it would be removed anyway.

Based on the obtained time series, the external white Gaussian noise with a definite SNR can be added. In Fig. 4.1, an example of two minutes noisy time series is plotted, where the SNR is set to 30 dB. The existence of sinusoidal components can be clearly observed, and these sinusoids are predicted to give rise to the Bragg peaks in the backscatter Doppler spectrum.

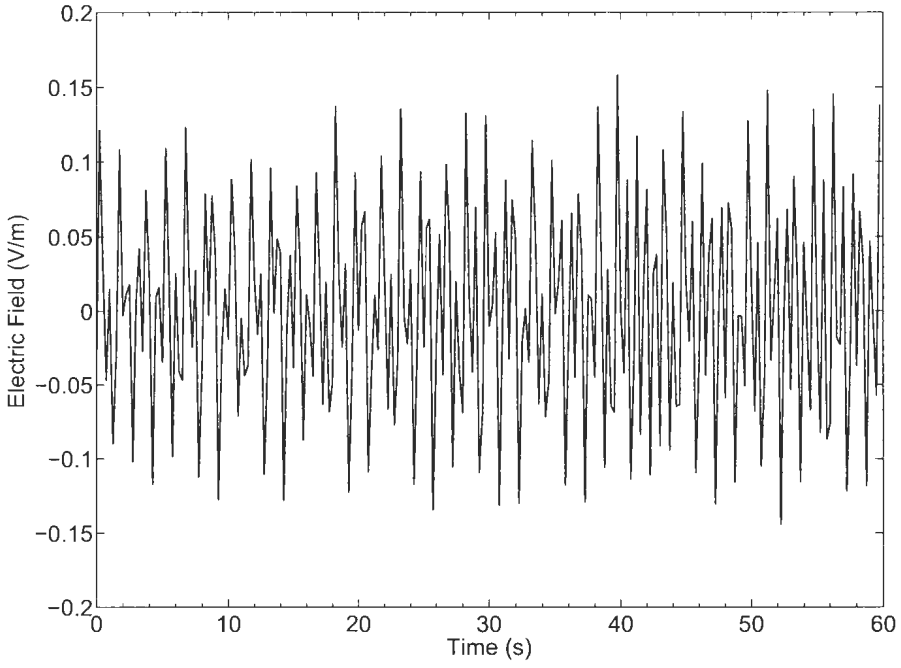

Figure 4.1: An example of a typical 1 minute simulated time series received from swell-contaminated seas. The radar operating frequency is 15 MHz, and the SNR for this signal is 30 dB.

As a final step, the Doppler spectrum of the time-varying electric fields received from swell-contaminated seas is calculated as a periodogram. Fig. 4.2 depicts the corresponding Doppler spectrum of the E-field in Fig. 4.1. The overall quality of the spectrum is quite rough due to the lack of averaging, a concept which will be introduced in the next section.

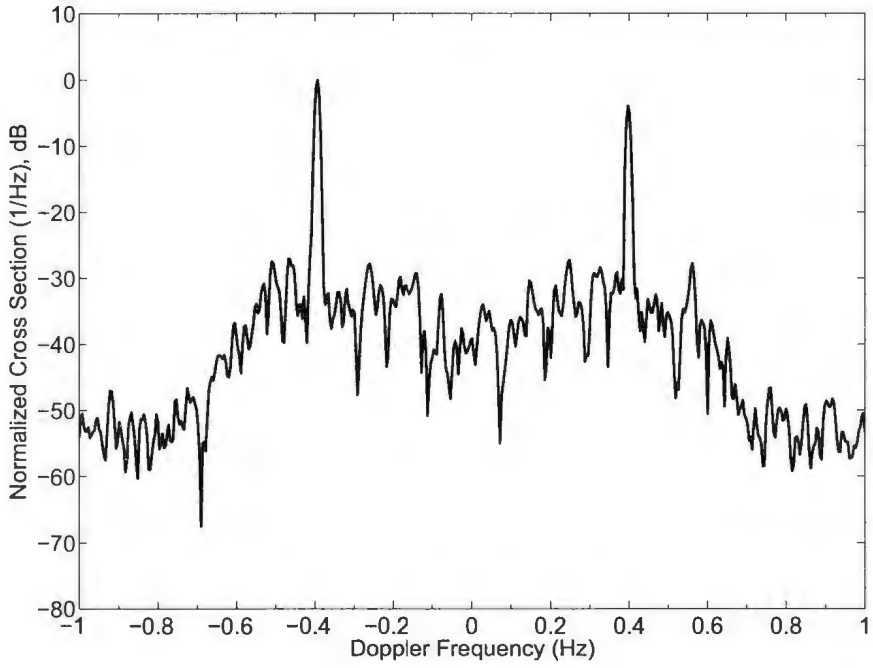

Figure 4.2: The normalized Doppler spectrum of the times series shown in Fig. 4.1.

4.2 Pre-processing of the Received Doppler Spectrum

Prior to applying any inversion algorithm on the Doppler spectrum, there are two essential steps that need to be performed. Firstly, the frequency shift, Δf, induced by the possible surface current, needs to be removed. Otherwise, the Bragg peaks

may be located at different Doppler frequencies in each range cell and, when averaged, cause severe spectral broadening and peak bifurcation. Secondly, the various Doppler spectra collected from different ranges and timing will be averaged both spatially and temporally to reduce the noise level and enhance the overall signal to allow better extraction of swell information.

4.2.1 Removal of the frequency shift induced by surface current

As noted, the frequency shift, Δf, away from the theoretical Bragg frequency, f_B, needs to be removed prior to any further manipulation of the Doppler spectrum (see Fig. 4.3). Although this frequency shift can be used to determine the radial velocity of surface current, it is irrelevant to the inversion process for swell. Thus, this frequency shift shall be removed beforehand, preparing a cleaner Doppler spectrum ready to be interpreted.

In order to return the correct value of Δf, both the theoretical positions and actual Doppler positions of the two Bragg peaks must be first identified. The theoretical Bragg frequency is simply related to the transmitting frequency, f_0, through (1.1) as

$$f_B = \pm\sqrt{\frac{g}{\pi\lambda_0}} = \pm\sqrt{\frac{gf_0}{\pi c}} \tag{4.8}$$

where c is the speed of light and g is the acceleration due to gravity. Meanwhile, when it comes to the identification of actual Bragg peaks, a windowing approach is applied, where we assume the general positions of Bragg peaks are within a relatively small window around the theoretical Bragg lines. Usually, a window of ± 0.1 Hz, centred at f_B, is used, and the most prominent peak within the window is identified as the Bragg peak. After comparing the power of the two obtained peaks, we retain

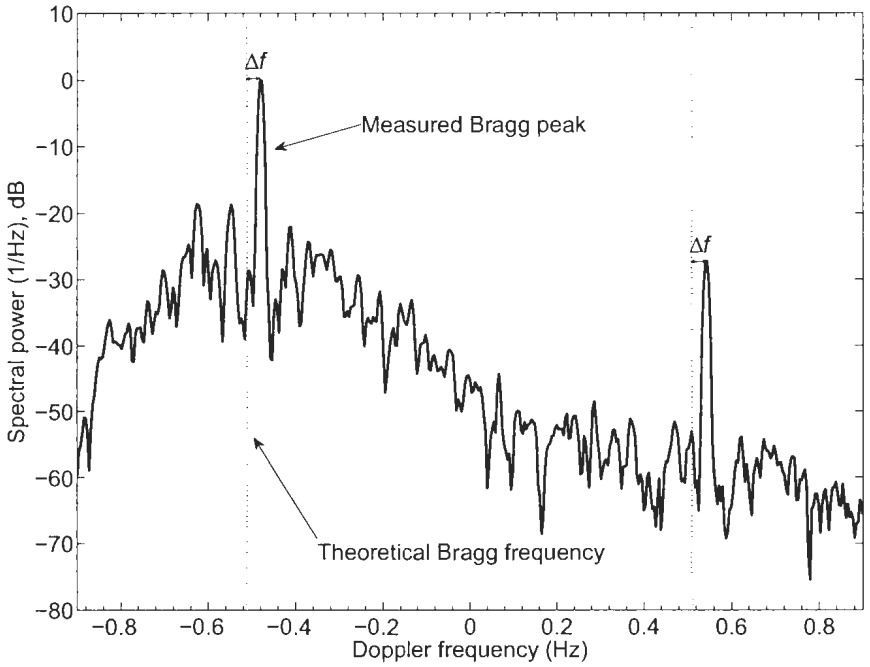

Figure 4.3: Evaluation of the Doppler shift Δf induced by surface current

only the stronger one since it is less likely to be affected by external noise and signal degradation. The shift of this strong peak away from the theoretical Bragg frequency is then calculated. This value of Δf can be then removed from the entire Doppler spectrum. Generally, the identification of first-order features should be unambiguous due to their favorable SNR, so that the two prominent Bragg peaks are left exactly at their theoretical positions after the processing.

Again, it must be noted that incoherent averaging of Doppler spectra (which will be introduced in the next section) without the removal of Δf may result in a smearing of spectral peaks, because the velocities of surface currents averaged over the area may vary significantly. With such smearing, the accurate identification of the swell peaks would become impossible.

4.2.2 Incoherent Averaging of Doppler Spectra

Incoherent averaging is an essential step to smooth the backscattered Doppler spectrum and to lower the noise floor. Prior to averaging, the second-order structure of the spectrum is often irregular and very difficult to identify (see Fig. 4.2); yet after averaging over a sufficiently long period and an area large enough, the inherent randomness of the ocean surface as well as the external noise will be suppressed so that the signal is greatly enhanced. Of course, the removal of the Doppler shift induced by surface currents and the normalization of Doppler spectra collected from different range cells have already been taken before averaging.

The first averaging concept is the temporal averaging. Since swell is generated in a remote region, it reacts very slowly to local wind conditions (on the order of hours [50]), we may smooth the spectrum temporally without significantly compromising the resolution. The fundamental concept is to segment the received time series during one radar interrogation into individual frames with 75% overlap and calculate the Doppler spectrum of each one [15]. Then, the obtained spectra are averaged to yield the final spectrum.

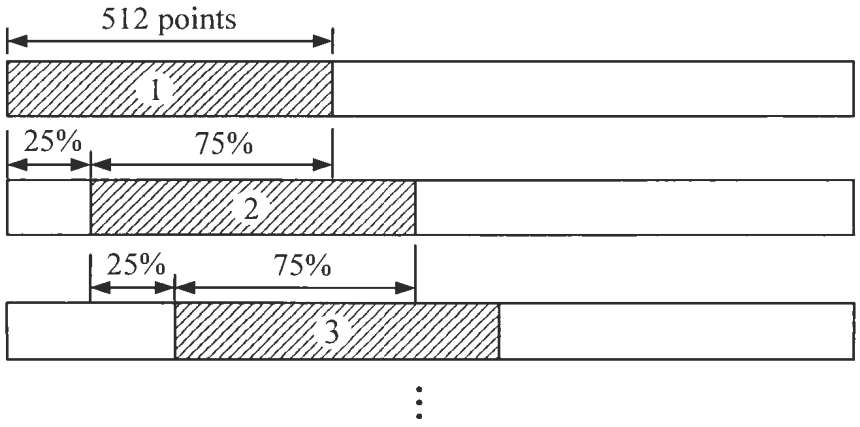

Figure 4.4: An illustration of the temporal averaging. Each frame has 512 points, and the overlapping is 75 %.

Another averaging scheme is the spatial averaging. Generally, the sea states are uniform over a large area, which is particularly true for long-period ocean waves in deep water such as swell. These waves are not so sensitive to the changes of wind fields as shorter waves, and their wave heights and directions do not vary greatly in different range cells. Therefore, spatial averaging over several neighbouring ocean patches is a desirable option to enhance the spectrum for the extraction of swell parameters.

However, caution must be taken when choosing the number of range cells to be averaged. Usually, there is a trade off between the increase in spectral clarity and spatial resolution, and a compromise shall be determined empirically. This is done by gradually increasing the number of averaged cells, starting from 1, until the desired second-order regions are distinguishable above the noise, while the spatial resolution is still acceptable (see Fig. 4.5). Note that during simulation, this spatial averaging procedure is conducted on multiple Doppler spectra created from the same set of input parameters.

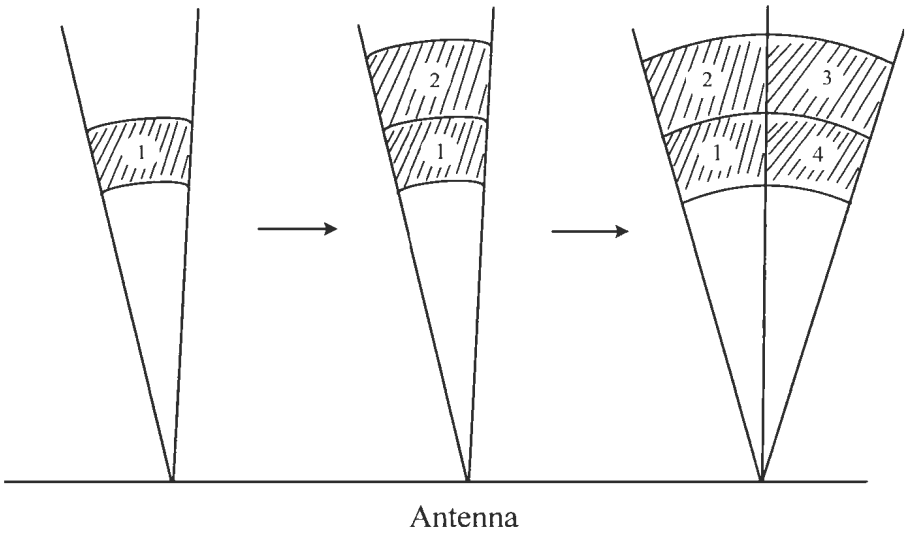

Figure 4.5: An example of the spatial averaging. The number of involved range cells are 1, 2, and 4, respectively.

Sample Doppler spectra resulted from the above two averaging methods are shown

in Figures 4.6, 4.7 and 4.8. Obviously, the interference from surrounding noise is minimized, and the second-order features are much clearer.

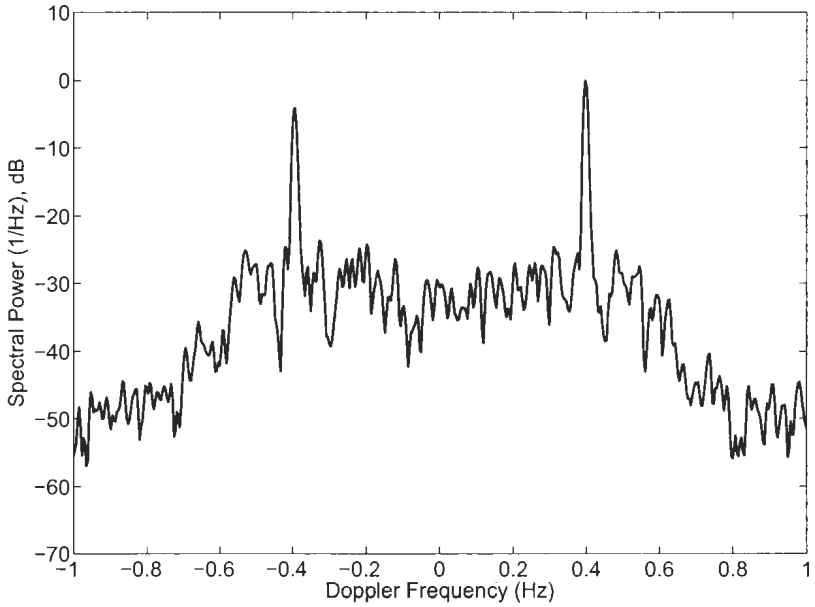

Figure 4.6: A Doppler spectrum obtained from a two-minute times series. No averages are performed.

Upon completing the essential pre-processing described above, a Doppler spectrum with fine spectral clarity and adequate Doppler resolution is ready for further manipulation. At this stage, the extraction of swell parameters can finally commence.

4.3 Extraction of Swell Period and Dominant Direction

The first two swell parameters to be extracted are the swell period and dominant direction. As was discussed in the previous chapter, these two parameters directly determine the Doppler positions of the swell peaks. Thus, it is clear that the correct

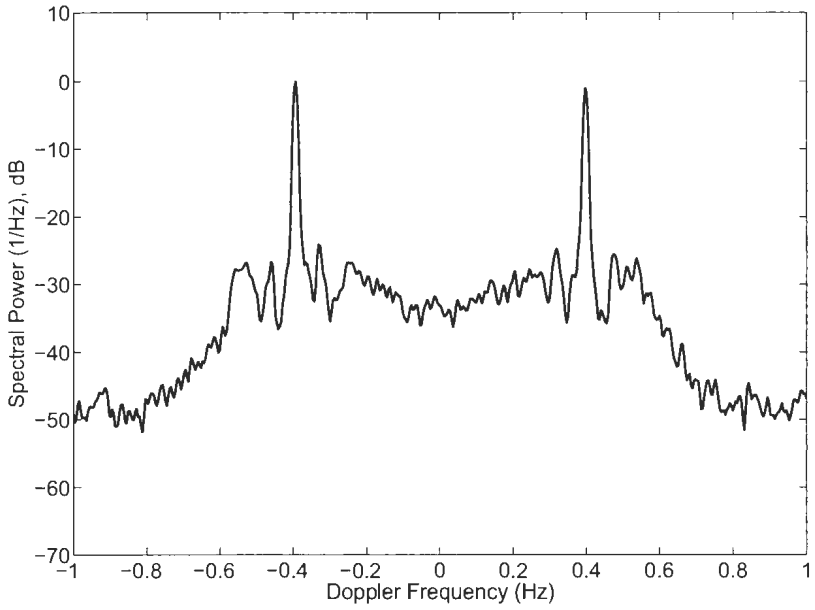

Figure 4.7: A Doppler spectrum averaged over ten minutes, with each frame being two-minute long.

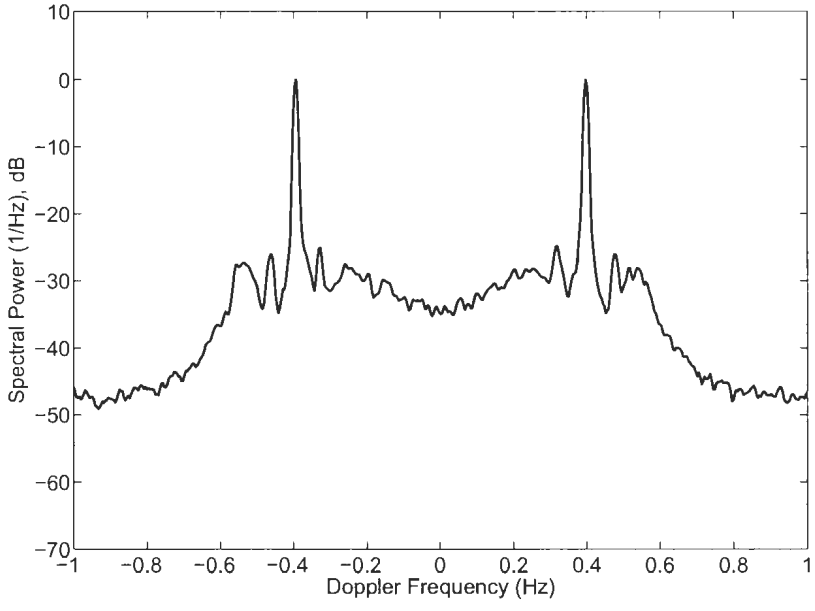

Figure 4.8: A Doppler spectrum both temporally and spatially averaged. A total of four range cells are involved.

identification of second-order swell peak positions is fundamental to the whole inversion process. Although these peaks are positioned almost symmetrically about the first-order Bragg peak and may not be so difficult to manually identify within each spectrum, this is not feasible in real practice considering the amount of data to be analyzed and the "real-time" requirement of radar operations. Thus, an automated and robust peak identification routine must be first developed. This process is described thoroughly in the following three subsections.

4.3.1 Defining Frequency Windows for Swell Peaks

When determining the possible locations of the swell peaks, a windowing scheme, as was used when locating the first-order Bragg peaks, is employed. It is assumed that the general positions of the swell peaks are within a relatively small window with clear boundaries. As was suggested by (2.59), the positions of the four swell peaks largely depend on the dominant wave number of the swell component, K_s, as in

$$\omega_{sp} = m_1\sqrt{gK_s} + m_2\sqrt{gK_w} \tag{4.9}$$

where ω_{sp} denotes the Doppler frequency of the swell peaks, and K_s is the dominant wave number of the swell. Physically, K_s and K_w are the wave numbers of the two interacting waves responsible for the maximum backscatter from the swell-contaminated region, and they should satisfy the relation that

$$\vec{K}_s + \vec{K}_w = \vec{K}_B \tag{4.10}$$

where $\vec{K}_B$ denotes the Bragg wave vector. Obviously, since swell generally consists of very long-period waves, the corresponding K_s is usually quite small, which means

that [23] (see Fig. 1.5 for illustration)

$$|\vec{K_w}| = |\vec{K}_B - \vec{K}_s| \approx |\vec{K}_B| \quad . \tag{4.11}$$

Thus, we may safely approximate (2.49) as

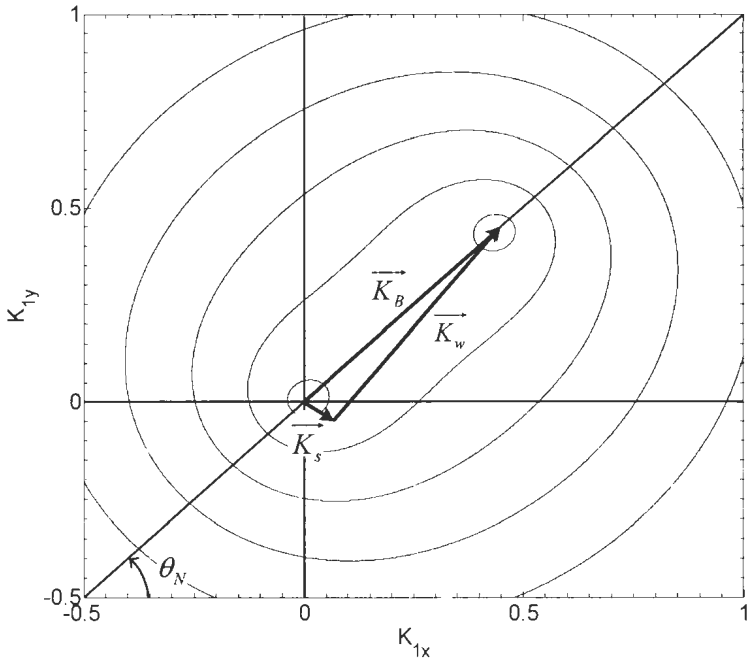

Figure 4.9: Geometry of the double scatter involving a swell vector $\vec{K}_s$ and a wind wave vector $\vec{K_w}$

$$\omega_{sp} \approx m_1\sqrt{gK_s} + m_2\sqrt{gK_B} = m_1\omega_s + m_2\omega_B \tag{4.12}$$

where ω_B is the Bragg frequency, $\omega_s = \frac{2\pi}{T_s}$ gives the angular peak frequency of the swell, and T_s denotes the swell period.

Clearly, since the theoretical ω_B is already fixed for a given set of radar parameters, the appropriate swell window shall be solely determined by the lower and upper wave periods that separate swell from wind waves. These boundaries are defined by

Kinsman [66] and Barrick [15] as 10 seconds and 16 seconds, respectively. In our case, a more conservative upper limit of 18 seconds is chosen so that all possible swell peaks are included. Now the two boundaries can be converted to a frequency window of ± 0.055 Hz to ± 0.1 Hz, sitting on both sides of the Bragg peak. For example, for a radar operating at 25 MHz, which corresponds to a Bragg frequency of ± 0.51 Hz, the four swell peaks are expected to be found within the windows shown in Table 4.1. For the purpose of illustration, Fig. 4.10 shows two windows surrounding the receding Bragg peak, and two clean swell peaks are easily identified within each.

Table 4.1: Frequency windows containing possible swell peaks

	Frequency window (Hz)
Swell peak 1	-0.610 — -0.565
Swell peak 2	-0.455 — -0.410
Swell peak 3	0.410 — 0.455
Swell peak 4	0.565 — 0.610

4.3.2 Swell Peak Identification

With the search range narrowed down, the swell peak detection process may be commenced. Although most swell peaks are visually identifiable, it is not so straightforward to pick them out in an automated routine. On the one hand, due to the proximity of the second-order continuum to the noise floor, the true swell information can be easily obscured by noise spikes that possess magnitudes similar to those of the swell peaks. On the other hand, the swell peak could be buried in the adjacent wind wave continuum, which makes it difficult to extract. Moreover, signal degradation in the form of bifurcation or broadening can sometimes impact the accuracy of detection. Thus, the automated swell peak identification should be a two-step process: 1) identify all peaks within the target window, 2) filter the ones that do not satisfy the swell peak feature.

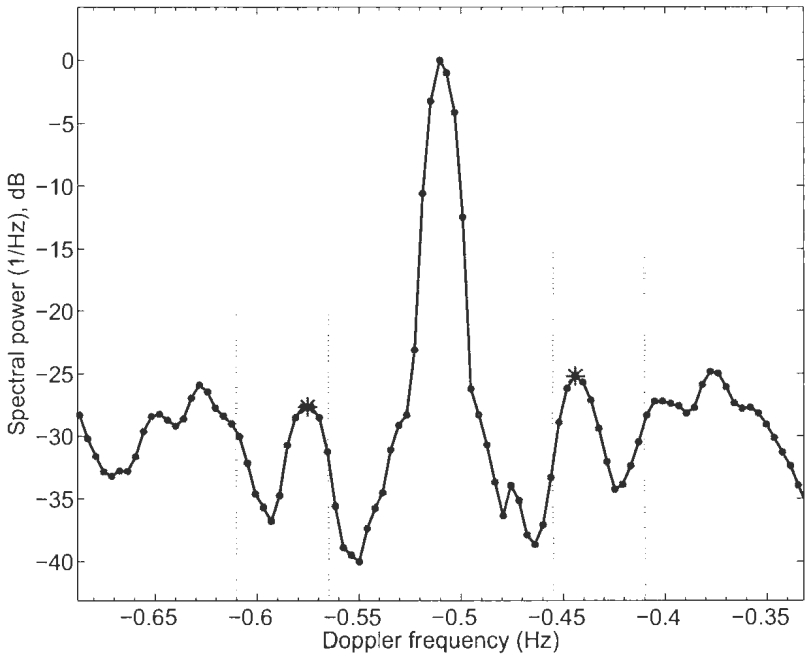

Figure 4.10: Receding Bragg peak at -0.51 Hz, flanked by two clean swell peaks (asterisk). The dashed lines indicate the frequency window boundaries as presented in Table 4.1.

To initiate the first step, all peaks and nulls (excluding the end points) within each window are first collected from the Doppler spectrum (see Fig. 4.11). This is done by examining the sign of the derivative of each point; whenever the sign changes, the corresponding point is taken as a possible peak or null. Next, a 3 dB threshold is adopted to filter out spurious peaks (see Figures 4.12 & 4.13). Basically, when a peak is too close to the surrounding nulls, it is unlikely to be a valid swell peak. However, it must be noted that this threshold value (3 dB) is empirically chosen and may be subject to changes between different data sets because of varying sea states, noise regimes, and radar parameters. For instance, when the local sea state or the swell significant height is high, this 3 dB threshold may need to be adjusted to larger values (e.g., 6 dB). The same should be done when the SNR is low so that more false peaks

could appear within the swell peak window.

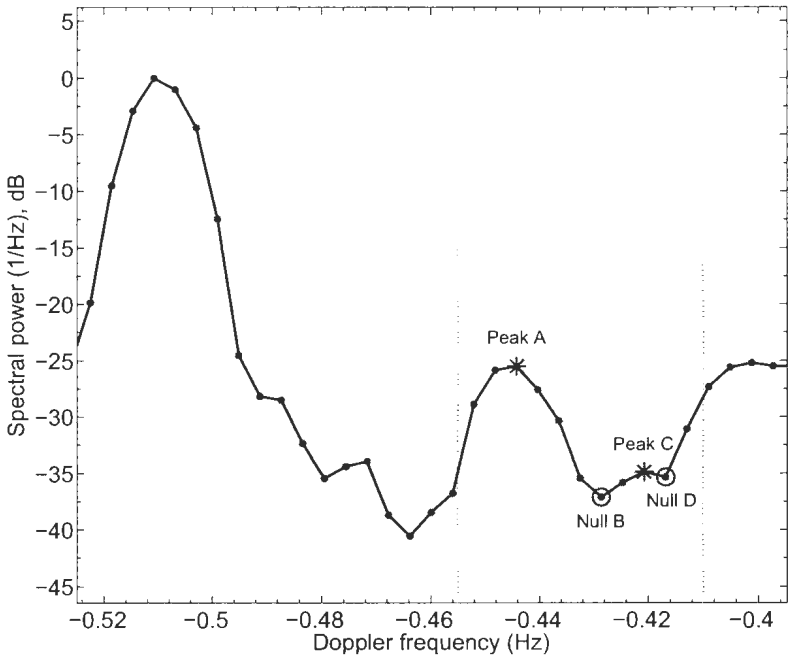

Figure 4.11: A close examination of the frequency window to collect all peaks and nulls.

In most cases, namely when a high-quality return signal is received, only one prominent swell peak will be left in each window after filtering (see Fig. 4.10). However, in the case of low SNR or extremely low swell peak amplitudes, confusion may occur, and two or more "legitimate" swell peaks may be detected within each window. To eliminate such interference, we employ the fact that "swell peaks should be positioned theoretically at equal distances from their respective Bragg peak" (see Appendix B.2 for derivation), and calculate the displacement of each detected swell peak away from its relevant Bragg peak. For instance, in Fig. 4.14, three candidates, swell peaks A, B and C, are detected. Among them, two peaks that are most symmetrically positioned relative to the Bragg peak are defined as a pair (clearly, B and C make a pair in this case). In every Doppler spectrum, a maximum of two pairs will be found, flanking the

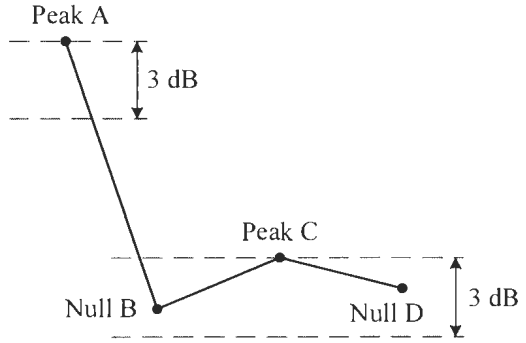

Figure 4.12: The four points collected from Fig. 4.11. Peak A is clearly more than 3 dB higher than the nearest null, Null B, and will be retained. On the contrary, Peak C is within the 3 dB range of both Null B and Null D and will be filtered out.

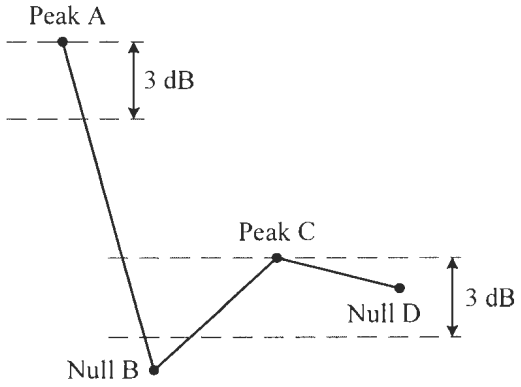

Figure 4.13: When a peak is 3 dB higher than either one of the nearest nulls, it is a potential swell peak. In this case, both Peak A and Peak C will be retained.

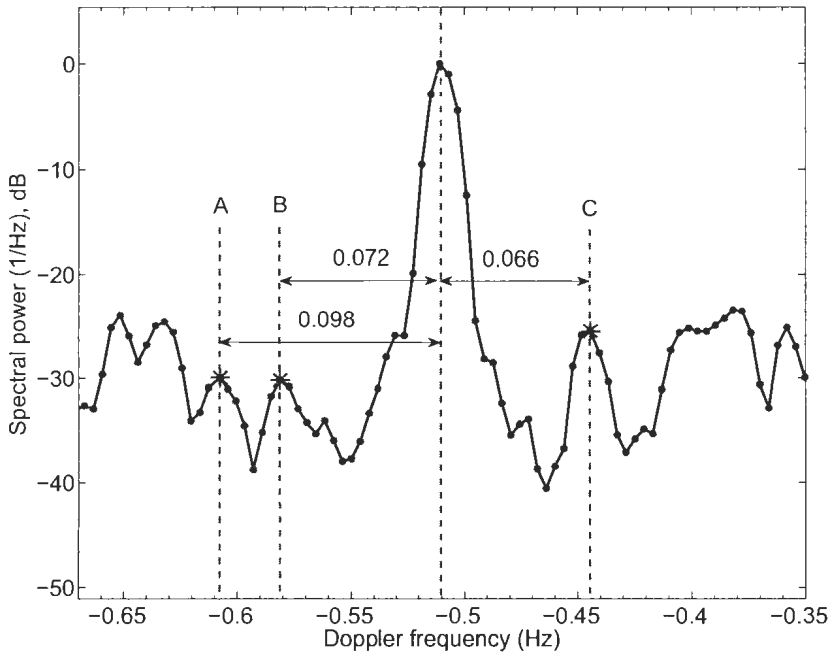

Figure 4.14: Measuring distances of swell peaks away from the respective Bragg peak. In this figure, swell peak B and C will be selected as a pair, while peak A will be eliminated.

approaching and receding first-order Bragg regions. Upon completing the filtering, four identified swell peaks are ready for further processing.

4.3.3 Processing of Swell Peaks

Despite the care given during the peak identification process, errors such as bifurcation or broadening still occur due to inherent system noise and surface current structures. Usually, the sign of such degradations is the severe asymmetry of a pair of swell peaks (e.g. the distance from one swell peak to its respective Bragg peak exceeds that of the other one by at least twice the Doppler resolution). To minimize these negative effects, a weighted mean approach is utilized, as is discussed in [50]. This routine adjusts the positions of adversely affected swell peaks according to the amplitudes of nearby data points via

$$\bar{f} = \frac{\sum P_i(f_i - f_m)}{\sum P_i} \tag{4.13}$$

where i ranges from 1 to 5 and denotes all 5 data points involved (with 2 points on each side of the target swell peak), f_m gives the average frequency of the 5 points, which is simply the original position of the swell peak, $\bar{f}$ denotes the frequency shift from the original position to the adjusted new position, and f_i and P_i give the respective frequency and amplitude of each data point in the Doppler spectrum. It can be observed from Fig. 4.15 that if the peak is well defined and roughly symmetrical (right peak of the pair), its position will remain almost unchanged; on the contrary, when disruption such as bifurcation or broadening occurs (the left peak of the pair), the peak position will be adjusted to a more reasonable value. Thus, this weighted mean algorithm can be applied indiscriminately to all swell peak pairs that suffer from severe signal degradations.

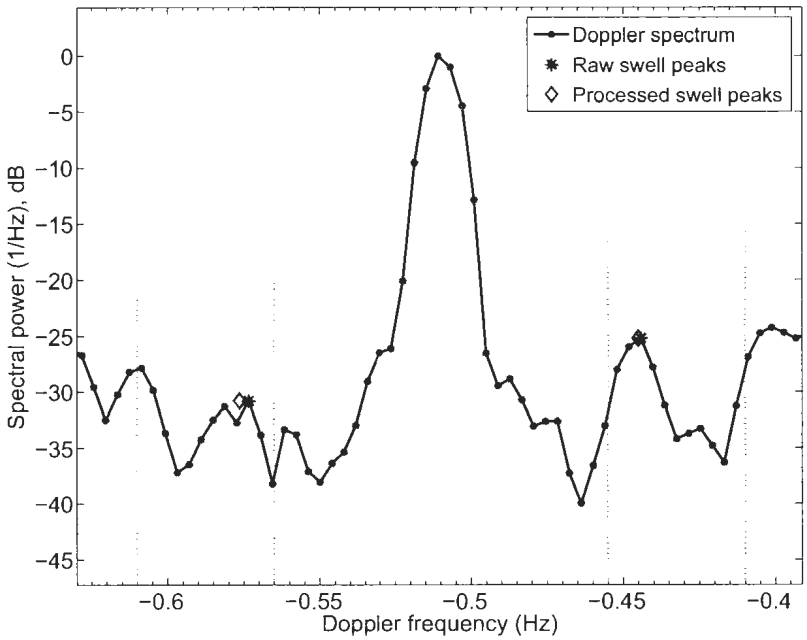

Figure 4.15: Application of the weighted mean algorithm to swell peaks when the severe signal degradation occurs.

4.3.4 Applying Inversion Formulas

Having identified the positions for the four swell peaks, we can finally apply the inversion formulas to extract the swell period and dominant direction. If we define Δf^+ as the frequency displacement between the two swell peaks surrounding the approaching Bragg peak and likewise Δf^- for the displacement between the two peaks surrounding the receding Bragg peak, the inversion formula can be given as (the detail can be found in Appendix B.2)

$$T_s = \frac{4}{\Delta f^+ + \Delta f^-} \tag{4.14}$$

and

$$\theta_s = \theta_N \pm \cos^{-1}\left(8 f_B \frac{(\Delta f^+ - \Delta f^-)}{(\Delta f^+ + \Delta f^-)^2}\right) \tag{4.15}$$

where θ_N denotes the radar look direction, and f_B is the usual Bragg frequency. The $\pm$ sign indicates the existence of an inherent directional ambiguity due to the $\cos^{-1}$ term in (4.15) (see Fig. 4.16). As is the case for wind direction extraction, the deployment of a dual radar station could solve this ambiguity.

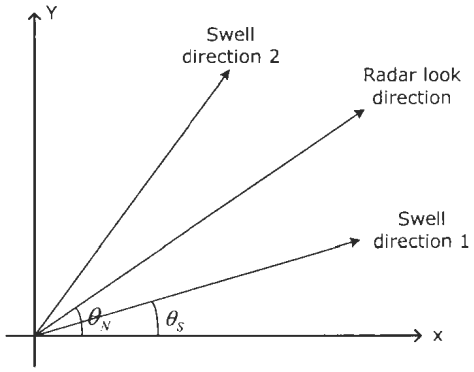

Figure 4.16: The inherent ambiguity in swell direction calculation

4.4 Extraction of the Shape Factor

Another key element in reconstructing the swell spectrum is the frequency spreading, or the shape factor, N, in a Wallop spectrum. Here the full expression for the Wallop spectrum is repeated as [63]

$$S_s(\omega) = A * G_o * (\frac{\omega}{\omega_p})^{-N} * \exp\left[\frac{-N}{4(\frac{\omega}{\omega_p})^4}\right] \tag{4.16}$$

where N is the parameter being sought here. Clearly, if the half-power width, ω_{hp}, of $S_s(\omega)$ is known, a set of equations can be constructed to numerically solve N via

$$\begin{cases} (1-\frac{\omega_L}{\omega_s})^{-N} * \exp\left[\frac{-N}{4(1-\frac{\omega_L}{\omega_s})^4}\right] = \frac{1}{2} * \exp\left[-\frac{N}{4}\right], & (a) \\ (1+\frac{\omega_R}{\omega_s})^{-N} * \exp\left[\frac{-N}{4(1+\frac{\omega_R}{\omega_s})^4}\right] = (1-\frac{\omega_L}{\omega_s})^{-N} * \exp\left[\frac{-N}{4(1-\frac{\omega_L}{\omega_s})^4}\right] & (b) \end{cases} \tag{4.17}$$

where $\omega_L + \omega_R = \omega_{hp}$, and ω_s is the peak angular frequency of the swell component as shown in Fig. 4.17. Thus, acquiring a precise value of ω_{hp} is a priority.

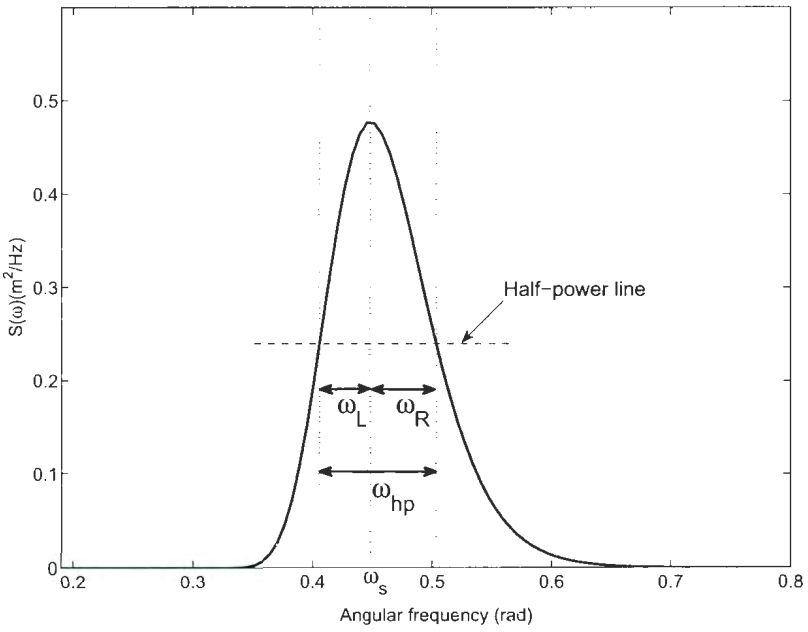

Figure 4.17: A typical swell spectrum with parameters notated in (4.16)

Intuitively, ω_{hp} will be related to the half-power width of the second-order swell peaks, ω_{Dhp}. As was suggested by Lipa and Barrick [23], ω_{Dhp} consists of contribution from the finite frequency spreading of the swell spectrum and its finite angular spreading as

$$\omega_{Dhp}^2 = \omega_{fs}^2 + \omega_{\theta s}^2 \tag{4.18}$$

where ω_{Dhp} denotes the swell peak half-power width in the Doppler spectrum, and ω_{fs}, $\omega_{\theta s}$ indicate the frequency spreading and angular spreading, respectively. More-

over, ω_{fs} can be particularly related to ω_{hp} via

$$\omega_{hp} = \frac{\omega_{fs}}{\left| m_1 + m_2 \dfrac{\omega_s^3 - m_1\omega_B^2\omega_s\cos(\theta_s - \theta_N)}{\left[\omega_s^4 - 2m_1\omega_B^2\omega_s^2\cos(\theta_s - \theta_N) + \omega_B^4\right]^{3/4}} \right|} \tag{4.19}$$

Finally, Barrick noticed that the frequency spreading term almost always dominates the angular spreading term, implying that $\omega_{Dhp} \approx \omega_{fs}$. Thus, ω_{Dhp} directly relates to ω_{hp} through (4.19). This approximation is successfully verified in our simulations by measuring the values for ω_{Dhp}, ω_{hp} under various situations. Now, the problem of finding ω_{hp} turns into finding the accurate value of ω_{Dhp}, or f_{Dhp}.

Consider, as an example, the swell peak in Fig. 4.18. We first define a half-power

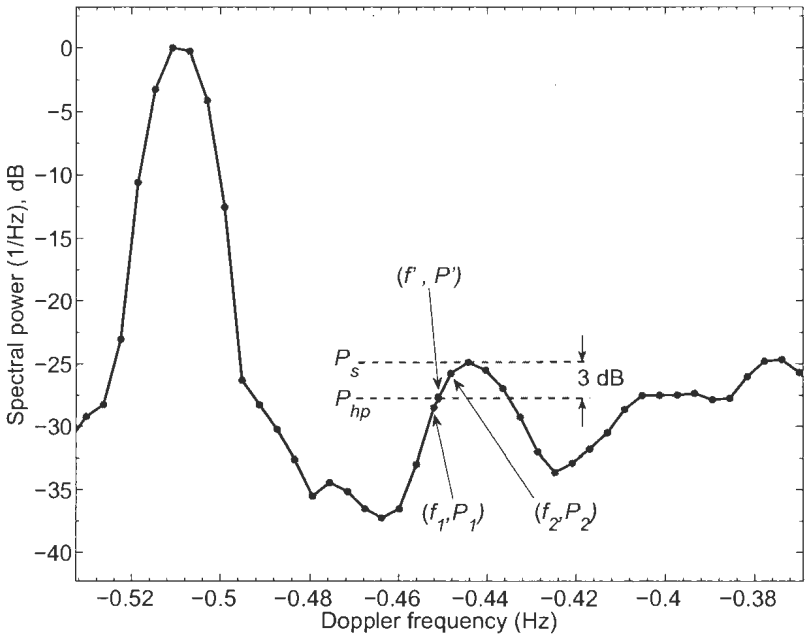

Figure 4.18: Extraction of f_{Dhp} from the right-hand side peak of the receding Bragg peak

line crossing the peak, and try to find the data points (f_1, P_1), (f_2, P_2) that surround

the left-hand side intersection point, (f', P'). Then, the exact value of f' can be then deduced as

$$f' \approx f_1 + \frac{P' - P_1}{P_2 - P_1}(f_2 - f_1) \quad . \tag{4.20}$$

By repeating the same procedure on the right-hand side data points, the corresponding half-power width can be easily calculated. However, in cases where the swell peak is almost obscured so that only one intersection point is obtained (i.e. see Fig. 4.19), we assume ω_{Dhp} to be twice the distance from this intersection to the swell peak. After averaging over all four calculated half-power widths, we may substitute this newly-obtained ω_{Dhp} back into (4.19) and then (4.17) and numerically solve the equations. In most practical situations, the value of N for swell should lie between 20 and 50.

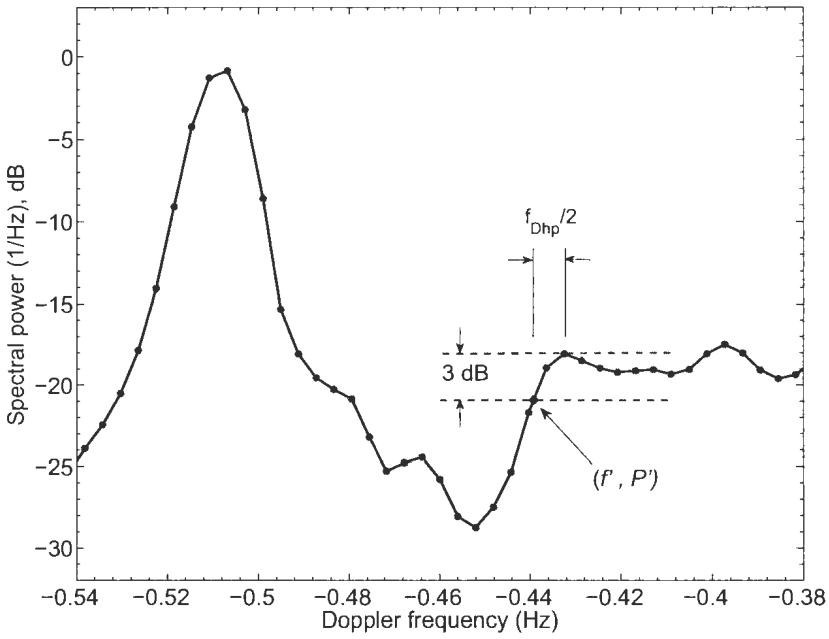

Figure 4.19: Extraction of f_{Dhp} when only one intersection point is found

4.5 Extraction of the Swell Wave Height

The remaining parameters required to reconstruct the swell directional spectrum are its significant wave height, ${}_SH_s$, and angular spreading s in a conventional cardioid directional spreading. Both parameters can be extracted by examining the swell peak amplitudes. However, the angular spreading for swell components usually ranges between 30 and 50, and changing the value of s does not significantly affect the swell peak amplitude. In other words, the inversion for the angular spreading can be extremely unstable. Thus, a typical value of 40 is chosen and fixed for s. This significantly reduces the complexity of the extraction process.

As has been discussed previously, for long-period swell (with small wave number K_s), it follows from (4.11) that the other vector $\vec{K}_w$ is approximately equal to the Bragg wave vector, implying that $S(\vec{K}_w) \approx S(\vec{K}_B)$. Thus, we may normalize the second-order spectrum by the power in the neighboring first-order peak so that only the information concerning the swell component will be left [23]. To do so, we first clarify the theoretical amplitude of the Bragg peak as

$$\sigma_1(\omega_B) = 16\pi k_0^2 \Delta\rho_s \sum_{m=\pm 1} {}_WS_1(m\vec{K}_B) \frac{K_B^{\frac{5}{2}}}{\sqrt{g}} \mathrm{Sa}^2\Big[\frac{\Delta\rho_s}{2}\Big(K_B - 2k_0\Big)\Big] \tag{4.21}$$

where ${}_SS_1(m\vec{K}_b)$ is omitted from the equation since it is negligibly small. Meanwhile, from (2.59), the theoretical amplitudes for the four swell peaks are

$$\begin{aligned}\sigma_2(\omega_{sp}) = 4\pi k_0^2 \Delta\rho \sum_{m_1=\pm 1} \sum_{m_2=\pm 1} \int_0^{\infty}\int_{-\pi}^{\pi}\int_0^{\infty} \Big[\big|{}_H\Gamma_p\big|^2 \Big({}_SS(m_1\vec{K}_1){}_WS(m_2\vec{K}_B)\Big)\Big] \\ \cdot \delta(\omega_{sp} + m_1\sqrt{gK_1} + m_2\sqrt{gK_2}) K_T^2 K_1 \mathrm{Sa}^2\Big[\frac{\Delta\rho}{2}(K_T - 2k_0)\Big] dK_1 d\theta_{\vec{K}_1} dK_T\end{aligned} \tag{4.22}$$

where the electromagnetic coupling coefficient, as well as first square bracket in (2.59)

are omitted.

Now, the normalized quantity can be defined as

$$
\begin{aligned}
R_{m_1,m_2} &= \frac{\sigma_2(\omega_{sp})}{\sigma_1(\omega_B)} \\
&= \frac{4\pi k_0^2 \Delta\rho}{16\pi k_0^2 \Delta\rho \left(\frac{(2k_o)^{2.5}}{g^{0.5}}\right)} \cdot \sum_{m_1=\pm 1} \sum_{m_2=\pm 1} \int_0^{\infty} \int_{-\pi}^{\pi} \int_0^{\infty} \Big\{ S_1(m_1 \vec{K}_1)|_H \Gamma_P|^2 \\
&\cdot K_T^2 \mathrm{Sa}^2\Big[\frac{\Delta\rho}{2}\Big(K_T - 2k_0\Big)\Big] \delta\Big(\omega_{sp} + m_1\sqrt{gK_1} + m_2\sqrt{gK_2}\Big) K_1 \Big\} dK_1 d\theta_{\vec{K_1}} dK \qquad (4.23)
\end{aligned}
$$

where as usual, $m_1, m_2 = \pm 1$ corresponds to four different swell peaks. If we further apply the approximation that [55]

$$
\mathrm{Sa}^2\Big[\frac{\Delta\rho}{2}\Big(K - 2k_0\Big)\Big] = \frac{2\pi\delta(K - 2k_0)}{\Delta\rho} \quad , \qquad (4.24)
$$

(4.23) could be simplified as

$$
\begin{aligned}
R_{m_1,m_2} = \frac{\pi\sqrt{g}}{2\Delta\rho\sqrt{2k_0}} \sum_{m_1=\pm 1} \sum_{m_2=\pm 1} \int_0^{\infty} \int_{-\pi}^{\pi} \Big\{ & S_1(m_1 \vec{K}_s)|_H \Gamma_P|^2 \\
& \cdot \delta\Big(\omega_{sp} + m_1\sqrt{gK_1} + m_2\sqrt{gK_2}\Big) K_1 \Big\} dK_1 d\theta_{\vec{K_1}} \quad . \qquad (4.25)
\end{aligned}
$$

Basically, equation (4.25) gives the theoretical value of the swell peak power normalized to the respective Bragg peak power. However, in actual practice, the Bragg peak often suffers from frequency smearing, which means the Bragg peak power is dissipated into the nearby Doppler frequencies. Thus, a more stable approach to find the Bragg peak power is to integrate the Doppler spectrum over a small window containing the Bragg peak, so that (4.25) becomes

$$
R_{m_1,m_2} = \frac{\sigma_2(\omega_{sp})}{\int_{\omega_B - \Delta\omega}^{\omega_B + \Delta\omega} \sigma_1(\omega_d) d\omega_d} \qquad (4.26)
$$

where $\Delta\omega$ usually takes the value of (0.01Hz $\times 2\pi$) rad.

As a final step, the actual value of R_{m_1,m_2} is calculated from the Doppler spectrum, and the wave height ${}_S H_s$ can be found by employing the maximum likelihood method. In other words, ${}_S H_s$ is determined when the theoretical value of R_{m_1,m_2} best matches with the measured data.

Having developed the inversion algorithms for various swell parameters, we shall validate the proposed routines against simulated Doppler spectra in the next section.

4.6 Test Results

In this section, the inversion algorithm presented above is tested. Although measured radar data is preferred for future analysis, the use of simulated data will provide valuable insights into the inversion routine. As in Section 2.4, where the input variables were modified one at a time in order to examine the corresponding effects on radar cross sections, we now produce the testing data set in the same way. A "reference" Doppler spectrum is first generated by setting the input variables to their average values from field observation, based on which the subsequent Doppler spectra are obtained by changing the input variables one at a time. By doing so, both the limit and accuracy of the algorithm can be acquired.

Fig. 4.20 shows the "reference" Doppler spectrum. The operating frequency is $f_0 = 15$ MHz. The wind direction is 0°, the radar look direction is 90°, the wind speed is 10 m/s, the swell wave height is 1 m, the swell period is 14 seconds, the swell direction is 60°, the swell shaping factor is $N = 30$, and the directional spreading factor for swell is $s = 40$. Also, the length of the simulated electric field signal is 7 minutes, with the sampling frequency being 2 Hz, and no external noise is added for the moment. As mentioned previously, the Doppler spectrum is both temporally

averaged and spatially averaged.

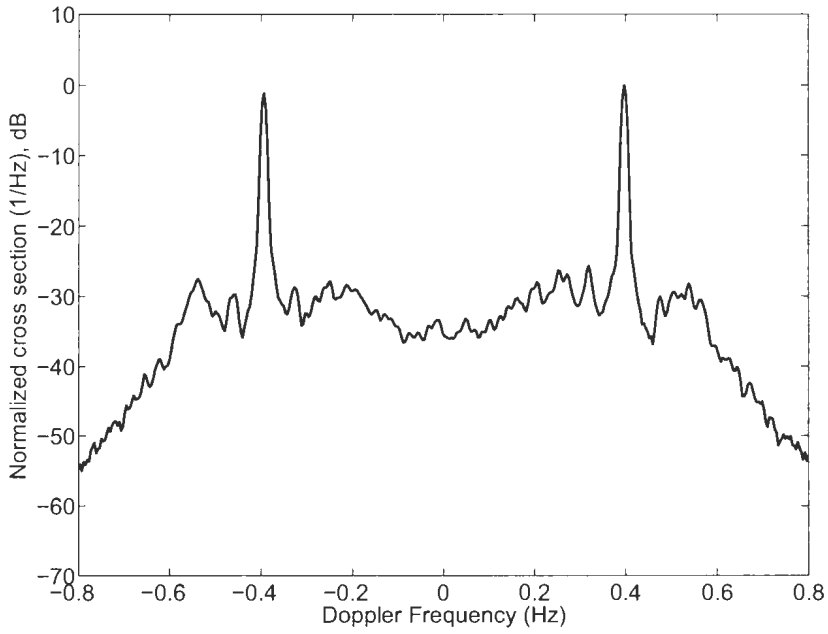

Figure 4.20: The "reference" Doppler spectrum. Only the frequency portion that contains Bragg peaks and swell peaks is shown here.

After applying the inversion algorithm introduced in Sections 4.3-4.5, we obtain the swell parameters for the above Doppler spectrum as in Table 4.2, where the

Table 4.2: Inversion results for the reference Doppler spectrum

	$T_s(s)$	$\theta_s(deg)$	N	${}_sH_s(m)$
Input	14	60	30	1
Output	13.89	70.6	21.6	0.82

directional ambiguity of θ_s is not considered. In fact, the result could be either 70.6 degrees or 109.4 degrees. It is observed that the extracted information is quite close to the original data. However, since the parameters that are used to construct Fig. 4.20 are average values from field observations, it can be expected that the accuracy of the inversion routine may decrease when one or more of the variables are changed, with

the very worst being that the algorithm is no longer feasible under extreme conditions.

The inversion results for changing the six input parameters are shown respectively in Table 4.3-4.8. Only one parameter is modified in each Table, and the remaining variables remain constant as those in the reference Doppler spectrum.

Table 4.3: Inversion results for changing the swell significant height, ${}_SH_s$

	$T_s(s)$	$\theta_s(deg)$	N	${}_SH_s(m)$
${}_SH_s = 0.5$	X	X	X	X
${}_SH_s = 1$	13.89	70.6	21.6	0.82
${}_SH_s = 2$	14.07	47.3	20.3	1.66

Table 4.4: Inversion results for changing the swell period, T_s

	$T_s(s)$	$\theta_s(deg)$	N	${}_SH_s(m)$
$T_s = 12$	11.68	74.6	X	X
$T_s = 14$	13.89	70.6	21.6	0.82
$T_s = 16$	15.89	69.8	23.7	0.85
$T_s = 18$	17.53	47.6	20.8	0.98

Table 4.5: Inversion results for changing the swell direction, θ_s

	$T_s(s)$	$\theta_s(deg)$	N	${}_SH_s(m)$
$\theta_s = 30$	X	X	X	X
$\theta_s = 60$	13.89	70.6	21.6	0.82
$\theta_s = 90$	13.78	82.3	25.5	0.88

Note that the symbol "X" indicates that the corresponding parameter cannot be extracted because the algorithm fails to locate the swell peaks or the half-power width of the swell peak. Thus, we can immediately conclude that the proposed routine may not function properly when the swell peak amplitude is too low, or when the swell peaks are too close to the second-order structures. This is clearly the case in the last line of Table 4.8, where the inverted information is totally erroneous.

Table 4.6: Inversion results for changing the swell shaping factor, N

	$T_s(s)$	$\theta_s(deg)$	N	${}_SH_s(m)$
$N = 20$	13.89	43.7	15.3	0.91
$N = 30$	13.89	70.6	21.6	0.82
$N = 40$	14.10	47.2	35.7	1.13

Table 4.7: Inversion results for changing the local wind direction, θ_w

	$T_s(s)$	$\theta_s(deg)$	N	${}_SH_s(m)$
$\theta_w = 0$	13.89	70.6	21.6	0.82
$\theta_w = 30$	13.86	32.6	20.6	1.34
$\theta_w = 60$	14.14	54.1	22.7	1.18

Aside from the situations described above, the algorithm successfully inverts the swell parameters from simulated Doppler spectra. Particularly, the inversion for the swell period is relatively stable under all circumstances, with the margin of error less than 2 %. However, the same cannot be said for the swell propagating direction, whose margin of error lies between 10 to 15 degrees. This may be explained by the fact that even fine variations in swell peak positions could result in significant error due to the $\cos^{-1}$ function in (4.15), while the Doppler resolution in our simulation is only 0.004 Hz. Predictably, the error of θ_s may be further reduced by increasing the Doppler resolution.

Compared with the randomness of θ_s, the extraction of the shaping factor tends to be undervalued, which is particularly true when the swell peaks are not prominent. The reason behind the underestimation is that at the swell height of 1 metre, the second-order swell peaks are generally very low and can be easily affected by the surrounding wind wave structures. Thus, the half-power width of the swell peaks are likely be enlarged, which renders the value of N to be underestimated. However, an error of 10 or less in N will not significantly affect the subsequent inversion for ${}_SH_s$ and may be safely neglected.

Table 4.8: Inversion results for changing the local wind speed, U_w

	$T_s(s)$	$\theta_s(deg)$	N	${}_SH_s(m)$
$U_w = 10$	13.89	70.6	21.6	0.82
$U_w = 15$	10.92	21.2	17.2	2.89

Finally, the extraction of ${}_SH_s$ is relatively unstable, with the margin of error being 10% to 20%. The major cause behind the error lies in the fact that the maximum likelihood method, used to invert for ${}_SH_s$, relies on the correct estimation of T_s, θ_s, and N; in other words, the error in the prior calculation will all be reflected in the inversion for ${}_SH_s$ and results in deviation from the input value.

In brief, the general properties of the proposed inversion algorithm apply over a large range of sea states. Low sea states (${}_SH_s < 0.5$ m), however, are excluded due to the difficulty in locating the swell peaks. Meanwhile, the accuracy of the extraction largely depends on the Doppler resolution of the radar system, with $\Delta f = 0.01$ Hz being the minimum requirement. Moreover, a dual-radar deployment is highly recommended in the ocean monitoring, which not only eliminates the directional ambiguity of the swell component, but also provides results with higher reliability.

4.7 General Chapter Summary

In this chapter, an automated inversion algorithm for swell information from the HF radar Doppler spectrum is proposed. The analysis is mainly based on the radar cross section model established in Chapter 2. Basically, the algorithm starts from the pre-processing of received Doppler spectra such as the frequency shift removal and the incoherent averaging. The next key step is to identify the Doppler positions and amplitudes of all four swell peaks if possible, from which the swell period and direction can be obtained. Then, the half-power width of the swell peaks are extracted

to invert for the shaping factor, N. Finally, based on all parameters already collected, the significant wave height for the swell component can be estimated via a maximum likelihood method. It is worth noticing that since the refined peak identification routine works with a lower buffer (3 dB), and a Wallop spectrum is adopted instead of a Gaussian frequency distribution, the applicability and generality of the inversion algorithm is considerably increased, compared with that in [50, 23].

In order to validate the proposed algorithm, a data set of Doppler spectra are created from the electric field time series, to which the inversion routines are applied. Among the five parameters that are required to reconstruct the original swell wave height spectrum, the directional spreading factor, s, is assigned a fixed value of 40 throughout the calculation to reduce the complexity while maintaining reasonable accuracy, and the other four parameters can be extracted one by one following the procedure described in this chapter. Promising inversion results are obtained, and certain limits on the target sea states are suggested. Overall, the method proposed here awaits validation by dedicated field experiments in the near future.

Chapter 5

Conclusions

5.1 General Summary and Significant Results

The development of a new HF radar cross section model for swell-contaminated seas under both pulse and FMCW operations has been accomplished. Based on this, a refined algorithm to extract swell parameters from Doppler spectra was proposed. The fundamental analysis behind this thesis can be found in [26], where a general procedure was introduced to develop radar cross sections of a good-conducting, random, time varying surface, namely, the ocean.

The analysis in this thesis started from the received electric field equations scattered from the swell-contaminated ocean surface when a pulsed source is employed. By assuming the same conditions for the surface as those in [26] (e.g., small height and small slope), it is possible to estimate the basic form of the E-field without having to re-derive a completely new set of equations from first principles. However, the specific portion indicating swell still had to be incorporated into the three dimensional Fourier representation of the random ocean surface. To do so, two different assumptions regarding the swell component were made: 1) the surface was viewed as a linear

superposition of swell and wind waves, and no interaction exists between the two, 2) a non-linear coupling term was added into the Fourier series to reflect the potential coupling effects between the two wave systems. The two cases were then investigated separately, and two sets of cross section equations were obtained. The standard procedure includes the autocorrelation of the received E-field, which, upon temporal Fourier transformation, leads to a Doppler power spectrum density. Comparison with the monostatic radar range equation then allows the derivation of Doppler cross sections per unit area of the scattering ocean surface. Note that the detail concerning ensemble averages of various field components can be found in Appendix A.

Upon deriving the first- and second-order cross sections of swell-contaminated seas, many important features of the model were analysed. On the one hand, it has been observed that the first-order cross section highly resembles its counterpart in the "wind wave only" situation, except for a small peak near zero Doppler resulted from single scatters from long-period swell. However, this first-order swell peak is most likely to be obscured by the second-order continuum and is thus incapable of providing any useful swell information. On the other hand, the second-order cross section distinguishes itself from its wind wave counterpart by four visible peaks surrounding the Bragg peaks. These peaks are hence called swell peaks and may vary significantly under different sea states. The exact effects of changing the operating frequency, the swell period, height, and direction, the local wind speed and direction have been investigated, which suggests that swell parameters could be extracted from the four swell peaks.

The results obtained for pulsed radar operation was then extended to the FMCW case, since such wave form has been widely applied due to its better resolution and less complexity in the real world. The fundamental analysis regarding the FMCW cross section development has been extensively discussed in [30], and this thesis simply

followed essentially the same path. A comparison between the cross sections of the two transmitted wave forms revealed only small differences, which is insufficient to affect the development of a swell inversion algorithm.

Finally, a data interpretation technique to recover swell information from the backscattered signals was presented. To prepare a smooth Doppler spectrum for inversion, several pre-processing methods were introduced such as frequency normalization and incoherent averaging. A refined peak recognition routine was then applied, locating the correct positions and amplitudes of swell peaks. In case that the signal is severely degraded, a post processing of swell peaks was implemented to adjust them to more reasonable positions. By applying the inversion formulas (as explained in Appendix B), the dominant period and propagating direction of the swell component can be calculated. Meanwhile, the extraction of the shape factor of the swell spectrum relies on the measurement of the half-power width of the swell peak, and the significant wave height of swell can be obtained using a maximum likelihood approach. Above all, relatively little time will be required to carry out the simple procedure, which makes it suitable for near real-time radar applications.

While the algorithm has not been applied to real data, it has been tested against simulated Doppler spectra in a noisy environment. The results showed that the algorithm is capable of providing full directional information of the swell component under certain conditions (e.g., ${}_{S}H_{s} > 0.5$ m), and better results may be achieved on higher Doppler resolution radar systems. Since the simulated Doppler spectrum originated directly from the electric field time series, one should therefore expect that the method given here will also yield reasonable results for measured data.

5.2 Suggestions for Future Work

The analysis of the cross sections for swell-contaminated seas as well as the corresponding inversion algorithm in this thesis suggest several directions for future research. The first might involve certain relaxation of the various assumptions invoked during the cross section derivation. One may notice that the incoming swell is assumed to be representable by a homogeneous and stationary zero-mean Gaussian process, while in fact, the narrow-band nature of the swell component may not fully satisfy such an assumption. Also, since the specific non-linear interaction between swell and wind waves is still unclear, this paper assumes the coupling coefficient between the two to possess the same form as that in Hasselmann's classic work [51] on non-linear energy transfer for gravity waves. This is unlikely to be completely accurate since the corresponding numerical model, developed by oceanographers [59, 11], does not totally agree with field observations on swell-contaminated seas. Lastly, the inversion algorithm does not consider the effects of surface currents, which might somehow interact with the long-period swell.

Next, the case of multiple swell components travelling from and to all directions should also be examined. One may easily notice that the wave height spectra throughout this thesis are all bimodal, while according to real buoy data, more peaks are often observed [67]. These peaks are created by different meteorological events separated thousands of miles apart, which might cause ambiguity in the backscattered signal and give spurious results. In this case, complex identification and separation approaches must be applied to distinguish different wave systems prior to any swell extraction.

As well, for certain sea states, not all four swell peaks can be located. Whenever this is the case, the insignificant swell peaks will be omitted, and thus reduce the stability of the technique. It is desirable to develop another algorithm based on fewer data points while maintaining the same level of precision. Besides, since the inversion

results for the swell significant wave height, ${}_{S}H_{s}$, were unsatisfactory considering its significance in sea warning, a more robust inversion routine, rather than the one based on the maximum likelihood method, needs to be established.

Of course, the ultimate goal would be to test the proposed algorithm on real Doppler spectra. It is expected that further dedicated experimentation would greatly aid the model verification process as well as the acceptance in the remote sensing community.

Bibliography

[1] Swell dominated sea. June, 2011. http://alinecasey.blogspot.ca.

[2] T. Hilmer. Radar sensing of ocean wave heights. Master's thesis, Univ. Hawaii, 2010.

[3] L. R. Wyatt. "The Ocean Wave Directional Spectrum". *Oceanography*, 10(2), 1997.

[4] L. R. Wyatt. "Progress in the interpretation of HF sea echo: HF radar as a remote sensing tool". *Radar and Signal Processing, IEEE Proceeding F*, 137(2):139–147, 1990.

[5] E. Gill. The scattering of high frequency electromagnetic radiation from the ocean surface: An analysis based on a bistatic ground wave radar configuration. PhD thesis, Mem. Univ. of Newfoundland, St.John's, 1999.

[6] M. D. Earle. Development of algorithms for separation of sea and swell. Technical report, National Data Buoy Center, 1984.

[7] L. F. Titov. Wind-driven waves. *Jerusalem: Israel Program for Scientific Translations*, 1969.

[8] E. F. Thompson. Energy spectra in shallow U.S. coastal water. Technical report, U.S. Army, Corps of Engineers, Coastal Engineering Research Center, 1980.

[9] W. E. Cummings, S. L. Bales, and D. M. Gentile. "hindcasting waves for engineering applications". *Proceedings of the International Symposium on Hydrodynamics in Ocean Engineering, Trondheim, Norway*, 1981.

[10] S. Aranuvachapun. "Parameters of Jonswap spectral model for surface gravity waves — II. Predictability from real data". *Ocean Engineering*, 1987.

[11] H. Tamur, T. Waseda, and Y. Miyazawa. "Freakish sea state and swell-windsea coupling: Numerical study of the Suwa-Maru incident". *Geophys. Res. Letters*, 36, 2009.

[12] D. D. Crombie. "Doppler spectrum of sea echo at 13.56 Mc/s". *Nature*, 175:681–682, 1955.

[13] W. L. Bragg. "The diffraction of short electromagnetic waves by a crystal". *Proceedigns of the Cambridge Philosophical Society*, 17:43-57, 1913.

[14] R. Stewart and J. Joy. "HF radio measurements of surface currents". *Deep-sea Research*, 21:1039–1049, 1974.

[15] D. E. Barrick. "Remote sensing of sea state by radar". *Remote sensing of the Troposphere*, 12:1–46, 1972.

[16] B. L. Weber and D. E. Barrick. "On the nonlinear theory for gravity waves on the ocean's surface. part i: Derivations". *J. Phys. Oceanogr.*, 7(1):3–10, 1977.

[17] B. L. Weber and D. E. Barrick. "On the nonlinear theory for gravity waves on the ocean's surface. part ii: Interpretation and applications". *J. Phys. Oceanogr.*, 7(1):11–21, 1977.

[18] Antenna Standards Committee of the IEEE Antennas, The Institute of Electrical Propagation Society, and New York Electronics Engineers Inc. *IEEE Standard Definitions of Terms for Antennas.* 1983.

[19] J. R. Wait. Electromagnetic surface waves. *Advances in Radio Res.*, pages 157–217, J. A. Saxton, Ed. New York: Academic, 1964.

[20] D. E. Barrick. "Theory of HF and VHF Propagation Across the Rough Sea, 1, 2, The Effective Surface Impedance for a Slightly Rough Highly Conducting Medium at Grazing Incidence". *Radio Sci.*, 6(5):517–526, 1971.

[21] J. W. Strutt. *The Theory of Sound*, volume 2. New York: Macmillan, 1945.

[22] D. E. Barrick. "First-order theory and analysis of MF/HF/VHF scatter from the sea". *IEEE Transactions on Antennas and Propagation*, 20:2–10, 1972.

[23] B. J. Lipa and D. E. Barrick. "Methods for the extraction of long-period ocean wave parameters from narrow beam HF radar sea echo". *Radio Sci.*, 15(4):843–853, 1980.

[24] D. E. Barrick and B. J. Lipa. "The second-order shallow-water hydrodynamic coupling coefficient in interpretation of HF radar sea echo". *IEEE J. Oceanic Eng.*, 11(2):310 - 315, 1986.

[25] J. Walsh and R. Donnelly. "Consolidated approach to two-body electromagnetic scattering". *Physical Review A*, 36(9):4474–4485, 1987.

[26] J. Walsh, R. Howell, and B. Dawe. Model development for evaluation studies of ground wave radar. Technical report, Contract rep. for the Dept. Nat. Defence, Government of Canada, DSS Contract Number W7714-8-5655/01-SS, C-CORE Contract Number 90-C14, 1990.

[27] J. Walsh and E. Gill. "An analysis of the scattering of high-frequency electromagnetic radiation from rough surfaces with application to pulse radar operating in backscatter mode". *Radio Sci.*, 35(6):1337–1359, 2000.

[28] E. Gill and J. Walsh. "Bistatic form of the electric field equations for the scattering of vertically polarized high-frequency ground wave radiation from slightly rough, good conducting surfaces". *Radio Sci.*, 35(6):1323–1335, 2000.

[29] E. Gill and J. Walsh. "High-frequency bistatic cross sections of the ocean surface". *Radio Sci.*, 36(6):1459–1475, 2001.

[30] J. Walsh, J. Zhang, and E. Gill. "High-Frequency Radar Cross Section of the Ocean Surface for an FMCW Waveform". *IEEE J. Ocean. Eng.*, 36(4):615–626, 2011.

[31] E. Gill and J. Walsh. "A combined sea clutter and noise model appropriate to the operation of high-frequency pulsed Doppler radar in regions constrained by external noise". *Radio Sci.*, 43:RS4012, 2008.

[32] J. Zhang, J. Walsh, and E. Gill. "Inherent limitations in High-frequency radar remote sensing based on Bragg scattering from the ocean surface". *IEEE J. Ocean. Eng.*, 37(3):395–406, 2012.

[33] J. Walsh, W. Huang, and E. Gill. "The First-Order High Frequency Radar Ocean Surface Cross Section for an Antenna on a Floating Platform". *IEEE Transactions on Antennas and Propagation*, 58(9):2994–3003, 2010.

[34] C. Shen, E. Gill, and W. Huang. "Simulation of HF radar cross sections for swell contaminated seas". *Oceans' 12 MTS/IEEE*, Hampton Roads, Virginia, Oct. 14-19, 2012.

[35] C. Shen, E. Gill, and W. Huang. "HF Radar Cross Sections of Swell Contaminated Seas For a Pulsed waveform". *IET Radar, Sonar and Navigation*, 2013, accepted.

[36] C. Shen, W. Huang, and E. Gill. "The Derivation of High Frequency Radar Cross Sections for Swell Contaminated Seas". *IEEE IGARSS 2013*, Melbourne, Australia, July 21 - 26, 2013.

[37] D. E. Barrick. "Extraction of wave parameters from measured HF radar sea-echo Doppler spectra". *Radio Sci.*, 12(3):415–424, 1977.

[38] D. E. Barrick. "The ocean waveheight nondirectional spectrum from inversion of the HF sea-echo Doppler spectrum". *Remote Sens. Environ.*, 6:201–227, 1977.

[39] B. J. Lipa. "Derivation of directional ocean-wave spectra by integral inversion of second-order radar echoes". *Radio Sci.*, 12(3):425–434, 1977.

[40] B. J. Lipa. "Inversion of second-order radar echoes from the sea". *J. Geophys. Res.*, 83(C2):959–962, 1978.

[41] D. L. Phillips. "A technique for the numerical solution of certain integral equations of the first kind". *J. Association for Compputing Machinery*, 9:84–97, 1962.

[42] S. Twomey. "On the Numerical Solution of Fredholm Integral Equations of the First Kind by the Inversion of the Linear System Produced by Quadrature". *J. Association for Compputing Machinery*, 10:97–101, 1963.

[43] D. E. Barrick and B. J. Lipa. "A compact transportable HF radar system for directional coastal wave field measurements". *Ocean Wave Climate*, pages 153–201, 1979.

[44] L. R. Wyatt. "The measurement of the ocean wave directional spectrum from HF radar Doppler spectra". *Radio Sci.*, 21(3):473–485, 1986.

[45] B. J. Lipa and D. E. Barrick. Analysis methods for narrow-beam high-frequency radar sea echo. Technical report, National Oceanic and Atmospheric Administraton, U.S. Departıment of Commerce, 1982.

[46] E. Gill and J. Walsh. "Extraction of ocean wave parameters from HF backscatter received by a four-element array: analysis and application". *Oceanic Engineering, IEEE Journal of*, 17(4):376 –386, oct 1992.

[47] R. Howell and J. Walsh. "Extraction of ocean wave spectra from HF radar returns". *Proc. Canadian Conf. on Electrical and Computer Engineering*, pages 719–722, Vancouver, Canada, 1988.

[48] B. J. Lipa, D. E. Barrick, and J. W. Maresca Jr. "HF radar measurements of long ocean waves". *Geophys. Res.*, 86(C5):4089–4012, 1980.

[49] J. S. Bathgate, M. L. Heron, and A. Prytz. "A Method of Swell-Wave Parameter Extraction From HF Ocean Surface Radar Spectra". *IEEE J. Ocean. Eng.*, 31(4):812 – 818, 2006.

[50] Jonathan S. Bathgate. Extensions to the COSRAD HF Ocean Surface Radar Extraction of swell parameters. PhD thesis, James Cook Univ., 2005.

[51] K. Hasselmann. "On the non-linear energy transfer in a gravity-wave spectrum Part 1. General theory". *J. Fluid Mech.*, 12:481–500, 1962.

[52] S. Badulin, A. Korotkevich, D. Resio, and V. Zakharov. "Wave-wave interactions in wind-driven mixed seas". *Proc. of the Rogue Waves Workshop*, Brest, France, Oct. 13-15, 2008.

[53] N. Violante Carvalho, F.J. Ocampo-Torres, and I.S. Robinson. "Buoy observations of the influence of swell on windwaves in the open ocean". *Appl. Ocean Res.*, 26(1-2):49–60, 2004.

[54] R. E. Collin. *Antennas and Radio Wave Propagation*, chapter 5, page 293. New York: McGraw-Hill, 1985.

[55] B. Lathi. *Random Signals and Communication Theory*, chapter 1. Scranton, Penn.:International Textbook Company, 1968.

[56] D. Barton. *Modern Radar Systems Analysis.* Norwood, Mass: Artech House Inc., 1987.

[57] M. Hatori, M. Tokuda, and Y. Toba. "Experimental Study on Strong Interaction between Regular Waves and Wind Waves–I". *J. Oceanographical Society of Japan*, 37:111 119, 1981.

[58] J. S. Reid. "Observational Evidence of the Interaction of Ocean Wind-sea with Swell". *Mar. Freshwater Res.*, 46:419–425, 1995.

[59] D. Masson. "On the nonlinear coupling between swell and wind waves". *J. Phys. Oceanography*, 23:1249–1258, 1993.

[60] Tucker. *Waves in Ocean Engineering.* New York: Ellis Horwood, 1991.

[61] J. B. Hinwood, D. R. Blackman, and G. T. Lleonart. "SOME PROPERTIES OF SWELL IN THE SOUTHERN OCEAN". *Proc. of the Int. Conf. on Coastal Eng.*, 18, 1982.

[62] K. Torsethaugen. "Simplified Double Peak Spectral Model for Ocean Waves". *In Proc. 14th ISOPE*, 2004.

[63] K. Torsethaugen. Characteristic for extreme sea states on the norwegian continental shelf. Technical report, Norwegian Hydrodyn. Lab., Trondheim, 1984.

[64] B. J. Lipa and D. E. Barrick. "Extraction of sea state from HF radar sea echo Mathematical theory and modeling". *Radio Sci.*, 21(1):81–100, 1986.

[65] C. Shen, E. Gill, and W. Huang. "Extraction of Swell Parameters from Simulated Noisy HF Radar Signals". *IEEE RadarCon13*, Ottawa Convention Centre, Ontario, Canada, Apr. 29 - May 3, 2013.

[66] B. Kinsman. *Wind Waves—Their Generation and Propagation on the ocean surface.* New York: Courier Dover, 2002.

[67] J. L. Hanson and O. W. Phillips. "Automated analysis of ocean surface directional wave spectra". *J. Atmos. Ocean. Technol.*, 18, 2001.

[68] W. Pierson. Wind generated waves. *Advances Geophys.*, 2:93 178, 1955.

[69] J. Thomas. *An Introduction to Statistical Communication Theory.* New York: John Wiley and Sons, 1969.

Appendix A

Calculation of the Ensemble Averages

This appendix mainly addresses the features associated with the ensemble averages appearing in Chapter 2. Section A.1 details the procedure to calculate the averages of two random Fourier coefficients that are generated either from the same wave system, or by two distinct systems. Section A.2 extends the analysis in Section A.1 to include the averages concerning four random variables. The last section, Section A.3, treats the cross-correlation of the first- and second-order E-field and confirms it to be zero.

A.1 The Ensemble Average Involving Two Random Surface Variables

In Section 2.2.2, we encountered the ensemble average involving two random surface variables (see (2.28)). As noted, these averages can be classified into two categories: the autocorrelation of two Fourier coefficients that represent the same wave system, and the cross-correlation which is a product of two different wave components. Due to

their relative importance, the autocorrelation term, $< {}_{S1}P_{\vec{K},\omega}{}_{S1}P^{*}_{\vec{K}',\omega'} >$ will be first analysed.

Prior to the calculation, we must define ${}_{S1}P_{\vec{K},\omega}$ and its complex conjugate ${}_{S1}P^{*}_{\vec{K}',\omega'}$ in some manner. According to the definition of these Fourier coefficients, we may describe the first-order surface displacement of the swell component as

$$ {}_{1}\xi_{s}(\vec{\rho},t) = \sum_{\vec{K},\omega} {}_{S1}P_{\vec{K},\omega} e^{j(\vec{\rho}\cdot\vec{K}+\omega t)} \quad . \tag{A.1} $$

Naturally, the complex conjugate of (A.1) will be

$$ {}_{1}\xi^{*}_{s}(\vec{\rho},t) = \sum_{\vec{K},\omega} {}_{S1}P^{*}_{\vec{K},\omega} e^{-j(\vec{\rho}\cdot\vec{K}+\omega t)} \quad . \tag{A.2} $$

Since the surface is real, (A.1) should be equal to (A.2), which gives the condition that

$$ \begin{aligned} {}_{S1}P_{\vec{K},\omega} &= {}_{S1}P^{*}_{-\vec{K},-\omega} \\ {}_{S1}P^{*}_{\vec{K},\omega} &= {}_{S1}P_{-\vec{K},-\omega} \quad . \end{aligned} \tag{A.3} $$

Next, the ${}_{S1}P_{\vec{K},\omega}$ is taken to have the form [32]

$$ {}_{S1}P_{\vec{K},\omega} = \sqrt{{}_{S}S_{1}(\vec{K},\omega)\,d\vec{K}\,d\omega}\cdot N_{s}(\vec{K},\omega) \tag{A.4} $$

where ${}_{S}S_{1}(\vec{K},\omega)$ denotes the first-order component of $S(\vec{K},\omega)$, the power spectral density for the ocean surface. The last factor in (A.4), $N_{s}(\vec{K},\omega)$, accounts for the randomness in the Fourier coefficients, and is later assigned a particular distribution

(see (A.12)). Combining (A.3) and (A.4), we may write ${}_{S1}P^{*}_{\vec{K}',\omega'}$ as

$$ {}_{S1}P^{*}_{\vec{K}',\omega'} = {}_{S1}P_{-\vec{K}',-\omega'} = \sqrt{{}_{S}S_1(-\vec{K}',-\omega')d\vec{K}\,d\omega}\cdot N_s(-\vec{K}',-\omega') \tag{A.5} $$

To use (A.4) and (A.5), the exact form of $S_1(\vec{K},\omega)$ must be considered. According to the linear dispersion relationship for gravity waves [66], the angular frequency, ω, and wave number, K, of a given first-order wave train can be related through

$$ \omega = \sqrt{gK\tanh(Kd)} \tag{A.6} $$

where d is the water depth. Moreover, if d is sufficiently large so that the wave is not significantly affected by the ocean bottom, i.e., when $\dfrac{d}{\lambda_0} \geqslant \dfrac{1}{4}$, $\tanh(Kd) \approx 1$, (A.6) may then be reduced to

$$ \omega = \sqrt{gK} \quad . \tag{A.7} $$

This approximation is usually valid for HF radar applications and is therefore employed throughout the remainder of this analysis. Given the linear dispersion relationship in deep water, we may conveniently express $S_1(\vec{K},\omega)$ in a generalized form as [66]

$$ S_1(\vec{K},\omega) = \frac{1}{2}\sum_{m=\pm 1} S_1(m\vec{K})\delta(\omega + m\sqrt{gK}) \tag{A.8} $$

where $S_1(\vec{K})$ denotes the first-order directional ocean wave spectrum, $m = \pm 1$ indicates the inward or outward direction along the radar look direction, and $\delta(\cdot)$ is the usual Dirac delta function.

By substituting (A.8) back into (A.4) and (A.5), we obtain a new form of ${}_{S1}P_{\vec{K},\omega}$ as

$$ {}_{S1}P_{\vec{K},\omega} = \sum_{m=\pm 1}\sqrt{\frac{1}{2}{}_{S}S_1(m\vec{K})\delta(\omega + m\sqrt{gK})d\vec{K}\,d\omega}\cdot N_s(\vec{K},\omega) \quad . \tag{A.9} $$

Similarly, ${}_{S1}P^{*}_{\vec{K}',\omega'}$ can be given by

$$ {}_{S1}P^{*}_{\vec{K}',\omega'} = \sum_{m'=\pm 1} \sqrt{\frac{1}{2} {}_{S}S_1(-m'\vec{K}')\delta(-\omega' + m'\sqrt{gK'})d\vec{K}'d\omega'} \cdot N_s(-\vec{K}', -\omega') \quad . \text{(A.10)} $$

Now, we may write the ensemble average based on equation (A.9) and (A.10) as

$$ \begin{aligned} < {}_{S1}P_{\vec{K},\omega} {}_{S1}P^{*}_{\vec{K}',\omega'} > = & \sum_{m=\pm 1} \sum_{m'=\pm 1} \sqrt{\frac{1}{4} {}_{S}S_1(m\vec{K}) {}_{S}S_1(-m'\vec{K}')} \\ & \cdot \sqrt{\delta(\omega + m\sqrt{gK})\delta(-\omega' + m'\sqrt{gK'})d\vec{K}\,d\vec{K}'d\omega\,d\omega'} \\ & \cdot < N_s(\vec{K},\omega)N_s(-\vec{K}', -\omega') > \quad . \end{aligned} \text{(A.11)} $$

Again, the $< \cdot >$ is applied to the only random factors in (A.11), i.e., $N_s(\vec{K},\omega)$. It is apparent that the statistical properties of $N_s(\vec{K},\omega)$ directly determine the nature of the whole ensemble average. For simplicity, we follow the classic model proposed by Pierson [68] and define this random phase function to take the form as

$$ N_s(\vec{K},\omega) = e^{jm\epsilon_s(m\vec{K})} \text{(A.12)} $$

where $\epsilon_s(\vec{K})$ are random phase variables uniformly distributed on $[0, 2\pi]$ for each K and they are mutually independent. It must be noted that to ensure that (A.12) is a valid form, the swell component, when separated from the local wave field, must be a Gaussian process itself. Although this perfect Gaussian assumption is almost never realized in the real world, the actual statistical property of the ocean surface seldom deviates far from it [66]. Thus, we temporarily put aside other possible types of ocean surface and continue our calculation of the ensemble average. Substituting

(A.12) into (A.11), we may observe that due to the independence of $\epsilon_s(\vec{K})$,

$$< e^{jm\epsilon_s(m\vec{K})} e^{jm'\epsilon_s(-m'\vec{K})} >= \begin{cases} 1, & m = -m',\ \vec{K} = \vec{K'} \\ 0, & \text{otherwise} \end{cases} \tag{A.13}$$

Considering (A.13) together with the delta functions in (A.11), it is straightforward to write the ensemble average regarding two swell surface variables as

$$< {}_{S1}P_{\vec{K},\omega S1}P^{*}_{\vec{K'},\omega'} >= \begin{cases} \sum_{m=\pm 1} \frac{1}{2} {}_{S}S_1(m\vec{K})\delta(\omega + m\sqrt{gK})d\vec{K}\,d\omega, & \vec{K} = \vec{K'},\ \omega = \omega' \\ 0, & \text{otherwise} \end{cases} \tag{A.14}$$

and likewise, for the wind wave component (which should also be a Gaussian process),

$$< {}_{W1}P_{\vec{K},\omega W1}P^{*}_{\vec{K'},\omega'} >= \begin{cases} \sum_{m=\pm 1} \frac{1}{2} {}_{W}S_1(m\vec{K})\delta(\omega + m\sqrt{gK})d\vec{K}\,d\omega, & \vec{K} = \vec{K'},\ \omega = \omega' \\ 0, & \text{otherwise} \end{cases} \tag{A.15}$$

which corresponds to equation (2.29) in Section 2.2.2.

Having specified the autocorrelation term, we will next focus on the cross-correlation, $< {}_{S1}P_{\vec{K},\omega W1}P^{*}_{\vec{K'},\omega'} >$, appearing in (2.28). Analogous to (A.10), the expression for ${}_{W1}P^{*}_{\vec{K'},\omega'}$ is given as

$${}_{W1}P^{*}_{\vec{K'},\omega'} = {}_{W1}P_{-\vec{K'},-\omega'} = \sqrt{{}_{W}S_1(-\vec{K'},-\omega')d\vec{K}\,d\omega}\cdot e^{jm'\epsilon_w(-m'\vec{K})} \quad . \tag{A.16}$$

Note that here the random phase factor, $\epsilon_w(-m'\vec{K})$, has a subscript w to indicate its origin to be the wind wave component instead of swell. Combining (A.9) and (A.16),

we can easily obtain the desired quantity as

$$< s_1 P_{\vec{K},\omega} w_1 P^*_{\vec{K}',\omega'} > = \sum_{m=\pm 1} \sum_{m'=\pm 1} \sqrt{\frac{1}{4} s S_1(m\vec{K}) w S_1(-m'\vec{K}')} \cdot \sqrt{\delta(\omega + m\sqrt{gK})\delta(-\omega' + m'\sqrt{gK'}) d\vec{K}\, d\vec{K}'\, d\omega\, d\omega'} \cdot < e^{jm\epsilon_s(m\vec{K})} e^{jm'\epsilon_w(-m'\vec{K})} > \quad . \tag{A.17}$$

As has already been pointed out in Section 2.2.1, the local wind waves and the incoming swell are physically generated by two wind fields separated far apart. Based on this fact, we can consider the two wave systems to be totally independent from each other. Consequently, the phase factors that represent the randomness in these two components should also be independent, which renders that

$$< e^{jm\epsilon_s(m\vec{K})} e^{jm'\epsilon_w(-m'\vec{K})} >= 0 \tag{A.18}$$

for all $\vec{K}$. Thus, we can safely write

$$< s_1 P_{\vec{K},\omega} w_1 P^*_{\vec{K}',\omega'} >=< w_1 P_{\vec{K},\omega} s_1 P^*_{\vec{K}',\omega'} >= 0 \tag{A.19}$$

which concludes that any cross-correlation involving a swell coefficient and a wind wave coefficient will simply vanish.

A.2 The Ensemble Average Involving Four Random Surface Variables

Now we will deal with the various ensemble averages appearing in (2.38). Although they all involve four random surface variables, we may classify them into four different

types. Each of these four has its unique features and will be explained successively in the following analysis.

1. In the first and second line of (2.38), there appear the averages of the first kind, i.e., the ones that involves all four elements from the same source as

$$\left\langle {}_{S1}P_{\vec{K}_1,\omega_1}\,{}_{S1}P_{\vec{K}_2,\omega_2}\,{}_{S1}P^{*}_{\vec{K}'_1,\omega'_1}\,{}_{S1}P^{*}_{\vec{K}'_2,\omega'_2}\right\rangle \quad \text{or} \quad \left\langle {}_{W1}P_{\vec{K}_1,\omega_1}\,{}_{W1}P_{\vec{K}_2,\omega_2}\,{}_{W1}P^{*}_{\vec{K}'_1,\omega'_1}\,{}_{W1}P^{*}_{\vec{K}'_2,\omega'_2}\right\rangle$$

Since these two are explicitly analogous, only the first $< \cdot >$ will be taken here as an example. Yet, before we start the calculation, a very useful conclusion from Thomas [69] shall be stated. In his work, Thomas proved that for four random variables, V_1, V_2, V_3, and V_4, which are Gaussian and zero-mean,

$$< V_1V_2V_3V_4 >=< V_1V_2 >< V_3V_4 > + < V_1V_3 >< V_2V_4 > + < V_1V_4 >< V_2V_3 > . \tag{A.20}$$

Using this idea, we may expand the above ensemble average to be

$$\begin{aligned}\left\langle {}_{S1}P_{\vec{K}_1,\omega_1}\,{}_{S1}P_{\vec{K}_2,\omega_2}\,{}_{S1}P^{*}_{\vec{K}'_1,\omega'_1}\,{}_{S1}P^{*}_{\vec{K}'_2,\omega'_2}\right\rangle &= \left\langle {}_{S1}P_{\vec{K}_1,\omega_1}\,{}_{S1}P_{\vec{K}_2,\omega_2}\right\rangle\left\langle {}_{S1}P^{*}_{\vec{K}'_1,\omega'_1}\,{}_{S1}P^{*}_{\vec{K}'_2,\omega'_2}\right\rangle \\ &+ \left\langle {}_{S1}P_{\vec{K}_1,\omega_1}\,{}_{S1}P^{*}_{\vec{K}'_1,\omega'_1}\right\rangle\left\langle {}_{S1}P_{\vec{K}_2,\omega_2}\,{}_{S1}P^{*}_{\vec{K}'_2,\omega'_2}\right\rangle \\ &+ \left\langle {}_{S1}P_{\vec{K}_1,\omega_1}\,{}_{S1}P^{*}_{\vec{K}'_2,\omega'_2}\right\rangle\left\langle {}_{S1}P^{*}_{\vec{K}'_1,\omega'_1}\,{}_{S1}P_{\vec{K}_2,\omega_2}\right\rangle .\end{aligned} \tag{A.21}$$

With the aid of (A.3), the first product of averages on the right hand side of

(A.21) becomes

$$\begin{aligned}
&\left\langle {}_{S1}P_{\vec{K}_1,\omega_1\,S1}P_{\vec{K}_2,\omega_2}\right\rangle\left\langle {}_{S1}P^*_{\vec{K}'_1,\omega'_1\,S1}P^*_{\vec{K}'_2,\omega'_2}\right\rangle \\
&= \left\langle {}_{S1}P_{\vec{K}_1,\omega_1\,S1}P^*_{-\vec{K}_2,-\omega_2}\right\rangle\left\langle {}_{S1}P_{-\vec{K}'_1,-\omega'_1\,S1}P^*_{\vec{K}'_2,\omega'_2}\right\rangle \\
&= \begin{cases} \left\langle |{}_{S1}P_{\vec{K}_1,\omega_1}|^2\right\rangle\left\langle |{}_{S1}P_{\vec{K}'_2,\omega'_2}|^2\right\rangle, & \vec{K}_1 = -\vec{K}_2, \vec{K}'_1 = -\vec{K}'_2, \omega_1 = -\omega_2, \omega'_1 = -\omega'_2 \\ 0, & \text{otherwise.} \end{cases}
\end{aligned} \tag{A.22}$$

It has already been pointed out in (2.14) that $\vec{K}_T = \vec{K}_1 + \vec{K}_2$, with K_T being the wave vector lying along the radar look direction. However, in (A.22), the constraint suggests that $\vec{K}_T = \vec{0}$, which obviously violates the known scatter condition. Therefore, this first ensemble average simply vanishes. The remaining two products of averages on the right hand side of (A.21) can be determined based on (A.14). It should be noted that the constraints for these two averages are slightly different, i.e., one is that $\vec{K}_1 = \vec{K}'_1,\ \vec{K}_2 = \vec{K}'_2,\ \omega_1 = \omega'_1,\ \omega_2 = \omega'_2$, and the other is that $\vec{K}_1 = \vec{K}'_2,\ \vec{K}_2 = \vec{K}'_1,\ \omega_1 = \omega'_2,\ \omega_2 = \omega'_1$. Still, they both meet the prerequisite condition that $\vec{K}_T = \vec{K}_1 + \vec{K}_2 = \vec{K}'_1 + \vec{K}'_2 = \vec{K}'_T$. Besides, since (A.21) is within a large summation that includes all possible wave vectors and angular frequencies (see (2.37)), two specific sets of $\vec{K}$ and ω that satisfy the two sets of constraints are sure to be found within the summation range. Now we may write the result for (A.21) as

$$\begin{aligned}
&\left\langle {}_{S1}P_{\vec{K}_1,\omega_1\,S1}P_{\vec{K}_2,\omega_2\,S1}P^*_{\vec{K}'_1,\omega'_1\,S1}P^*_{\vec{K}'_2,\omega'_2}\right\rangle \\
&= \begin{cases} \displaystyle\sum_{m=\pm 1}\frac{1}{2}{}_SS_1(m_1\vec{K}_1){}_SS_1(m_2\vec{K}_2)\delta(\omega_1 + m_1\sqrt{gK_1}) & \\ \qquad \cdot\delta(\omega_2 + m_2\sqrt{gK_2})\,d\vec{K}_1\,d\omega_1\,d\vec{K}_2\,d\omega_2, & \text{constraint A, B} \\ 0, & \text{otherwise} \end{cases}
\end{aligned} \tag{A.23}$$

The ensemble average concerning all four wind wave elements can be deduced analogously to (A.23) and will not be shown here.

2. Again in the first and second line of (2.38), we noticed the averages of another kind which involves two surface variables from one wave system, either swell or wind waves, and another two complex conjugates from the other system. For example,

$$\begin{aligned}\left\langle s1P_{\vec{K}_1,\omega_1}s1P_{\vec{K}_2,\omega_2}w1P^*_{\vec{K}'_1,\omega'_1}w1P^*_{\vec{K}'_2,\omega'_2}\right\rangle &= \left\langle s1P_{\vec{K}_1,\omega_1}s1P_{\vec{K}_2,\omega_2}\right\rangle\left\langle w1P^*_{\vec{K}'_1,\omega'_1}w1P^*_{\vec{K}'_2,\omega'_2}\right\rangle \\ &+ \left\langle s1P_{\vec{K}_1,\omega_1}w1P^*_{\vec{K}'_1,\omega'_1}\right\rangle\left\langle s1P_{\vec{K}_2,\omega_2}w1P^*_{\vec{K}'_2,\omega'_2}\right\rangle \\ &+ \left\langle s1P_{\vec{K}_1,\omega_1}w1P^*_{\vec{K}'_2,\omega'_2}\right\rangle\left\langle w1P^*_{\vec{K}'_1,\omega'_1}s1P_{\vec{K}_2,\omega_2}\right\rangle \end{aligned} \tag{A.24}$$

Clearly, the first term on the right hand side of (A.24) equals zero for the same reason as (A.22), while the remaining two terms contain the ensemble averages of a swell coefficient and a wind wave coefficient and, based on (A.19), will simply vanish. Thus, we can safely neglect the averages of this second kind.

3. In the third and fourth lines of (2.38), there exists the averages of a third sort that involves three surface variables from one wave system, and another one from the other system. By taking the first one as an example, we notice that

$$\begin{aligned}\left\langle s1P_{\vec{K}_1,\omega_1}s1P_{\vec{K}_2,\omega_2}s1P^*_{\vec{K}'_1,\omega'_1}w1P^*_{\vec{K}'_2,\omega'_2}\right\rangle &= \left\langle s1P_{\vec{K}_1,\omega_1}s1P_{\vec{K}_2,\omega_2}\right\rangle\left\langle s1P^*_{\vec{K}'_1,\omega'_1}w1P^*_{\vec{K}'_2,\omega'_2}\right\rangle \\ &+ \left\langle s1P_{\vec{K}_1,\omega_1}s1P^*_{\vec{K}'_1,\omega'_1}\right\rangle\left\langle s1P_{\vec{K}_2,\omega_2}w1P^*_{\vec{K}'_2,\omega'_2}\right\rangle \\ &+ \left\langle s1P_{\vec{K}_1,\omega_1}w1P^*_{\vec{K}'_2,\omega'_2}\right\rangle\left\langle s1P^*_{\vec{K}'_1,\omega'_1}s1P_{\vec{K}_2,\omega_2}\right\rangle. \end{aligned} \tag{A.25}$$

Clearly, since every term on the right hand side contains an average in the form of (A.19) and thus reduces to zero, we can promptly eliminate the averages of this third kind from any equations.

4. The last kind of averages can be found in the last line of (2.38) and may be expanded as

$$\begin{aligned}\left\langle {}_{S1}P_{\vec{K}_1,\omega_1 W1} P_{\vec{K}_2,\omega_2 S1} P^*_{\vec{K}'_1,\omega'_1 W1} P^*_{\vec{K}'_2,\omega'_2} \right\rangle &= \left\langle {}_{S1}P_{\vec{K}_1,\omega_1 W1} P_{\vec{K}_2,\omega_2} \right\rangle \left\langle {}_{S1}P^*_{\vec{K}'_1,\omega'_1 W1} P^*_{\vec{K}'_2,\omega'_2} \right\rangle \\ &+ \left\langle {}_{S1}P_{\vec{K}_1,\omega_1 S1} P^*_{\vec{K}'_1,\omega'_1} \right\rangle \left\langle {}_{W1}P_{\vec{K}_2,\omega_2 W1} P^*_{\vec{K}'_2,\omega'_2} \right\rangle \\ &+ \left\langle {}_{S1}P_{\vec{K}_1,\omega_1 W1} P^*_{\vec{K}'_2,\omega'_2} \right\rangle \left\langle {}_{S1}P^*_{\vec{K}'_1,\omega'_1 W1} P_{\vec{K}_2,\omega_2} \right\rangle \end{aligned} \tag{A.26}$$

Based on the analysis presented above, one may easily observe that only the middle term on the right hand side will be left and equals to

$$\begin{aligned}&\left\langle {}_{S1}P_{\vec{K}_1,\omega_1 W1} P_{\vec{K}_2,\omega_2 S1} P^*_{\vec{K}'_1,\omega'_1 W1} P^*_{\vec{K}'_2,\omega'_2} \right\rangle \\ &= \begin{cases} \sum_{m=\pm 1} \frac{1}{4} {}_S S_1(m_1\vec{K}_1)_W S_1(m_2\vec{K}_2)\delta(\omega_1 + m_1\sqrt{gK_1}) & \vec{K}_1 = \vec{K}'_1,\ \vec{K}_2 = \vec{K}'_2, \\ \quad \cdot\delta(\omega_2 + m_2\sqrt{gK_2})\, d\vec{K}_1\, d\omega_1\, d\vec{K}_2\, d\omega_2, & \omega_1 = \omega'_1,\ \omega_2 = \omega'_2 \\ 0, & \text{otherwise.} \end{cases} \end{aligned} \tag{A.27}$$

Having specified all four types of averages, we may obtain a more compact equation of the second-order autocorrelation as in (2.39) by substituting (A.23) and (A.27) back into (2.38).

A.3 The Cross-correlations of the First- and Second-order Field Components

In equation (2.26), we came across the cross-correlations of the first- and second-order electric field components as defined by

$$\begin{aligned} & \mathcal{R}_{1,2}(\tau) = < (E_n)_1(t+\tau)(E_n)_2^*(t) > \\ \text{or} \quad & \mathcal{R}_{2,1}(\tau) = < (E_n)_2(t+\tau)(E_n)_1^*(t) > \quad . \end{aligned} \tag{A.28}$$

Since these two are perfectly analogous, only the first correlation will be examined here, and the same conclusion can be easily extended to the second case.

When multiplying the first-order E-field, (2.15), and the complex conjugate of the second-order E-field, (2.55), (or (2.20) for the "non-coupling case"), we will encounter averages in six different forms,

$$\begin{aligned} & < {}_{S1}P_{\vec{K},\omega\,S1}P^*_{\vec{K}_1,\omega_1\,S1}P^*_{\vec{K}_2,\omega_2} >,\ < {}_{W1}P_{\vec{K},\omega\,S1}P^*_{\vec{K}_1,\omega_1\,S1}P^*_{\vec{K}_2,\omega_2} > \\ & < {}_{S1}P_{\vec{K},\omega\,W1}P^*_{\vec{K}_1,\omega_1\,W1}P^*_{\vec{K}_2,\omega_2} >,\ < {}_{W1}P_{\vec{K},\omega\,W1}P^*_{\vec{K}_1,\omega_1\,W1}P^*_{\vec{K}_2,\omega_2} > \\ & < {}_{S1}P_{\vec{K},\omega\,S1}P^*_{\vec{K}_1,\omega_1\,W1}P^*_{\vec{K}_2,\omega_2} >,\ < {}_{W1}P_{\vec{K},\omega\,S1}P^*_{\vec{K}_1,\omega_1\,W1}P^*_{\vec{K}_2,\omega_2} > \quad . \end{aligned} \tag{A.29}$$

Based on (A.9) and (A.10), the first ensemble average of (A.29) can be written as

$$\begin{aligned} & < {}_{S1}P_{\vec{K},\omega\,S1}P^*_{\vec{K}_1,\omega_1\,S1}P^*_{\vec{K}_2,\omega_2} > \\ & = \sum_{m=\pm1}\sum_{m_1=\pm1}\sum_{m_2=\pm1} \sqrt{\frac{1}{8}\,{}_SS_1(m\vec{K})\,{}_SS_1(-m_1\vec{K}_1)\,{}_SS_1(-m_2\vec{K}_2)} \\ & \cdot \sqrt{\delta(\omega + m\sqrt{gK})\delta(-\omega_1 + m_1\sqrt{gK_1})\delta(-\omega_2 + m_2\sqrt{gK_2})\,d\vec{K}\,d\vec{K}_1\,d\vec{K}_2\,d\omega\,d\omega_1\,d\omega_2} \\ & \cdot < e^{jm\epsilon_s(m\vec{K})}e^{jm_1\epsilon_s(-m_1\vec{K}_1)}e^{jm_2\epsilon_s(-m_2\vec{K}_2)} > \quad . \end{aligned} \tag{A.30}$$

Clearly, the key to resolve (A.29) lies in the last line of (A.30), which is an average that contains three phase factors,

$$< e^{jm\epsilon_s(m\vec{K})} e^{jm_1\epsilon_s(-m_1\vec{K}_1)} e^{jm_2\epsilon_s(-m_2\vec{K}_2)} > \quad . \tag{A.31}$$

Since $\epsilon_s(\vec{K})$ represent independent variables uniformly distributed between 0 and 2π for each $\vec{K}$, $e^{jm\epsilon_s(m\vec{K})}$ naturally become zero-mean random variables, which suggests that

$$\begin{aligned} & < e^{jm\epsilon_s(m\vec{K})} e^{jm_1\epsilon_s(-m_1\vec{K}_1)} e^{jm_2\epsilon_s(-m_2\vec{K}_2)} > \\ =& < e^{jm\epsilon_s(m\vec{K})} > \cdot < e^{jm_1\epsilon_s(-m_1\vec{K}_1)} > \cdot < e^{jm_2\epsilon_s(-m_2\vec{K}_2)} > \\ =& \ 0 \qquad \text{if } m\vec{K} \neq -m_1\vec{K}_1 \neq -m_2\vec{K}_2 \end{aligned} \tag{A.32}$$

Thus, in order to for (A.31) to reach a non-zero result, it must be in the case that

$$\begin{aligned} & < e^{jm\epsilon_s(m\vec{K})} e^{jm_1\epsilon_s(-m_1\vec{K}_1)} e^{jm_2\epsilon_s(-m_2\vec{K}_2)} > \\ =& < e^{j(m+m_1+m_2)\epsilon_s(m\vec{K})} > \qquad \text{when } m\vec{K} = -m_1\vec{K}_1 = -m_2\vec{K}_2 \ . \end{aligned} \tag{A.33}$$

Since m, m_1 and m_2 take the value of ± 1, it is impossible for the sum of the three to be zero, i.e.,

$$m + m_1 + m_2 \neq 0 \tag{A.34}$$

which indicates that (A.33) will still reduce to zero. Overall, combining (A.32) and (A.33), it can be safely concluded that

$$< s_1 P_{\vec{K},\omega} s_1 P^*_{\vec{K}_1,\omega_1} s_1 P^*_{\vec{K}_2,\omega_2} > = 0 \quad . \tag{A.35}$$

Following exactly the same procedure, the remainder of (A.29) will be shown to

vanish just as (A.35). Thus, we can immediately state that

$$\mathcal{R}_{1,2}(\tau) = \mathcal{R}_{2,1}(\tau) = 0 \tag{A.36}$$

which suggests that we no longer have to deal with the cross-correlations of the first- and second-order E-fields.

Appendix B

Miscellaneous of the Swell Inversion Algorithm

B.1 The Theoretical Positions of Swell Peaks

In Chapter 2, it was seen that the Doppler positions of second-order swell peaks are solely determined by the swell period and dominant direction. In order to explain this observation, the theoretical positions of the four swell peaks shall be derived here.

Firstly, the swell peak on the far left shall be analysed. According to the delta constraint in (2.59),

$$\omega_{d1} = -m_1\sqrt{gK_1} - m_2\sqrt{gK_2} \tag{B.1}$$

the Doppler frequency of this swell peak, ω_{d1}, can be defined by a certain contour in the K_x, K_y plane (see Fig. B.1). Moreover, if we plot this contour over the corresponding swell wavenumber spectrum and wind wave wavenumber spectrum, it is seen that the contour always coincides with the peak of the swell spectrum. Clearly, the wave vector, $\vec{K}_s$, in Fig. B.1 points to the peak value of the swell spectrum; therefore, its magnitude can be related to the swell period, T_s, through the dispersion relationship

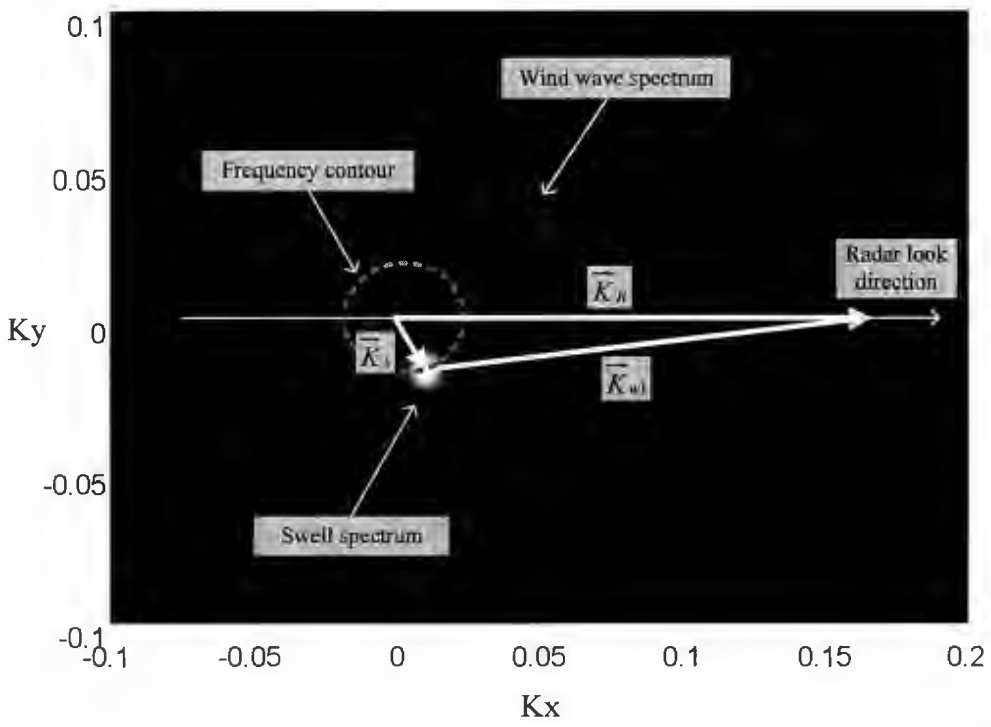

Figure B.1: The contour of ω_{d1} against the wave height spectrum.

as

$$K_s = \frac{(2\pi f_s)^2}{g} = \frac{4\pi^2}{gT_s^2} \tag{B.2}$$

while its direction, $\theta_{\vec{K}_s}$, is simply the dominant direction of the swell component. The remaining wave vector, defined by $\vec{K}_{w1} = \vec{K}_B - \vec{K}_s$, can be viewed as wind wave contribution. Referring to (B.1), and noting that $m_1 = 1$ and $m_2 = 1$ for the Doppler region under consideration, we may write the Doppler frequency of the far left swell peak as

$$\omega_{d1} = -\sqrt{gK_s} - \sqrt{gK_{w1}} \quad . \tag{B.3}$$

Next, the swell peak on the far right shall be examined. Again, we may plot the contour for ω_{d4} over the same wave height spectrum shown in Fig. B.1, and the result is illustrated by Fig. B.2. As can be observed from Fig. B.2, the frequency contour of ω_{d4} no longer goes through the peak of the swell spectrum; rather, it coincides with

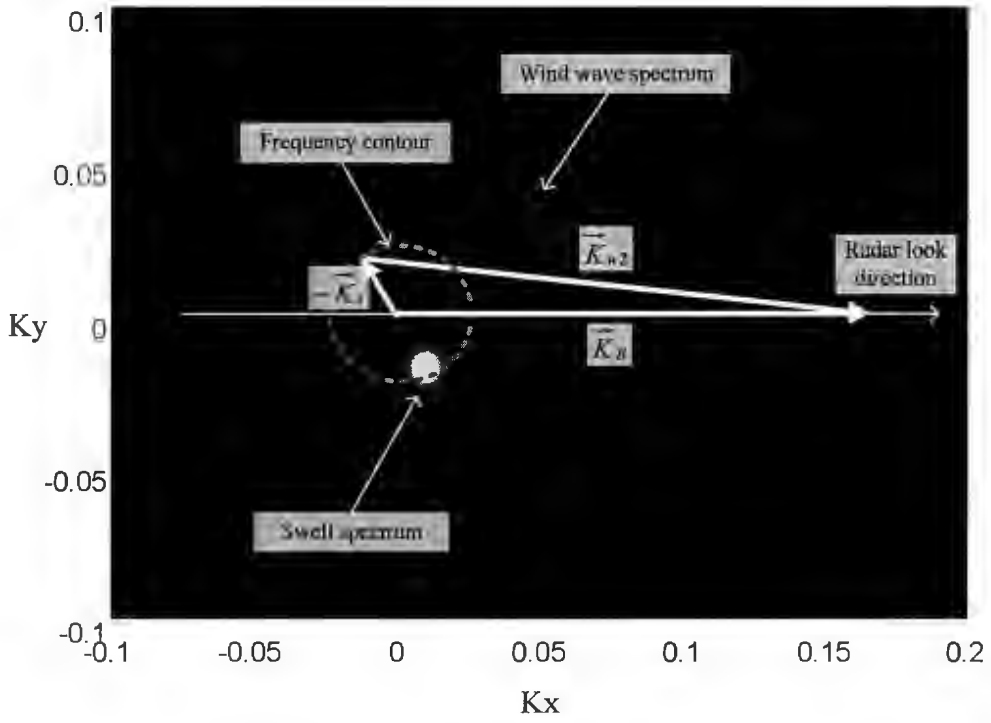

Figure B.2: The contour of ω_{d4} against the wave height spectrum.

the opposite vector of $\vec{K}_s$ in Fig. B.1. This is explained by the fact that for ω_{d4}, we have $m_1 = -1$ and $m_2 = -1$ so that ${}_SS_1(m_1\vec{K}_1) = {}_SS_1(-\vec{K}_1)$. Therefore, when $\vec{K}_1 = -\vec{K}_s$, the value of the swell spectrum is maximized, and by integrating over the contour that defines $-\vec{K}_s$, a swell peak can be formed. Now, the Doppler frequency of the far right swell peak is given by

$$\omega_{d4} = \sqrt{gK_s} + \sqrt{gK_{w2}} \tag{B.4}$$

where $\vec{K}_{w2} = \vec{K}_B + \vec{K}_s$ and, in this case, $|\vec{K}_{w2}| \geq |\vec{K}_{w1}|$.

The analysis for the remaining two peaks is similar to that presented above. For the second peak from the left, we have $m_1 = -1$ and $m_2 = 1$ for the case that

$K_1 < K_2$. Thus, its Doppler frequency can be written analogously to (B.4) as

$$\omega_{d2} = \sqrt{gK_s} - \sqrt{gK_{w2}} \quad . \tag{B.5}$$

Finally, for the second peak from the right, we have $m_1 = 1$ and $m_2 = -1$ for the case that $K_1 < K_2$, and its Doppler frequency is given by

$$\omega_{d3} = -\sqrt{gK_s} + \sqrt{gK_{w1}} \quad . \tag{B.6}$$

In brief, the Doppler positions of the swell peak depends on 1) the wave vector $\vec{K}_s$, which corresponds to the swell period T_s, and 2) the wind wave vectors, $\vec{K}_{w1}$ and $\vec{K}_{w2}$, which are determined by the swell propagation direction, $\theta_{\vec{K}_s}$. This conclusion directly verifies the statement made at the beginning of the section.

B.2 The Derivation of the Inversion Formula for Swell Period and Dominant Direction

In Section 4.3.2, we employed the fact that "swell peaks should be positioned theoretically at equal distances from their respective Bragg peak". The derivation for this statement is presented here.

Based on (B.3), the distance from the far left swell peak to the receding Bragg peak is given by

$$D_1 = (-\omega_B) - \omega_{d1} = -\omega_B + \sqrt{gK_s} + \sqrt{gK_{w1}} \tag{B.7}$$

and likewise, according to (B.5), the distance from the second peak to the receding

Bragg peak is

$$D_2 = \omega_{d2} - (-\omega_B) = \sqrt{gK_s} - \sqrt{gK_{w2}} + \omega_B \quad . \tag{B.8}$$

In order to prove that $D_1 = D_2$, we may write

$$D_1 - D_2 = \sqrt{gK_{w1}} + \sqrt{gK_{w2}} - 2\omega_B = \sqrt{g}(\sqrt{K_{w1}} + \sqrt{K_{w2}} - 2\sqrt{K_B}) \tag{B.9}$$

the value of which depends on the value range of K_{w1}, K_{w2} and K_B. Based on Fig. B.1 and Fig. B.2, we may easily deduce that

$$2K_B = (K_B - K_s) + (K_B + K_s) \leq K_{w1} + K_{w2} \leq 2\sqrt{K_B^2 + K_s^2} \quad . \tag{B.10}$$

Thus, for a typical case where the radar operating frequency is 15 MHz and the swell period is 14 seconds, the above value range is converted to

$$2K_B = 1.2566 \leq K_{w1} + K_{w2} \leq 1.2572.$$

and that

$$2\sqrt{K_B} = 1.5853, \ 1.5851 \leq \sqrt{K_{w1}} + \sqrt{K_{w2}} \leq 1.5857.$$

Since the possible errors in K are at the orders of 0.0001, which is far smaller than the Doppler resolution, we may safely conclude that for all practical purposes

$$K_{w1} + K_{w2} = 2K_B \ , \ \sqrt{K_{w1}} + \sqrt{K_{w2}} = 2\sqrt{K_B} \ . \tag{B.11}$$

Substituting (B.11) back into (B.9), we have $D_1 - D_2 = 0$. Similarly, the distances of the remaining two peaks to the approaching Bragg peak can be shown to be identical.

In Section 4.3.4, we used two inversion formulas, (4.14) and (4.15), to extract the

swell period and dominant direction, respectively. The detailed derivation shall be presented here. For (4.14), we may first calculate the value for Δf^+ and Δf^-, which is quite straightforward based on (B.3), (B.4), (B.5), (B.6):

$$\Delta f^+ = \frac{\omega_{d4} - \omega_{d3}}{2\pi} = \frac{2\omega_s + \omega_{w2} - \omega_{w1}}{2\pi} \tag{B.12}$$

and

$$\Delta f^- = \frac{\omega_{d2} - \omega_{d1}}{2\pi} = \frac{2\omega_s - \omega_{w2} + \omega_{w1}}{2\pi} \ . \tag{B.13}$$

Clearly, we have

$$\Delta f^+ + \Delta f^- = 4\frac{\omega_s}{2\pi} = 4f_s = \frac{4}{T_s} \ . \tag{B.14}$$

Thus, the inversion formula for the swell period can be derived as

$$T_s = \frac{4}{\Delta f^+ + \Delta f^-} \ . \tag{B.15}$$

For (4.15), we first employ the geometry in Fig. B.1, Fig. B.2 and the law of cosines to write that

$$K_s^2 + K_B^2 - 2K_sK_B\cos\theta = K_{w1}^2 \tag{B.16}$$

and

$$K_s^2 + K_B^2 - 2K_sK_B\cos(\pi - \theta) = K_{w2}^2 \tag{B.17}$$

Combining the above two equations, we have

$$4K_sK_B\cos\theta = K_{w2}^2 - K_{w1}^2 = (K_{w2} + K_{w1})(K_{w2} - K_{w1}) \ . \tag{B.18}$$

where θ denotes the angel between the radar look direction, θ_N, and the swell dominant

direction, θ_s. Based on (B.11), we may simplify the above equation into

$$\begin{aligned}\cos\theta &= \frac{(K_{w2}+K_{w1})(K_{w2}-K_{w1})}{4K_sK_B} = \frac{(K_{w2}-K_{w1})}{2K_s} \\ &= \frac{(\sqrt{K_{w1}}+\sqrt{K_{w2}})(\sqrt{K_{w1}}-\sqrt{K_{w2}})}{2K_s} = \frac{\sqrt{K_B}(\sqrt{K_{w1}}-\sqrt{K_{w2}})}{2K_s} \ . \end{aligned} \tag{B.19}$$

Through (B.14), we have the relation that

$$\Delta f^+ + \Delta f^- = \frac{4\omega_s}{2\pi} = \frac{2\sqrt{gK_s}}{\pi} \tag{B.20}$$

which immediately yields

$$K_s = (\frac{\Delta f^+ + \Delta f^-}{2}\pi)^2/g \ . \tag{B.21}$$

Similarly, we can easily deduce that

$$\Delta f^+ - \Delta f^- = \frac{\sqrt{K_{w2}}-\sqrt{K_{w1}}}{\pi} \tag{B.22}$$

which follows that

$$\sqrt{K_{w2}}-\sqrt{K_{w1}} = (\Delta f^+ - \Delta f^-)\pi \tag{B.23}$$

By substituting (B.21) and (B.23) back into (B.19), all the unknowns will be eliminated, and the final form of $\cos\theta$ is given by

$$\cos\theta = 8f_B\frac{(\Delta f^+ - \Delta f^-)}{(\Delta f^+ + \Delta f^-)^2} \tag{B.24}$$

which leads to the inversion formula for the swell dominant direction as

$$\theta_s = \theta_N \pm \cos^{-1}\left(8f_B\frac{(\Delta f^+ - \Delta f^-)}{(\Delta f^+ + \Delta f^-)^2}\right) \ . \tag{B.25}$$